



Energy management in electric systems fed by fuel cell stacks

Antonio Sanchez

► To cite this version:

Antonio Sanchez. Energy management in electric systems fed by fuel cell stacks. Other [cond-mat.other]. Université Paris Sud - Paris XI, 2011. English. NNT: 2011PA112032 . tel-00590217

HAL Id: tel-00590217

<https://theses.hal.science/tel-00590217>

Submitted on 3 May 2011

HAL is a multi-disciplinary open access archive for the deposit and dissemination of scientific research documents, whether they are published or not. The documents may come from teaching and research institutions in France or abroad, or from public or private research centers.

L'archive ouverte pluridisciplinaire **HAL**, est destinée au dépôt et à la diffusion de documents scientifiques de niveau recherche, publiés ou non, émanant des établissements d'enseignement et de recherche français ou étrangers, des laboratoires publics ou privés.



UNIVERSITÉ
PARIS-SUD 11

Faculté des
sciences
d'Orsay



Nº d'ordre:

THÈSE DE DOCTORAT

Présentée pour obtenir

LE GRADE DE DOCTEUR EN SCIENCES
DE L'UNIVERSITÉ PARIS-SUD XI

SPECIALITÉ : PHYSIQUE

Ecole Doctorale « Sciences et Technologies de l'Information des
Télécommunications et des Systèmes »

présentée par

Antonio SÁNCHEZ

Energy Management in Electric Systems Fed by Fuel Cell Stacks

Soutenue le 9 March 2011 devant la Commission d'examen:

M.	Jean-Claude VANNIER	(Président)
M.	Daniel HISSEL	(Rapporteur)
M.	Eric MONMASSON	(Rapporteur)
M.	Jean-Pierre BARBOT	(Examinateur)
Mme.	Françoise LAMNABHI-LAGARRIGUE	(Examinateuse invitée)
M.	Olivier BETHOUX	(Co-encadrant)
M.	Romeo ORTEGA	(Directeur de thèse)



Thèse préparée au
Laboratoire des signaux et systèmes (L2S)(UMR 8506)
Ecole supérieure d'électricité (Supélec)
3 rue Joliot-Curie
91 192 Gif-Sur-Yvette, France

ECOLE DOCTORALE STITS

THESE DE DOCTORAT

DE PHYSIQUE

SPECIALITE: Automatique

Année Universitaire 2010-2011

**Gestion d'Énergie Dans Des Systèmes Électriques
de Puissance Alimentés par Piles à Combustible**

**Energy Management in Electric Systems
Fed by Fuel Cell Stacks**

Antonio SÁNCHEZ

LABORATOIRE DES SIGNAUX ET SYSTEMES

UNIVERSITE PARIS-SUD XI

Directeur de thèse: Romeo ORTEGA

Co-encadrant de thèse: Olivier BETHOUX

To my wife and coming daughter.

Acknowledgments

I would like to express my sincere gratitude to my thesis advisor Romeo Ortega, for giving me the opportunity to develop this research subject. His unending capability of researching and skepticism were the model and provided me the motivation to finish this thesis. I also want to thank my co-supervisor Olivier Bethoux, for his scientific guidance and help during my extended work in LGEP and Eric Berthelot, for his invaluable help in the experimental setups.

Je tiens à remercier les rapporteurs Professeurs Daniel Hissel et Eric Monmasson pour leurs précieuses observations, et les membres du jury Professeurs Jean-Pierre Barbot, Jean Claude Vannier et Mme. Françoise Lamnabhi-Lagarrigue. I would like to specially thanks Mme. Lamnabhi for her permanent encouragement and, together with Eloisa Garcia-Canseco, being the forerunners of the Digiteo project, which made possible this thesis development.

Thanks to my first office-mate and friend Fernando Castaños for his theoretical orientation and for being the first in showing me how to deal with this new venture. To my friend Dhruv Shah for showing me the “new” Indian culture and bringing me back to my twenties. Thanks to Antoine Chaille for his friendship, help with the French language and destroying some stereotypes about French people. A mi amiga de la república-hermana de Argentina, Alejandra Garcia-Cattaneo, por aquellas largas conversaciones acerca de la procedencia de los pueblos prehispánicos. A mi único amigo chileno del L2S, José Saavedra, y a su novia Pamela Guevara, por compartir mis desahogos y rememorar lo querido, y no tan querido de Chile.

I would like to thank my friend Ioannis Sarris, for pulling me into more theoretical issues and for sharing with me special events of his life (his wedding). I also want to express my gratitude to my friend Romain Postoyan, he unsuccessfully encouraged me to learn the French language and showed me the culture of Bretagne, seafood mainly.

I will be always grateful of all my laboratory partners Michael, Wissam, Reine, Francesca, Luca, Alessio, Laurie, and F. Tiefensee, for the good moments that we

shared. I would like to acknowledge also Antonio Loria and Dr. Elena Panteley for their kindness and hospitality.

Profundo agradecimiento a mi padre y hermana por su apoyo permanente desde Chile.

Special gratitude to my beloved wife Maria-Isabel Yuseff, mainly for her unconditioned support and consideration during this period and also, for helping me with my poor English.

Finally I would like to acknowledge Digiteo project 2007-13D and the Chilean Council for Science and Technology (CONICYT), together with the French embassy in Chile, for their financial support.

Contents

Acknowledgments	v
Résumé	xi
Abstract	xiii
1 Introduction	1
1.1 Motivation	1
1.2 Outline of the Thesis	2
2 Fuel Cell Model Overview	5
2.1 Introduction to Fuel Cell Model	5
2.1.1 Fuel Cells Model Bibliography	8
2.2 Operation Principle of PEMFC	8
2.3 Fuel Cell Stack Model	9
2.3.1 Fuel Cell Stack Voltage Model	10
2.3.2 Cathode Flow Model	17
2.3.3 Anode Flow Model	19
2.4 Fuel Cell Auxiliary Components Models	20
2.4.1 Compressor Model	22
2.4.2 Lumped Model of the Manifold Dynamics	23
3 FC Test Bench Design and Development	25
3.1 Introduction and Objectives	25
3.1.1 FC Stack Specifications	26
3.2 Process Subsystems	28
3.2.1 Humidifier Subsystems	29

3.2.2	Compressor Subsystem	30
3.2.3	Temperature Regulating Subsystem	32
3.2.4	Air Supply Subsystem	33
3.2.5	Hydrogen Supply Subsystem	34
3.3	Acquisition, Automation, and Data Display	35
3.3.1	Data Acquisition	36
3.3.2	Control Loops and Protection Block	42
3.3.3	Data Display	46
3.4	Experimental Results	48
3.4.1	Experimental Characteristic Curve	48
3.4.2	Equivalent Impedance	49
3.4.3	Experimentation of Close Loop Operation	53
3.5	Conclusions	55
4	Dynamic Energy Router	57
4.1	Introduction	57
4.1.1	Criteria for Current Reference Selection	58
4.2	Formulation of the Energy Transfer Problem	59
4.3	The Duindam–Stramigioli Energy Router	61
4.4	Design with external bus voltage regulation	64
4.4.1	Linear controller, proportional plus integral (PI)	69
4.4.2	FL without considering the internal dynamics	81
4.4.3	FL considering the dynamics of the system	87
4.5	Design with no external bus-voltage regulation	92
4.5.1	Control Design	93
4.6	Conclusions	98
5	DSER in Fuel Cell Applications	101
5.1	Introduction	101
5.2	Description of the System	102
5.3	Standard Approach of the Energy Management	103
5.3.1	Current Controllers Design	105
5.3.2	Dc–bus Voltage Controller Design	107
5.3.3	Load Voltage Controller Design	107
5.3.4	Stability of the Close-Loop System	108
5.3.5	Simulation Results	110
5.4	Dynamic Energy Router Application	115

5.4.1	The Dynamic Energy Transfer Procedure	115
5.4.2	Controller Design	117
5.4.3	Simulation Results	118
5.5	Conclusions	123
6	Conclusions and Future Work	125
6.1	Concluding Remarks	125
6.2	Future Work	127
A	Appendix	129
A.0.1	PCB circuit adapter, 4 – 20 mA to 0 – 10 V	129
A.0.2	Thermocouple signal conditioner PCB design	130
A.0.3	Multiplexer PCB design	131

Résumé

La croissance des unités de distribution des ressources énergétiques ainsi que l'intégration des nouvelles technologies dans la production et le stockage d'énergie, ont imposé un contrôle nouveau et de nouvelles stratégies opérationnelles. Grâce à sa capacité de stockage et étant considérée comme une énergie propre; la pile à combustible (Pac) est l'une des technologies les plus prometteuse en tant que source d'énergie stationnaire dans les réseaux micro et aussi dans les applications de transport. Par conséquent, deux sujets principaux sont abordés dans cet ouvrage, la conception et l'installation d'un banc d'essai complet instrumenté a membrane échangeuse de polymère (PEM) Pac et de conception et l'essai expérimental d'une nouvelle stratégie de contrôle dynamique d'échange de l'énergie pour les systèmes multi - source et multi - charge. Pour définir le test instruments banc exigences, un examen complet de modèle dynamique est donné dans la première partie. Dans la prochaine section seront incluses, les renseignements concernant la configuration de la conception et la mise en œuvre de banc d'essai de Pac, i.e., critères de spécification des instruments, acquisition, et affichage des données du système. Des résultats expérimentaux sont réalisés afin de démontrer les potentialités de l'installation. Dans le chapitre suivant, une nouvelle stratégie de contrôle dynamique de l'énergie d'échange (DSER) sera introduite et testée par simulation et expérimentalement dans un système deux ports. Afin d'établir une comparaison et d'intégrer la DSER dans une application Pac, un système trois ports - y compris un modèle statique de Pac - et deux différentes approches de contrôle, seront testés par simulation dans le cinquième chapitre. La thèse s'achèvera par quelques conclusions et quelques thèmes de recherche potentiels générés partir de ce travail.

Abstract

The growth of distributed energy resources together with the incorporation of new technologies in the generation and storage of energy are imposing new control and operational strategies. Due to its storage capability and that it is considered to be clean energy; fuel cell (FC) is one of the most promissory technologies as a stationary energy source in micro grids and also in transportation applications. Therefore, two main issues are addressed in this work; the conception, design, and setup of a fully instrumented test bench for proton exchange membrane (PEM) FC stacks and the design and experimental test of a new dynamic energy-exchange control strategy for multi source and multi load systems. To define the test bench instrument requirements, in the first part a complete dynamic model review is given. In the next section, relevant information regarding the setup of the FC test bench design and implementation is included, i.e., specification criteria of the instruments and acquisition and data display system. Some experimental results are performed in order to demonstrate the potentialities of the setup. In the following chapter, a new dynamic energy exchange control strategy (DSER) is introduced and tested in a two port system via simulation and experimentation. In order to establish a comparison and integrate the DSER in a FC application, in the fifth chapter a three port system - including a static model of FC - and two different control approaches, are tested via simulation. The thesis is closed with some concluding remarks and some potential research topics generated from this work.

Chapter 1

Introduction

In the development of this thesis two main objectives were accomplished:

- ✓ Conception, design, and setup of a full instrumented test bench for proton exchange membrane (PEM) fuel cell (FC) stacks.
- ✓ Design and experimental test of a new dynamic energy-exchange control strategy for multi source and multi load systems.

1.1 Motivation

Due to its easy fuel storage capability and that it is considered clean energy, FC technology is used as an energy source in micro grids and also in transportation applications. Although, FC stacks and its applications are nowadays vastly studied, since they are complex systems most of the research regarding this subject can be considered as an innovation. The application has to adapt to the fast load changes and varying operating parameters. To reach this performance, the system behavior and its interactions with the different subsystems, e.g., FC auxiliaries or power electrical system, have to be understood and modeled. It is found that the improvements on the FC stack performance depends, not only on material characteristics, but also on the optimization of operating parameters. Once they are well understood and described in an appropriate model, this can be used to derive a control strategy for the whole FC system that maximizes or optimizes performance, efficiency and lifetime. Other advantages reside in the observability of variables that cannot be measured directly, yet represent an important possibility for improving the system performance, e.g., membrane water content. In order to successfully control and run a fuel cell system, the user must act on vari-

ous actuators, (e.g. air compressor, mass flow controllers, heaters , etc.), also the accurate control of the auxiliary system plays a significant role. Therefore, one of the main objectives of the present work is to setup a test bench for FC system evaluation. By experimentation it will be possible to obtain the model parameters that have a physical significance, and also it will be feasible to describe the interaction between the different subsystems, i.e., the fuel cell stack, the reactant supply subsystem, the temperature regulating subsystem and the electrical power load.

The growth of distributed energy resource units together with the incorporation of new technologies in generation and energy storage, are imposing new control and operational strategies. The dynamics of these new technologies in combination with the different energy storage capacity and/or the particular features of each source (e.g. noncontrollable energy coming from wind generators) will introduce constraints different from the ones that a conventional power system has. This work addresses the issue of control of energy flow in systems composed by various units. Moreover, the main objective regarding the energy exchange, is the development and experimental test of a new control strategy of energy exchange between multiple sources and loads. In a second stage, this novel strategy is extended to FC stack applications.

1.2 Outline of the Thesis

Chapter 2

As a first step in FC research a study of the static and dynamic model of the FC is given. Chapter 2 provides a summary of the FC model and specialized bibliography regarding this topic is presented. The objective of this chapter is to understand the dynamics and the variables that define the performance of the FC in order to design the test bench system. The basic operation of the FC is explained as an introduction, with some historical general information and the basic electrochemical reaction of the system. The description of the FC model is discussed in two sections; the FC stack model and the auxiliary components model, where the basis of this study is the control-oriented model presented in [1, 2, 3]. Due to the objectives of the thesis, especial emphasis is given to the FC stack model and to the compressor model.

Chapter 3

The specification and develop of the acquisition and data display system is described in detail in this chapter. Relevant information regarding the setup of the FC test bench design and implementation is included in the text and Appendix A. Specification criterions are mentioned in the text regarding, e.g., maximum power, flow, or limits values of pressure and temperature. Using as the starting technical information the FC characteristics, the chapter begins describing the process subsystems, where all the instrumentation, sensors, and actuators involved in the process of the plant (FC stack test bench) are described in detail. In the following section, the acquisition, automation and data display systems are described, in this part there is a detailed description of the signal conditioning, the controller implementation, and the screen display of the information. To demonstrate the united operation of the system and furthermore, to show the potential applications of the test bench, some experimental outcomes are also presented in this chapter.

Chapter 4

In this chapter an energy router that dynamically controls energy flow is presented. The router operational principle of this device, which we call the Duindam–Stramigioli energy router (DSER), is presented in [4], [5]. One of the objectives of this work is to implement the DSER by using standard power electronic converter topologies [6]. Since the objective is to extend this work to fuel cell fed systems, a power electronics scheme is designed and implemented [7, 8] to test its performance by simulation and experimentation. In a first step, a DESR design of two–subsystem interconnection based on an external bus voltage regulation is tested, and three different controllers are evaluated to illustrate the performance of this approach. The first results are obtained by testing linear controller (PI) [9, 10], afterwards a feedback linearization (FL) without considering the system dynamics and a FL considering the system dynamics are performed [11, 12]. Finally, the same two–subsystems, yet without external bus voltage regulation, is tested by simulation and experimentation using FL controller incorporating the system dynamics.

Chapter 5

The extension to three ports of the dynamic energy router is accomplished in Chapter 5. As it is shown in the specialized literature [13, 14, 15, 16] the hy-

bridization of FC stack with supercapacitors or batteries is a common practice. The difference on their time response turns them in sort of complementary equipment. The first approach to solve the energy exchange management in multiport FC fed system is by using liner controllers and standard procedure. Alternative techniques are presented in [17, 18, 19], yet a common practice is to calculate the instantaneous load power, supply the demanded power with the FC (restricting the rate and the maximum current) and keep the bus voltage constant using the fast response of the supercapacitor. With the purpose of evaluation and to establish a comparison between the two approaches, the DSER is applied to solve the energy exchange problem in the multiport system. The flow direction and rate of change of the energy, initially regulated by means of $\alpha(t)$ in a two ports system, is now extended to three ports introducing a more flexible interconnection matrix. A controller based on a feedback linearization is used to track the references given by the DSER.

Chapter 2

Fuel Cell Model Overview

2.1 Introduction to Fuel Cell Model

Fuel Cells are electrochemical energy converters. They can be seen as black-boxes turning chemical energy contained in a fuel directly into electrical energy while generating heat and water as byproducts. The mechanism involved in this conversion is the same as the one for batteries. The primary difference is that the battery contains the reactants that generate electricity whereas those reactants need to be supplied externally to the fuel cell i.e. a battery needs to be thrown away or recharged once those reactants are depleted while the fuel cell can be refueled by refilling the tank with hydrogen. In this respect they are comparable to internal combustion engines which generate mechanical power with heat and exhaust gases as byproducts. The first demonstration of a fuel cell was done by William Grove in 1839 [20], using an experiment like the one shown in Fig. 2.1. Yet with the development of the steam engine and the later discovery of the internal combustion engine, fuel cells did not see any industrial development until the 20th century.

The basic reaction shown in Fig. 2.1(a) illustrates how water is being electrolyzed into hydrogen and oxygen by passing an electric current through it. In Fig. 2.1(b), the power supply has been replaced with an ammeter that measures the current flow, the electrolysis is being reversed so the hydrogen and oxygen are recombining, and an electric current is being produced. The chemical reaction that regulates this process is described by (2.1)



The main advantages of fuel cells with respect to traditional energy converters

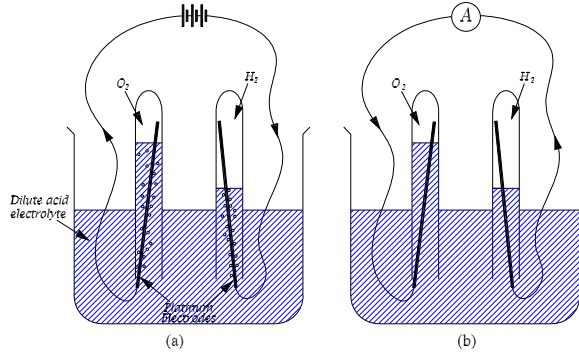


Figure 2.1: Electrochemical reaction related with the fuel cell process. (a) Electrolisis of the water. (b) Recombination of O_2 and H_2 and the consequent production of electricity.

are:

- A high conversion efficiency. A very interesting characteristic for the transportation sector is that efficiency increases with diminishing load, in contrary to the internal combustion engine where efficiency is reduced together with the load conditions [19].
- Low emissions. Zero-emission performance is achieved since the only reaction product is water. Even if natural gas or petrol is used as a fuel through a reforming process, CO_2 emissions will be lower than a conventional system.
- Low noise levels. Since no moving parts are required for the energy conversion, operation of the fuel cell is almost completely silent, the only noise emission will be produced by the air compressor.

Different types of fuel cells have been developed. They are typically classified by, either their operating temperature or the type of electrolyte. Table 2.1 gives an overview of the main classes of fuel cells with their associated fuels, operating temperatures and electrolyte types.

Proton Exchange Membrane Fuel Cells (PEMFC) or Polymer Electrolyte Membrane Fuel Cells are based on a solid polymer electrolyte. Its characteristics are fast startup times, low temperature operation and high power densities make them an easy to use technology especially for portable or transport applications. Since the polymer membrane has to be kept well humidified for good proton conduction, water management is one of the critical issues for a satisfactory performance.

Table 2.1: Data of different types of FC

Fuel cell type	Mobile ion	Temperature	Fuel
PEMFC	H^+	50 – 90°C	H_2
DMFC	H^+	50 – 90°C	CH_3OH
AFC	OH^-	60 – 250°C	H_2
PAFC	H^+	~ 220°C	H_2
MCFC	CO_3^{2-}	~ 650°C	H_2, CO, CH_4
SOFC	O^{2-}	750 – 1000°C	H_2, CO, CH_4

Direct Methanol Fuel Cells (DMFC) are similar in construction to PEM fuel cells. Since liquid methanol can be used as a fuel, no external fuel processing is required and high energy storage densities can be achieved. An important drawback relies on the fact that the polymer membrane is not impermeable to liquid methanol and the resulting fuel crossover reduces overall system efficiency.

Alkaline Fuel Cells (AFC) are based on a liquid, concentrated KOH electrolyte. AFCs can operate with non-precious metal catalysts and therefore have a cost advantage over other types of fuel cells. The use of a liquid electrolyte requires an additional electrolyte re-circulation system. The use of AFCs has been limited to niche applications such as military and space applications.

Phosphoric Acid Fuel Cells (PAFC) are based on a liquid acid electrolyte. Due to their higher operating temperature, they are less sensitive to CO impurities in the fuel. Their relatively long start-up times and low power densities limit their application to stationary power or co-generation plants.

Molten Carbonate Fuel Cells (MCFC) are based on a liquid molten carbonate electrolyte and generally exhibit very high conversion efficiencies. A high operating temperature allows direct use of non noble catalysts along with direct internal processing of fuels such as natural gas. Relatively long start-up times and low power densities limit their application to stationary power or co-generation plants.

Solid Oxide Fuel Cells (SOFC) are based on a solid oxide electrolyte conducting oxygen O^{2-} ions. As the MCFC, the high operating temperature translates into non-noble catalysts, direct internal hydrocarbon fuel processing and high quality waste heat that can be utilized in combined-cycle power plants. High power densities along with high efficiencies can be attained with this technology.

Slow start-up times dictate their primary use as stationary power or co-generation plants.

2.1.1 Fuel Cells Model Bibliography

Extensive studies have been done regarding the FC modeling, from the static models presented in [13, 20, 21] to the complex dynamic models presented in [1, 22, 23]. Where, [1] presents a control oriented model based on the electrochemical reaction and the dynamic internal behavior of the gases, in [22] the governing equations of the transient behavior of a FC are presented taking especial care about the water management inside the stack, and in [23] a dynamic electrical terminal model of a PEMFC is developed by extending a static current voltage description to include the temperature. Simulation oriented models that considered the representation of the auxiliaries and thermal phenomenons can be found in the literature [24, 25], where in the case of [25] the goal is to modeled a close FC stack, or black box FC. Interesting models based on the transient electric terminal variables [26] can be useful for monitoring the state of health. Due to the potential application of FC technology in transportation, vehicle oriented models are also available in the literature [27, 28, 29]. Advance applications of the modeling, as the predicting scheme presented [30, 31] is the outcome of expert knowledge regarding FC dynamics.

2.2 Operation Principle of PEMFC

A PEMFC consists of an electrolyte sandwich between two electrodes. The electrolyte has a special property that allows positive ions (protons) to pass through while blocking electrons. Hydrogen gas passes over one electrode, called an anode, and with the help of a catalyst, separates into electrons and hydrogen protons, as shown in Fig. 2.2. The chemical reaction that described this process is



The protons pass through the electrolyte towards the cathode, and the electrons close the circuit through the electric load, performing electric work. In the cathode, the protons and electrons combine with oxygen produce water, this reaction is described by



The overall reaction that takes place in the fuel cell is



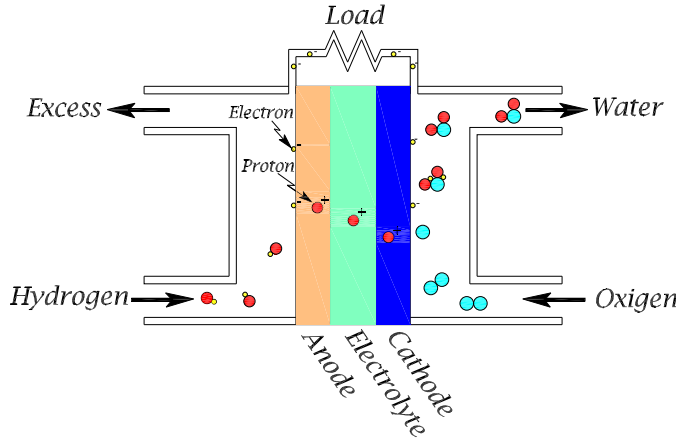


Figure 2.2: Scheme of one cell internal process.

Each cell produced between 0 to 1 volts according to the fuel cell operating conditions and the electric load connected, normally the voltage is close to 0.7 V. In order to reach higher voltage values, cells are assembly in series (stack). The membrane is sandwiched between two electrodes (anode and cathode) made from a highly conducting material such as porous graphite. This is to give the maximum possible contact between the electrode, the electrolyte, and the gas [20]. One special feature of PEM FC is that their operation temperature is between 50 and 100°C which permits and operation without thermal insulation. The polymer electrolyte membrane is an electronic insulator but an excellent conductor of protons. When the membrane becomes hydrated, the protons (H^+) become mobile. Depending on membrane manufacturers and the versions of the membrane, properties of the membranes differ. The thickness of the membrane varies from 50 to 175 microns, which is approximately 2 to 7 papers thick. A small amount of platinum is applied to the surface of the anode and cathode to help increase the rate of reaction. The structure of a membrane electrolyte assembly (MEA) is an assembly of anode, electrolyte, and cathode, the three of them sealed together, this structure is normally less than one millimeter thickness.

2.3 Fuel Cell Stack Model

In this section the main FC stack models are reviewed, these are the stack voltage, the anode flow, and the cathode flow. The models here presented are based on [1, 2, 32]. In the voltage model, an equation is used to calculate stack voltage for different operating conditions. The cathode and anode flow models use mass

conservation along with thermodynamic properties to calculate the pressure and the relative humidity of the reactant gas flow inside the stack [2, 20, 33], for all these calculations the stack temperature is assumed to be constant. The process inside the a FC are shown in Fig. 2.3 where MEA is the membrane electrode assembly that was explained in the previous chapter. The process of water transfer across the membrane will not be considered in this model review, for further details in this respect refer to [2].

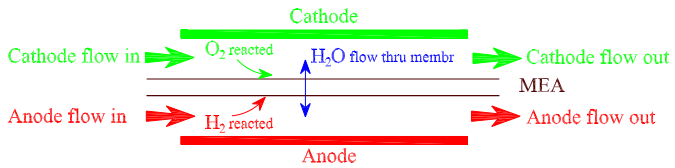


Figure 2.3: FC stack mass flow.

2.3.1 Fuel Cell Stack Voltage Model

In this section, by means of energy balance, the fuel cell terminal voltage is calculated. In this respect, three types of losses are shown. The electrical equivalence circuit is also briefly explained.

Fuel Cell Open Circuit Voltage

A FC stack can transform chemical energy into electrical energy, the chemical energy produced by the reaction is calculated by the variation of Gibbs free energy, i.e., difference of the Gibbs free energy of the product and the Gibbs free energy of the reactants. By using the Gibbs free energy is also possible to calculate the energy able to perform external work [20]. The basic chemical reaction that take place inside the FC is



and the corresponding Δ Gibbs free energy is

$$\Delta g_f = (g_f)_{H_2O} - (g_f)_{H_2} - (g_f)_{O_2}. \quad (2.6)$$

It can be seen that the Gibbs free energy depends on the temperature and pressure. Therefore, as shown in [32], after some calculation and simplifications, the

Table 2.2: $\Delta\bar{g}_f$ for the reaction shown in (2.5) [20].

Form of Water	Temperature (C°)	$\Delta\bar{g}_f$ (kJ mol $^{-1}$)
Liquid	25	-237.2
Liquid	80	-228.2
Gas	80	-226.1
Gas	100	-225.2
Gas	200	-220.4
Gas	400	-210.3
Gas	600	-199.6
Gas	800	-188.6
Gas	1000	-177.4

reversible voltage of the FC can be written as

$$E = \frac{-\Delta g_f}{2F} = \frac{-\Delta g_f^0}{2F} + \frac{RT_{fc}}{2F} \ln \left[\frac{p_{H_2} p_{O_2}^{\frac{1}{2}}}{p_{H_2O}} \right]. \quad (2.7)$$

where Δg_f^0 is the change in Gibbs free energy at 1 Bar, T_{fc} is the temperature of the FC (in Kelvin), p_{H_2} , p_{O_2} , and p_{H_2O} are the partial pressure of the hydrogen, oxygen, and vapor, respectively (expressed in Bar), R is the universal gas constant 8.31451 J/(kg·K), F is the Faraday Constant (96485 Coulombs), and E is the FC terminal voltage. Different values of the Gibbs free energy of (2.5) at 1 Bar are given in Table 2.2. The negative sign of Δg_f^0 is referred to the fact the the energy is released.

Since the fuel cell process is not reversible, some of the chemical energy is converted to heat, and the fuel cell voltage, V_{fc} , is less than that in (2.7). E in (2.7) is the open circuit voltage, also known as Nernst voltage of an hydrogen FC. The term $-\Delta g_f^0/2F$ varies from standard state ($25^\circ C$ and 1 atm) reference potential (1.229 V) in accordance with the temperature. As shown in [2] and [32], and using the standard state value of temperature ($298.15 K$) and entropy change to solve $-\Delta g_f^0/2F$, (2.7) can be written as

$$E = 1.229 - 0.85 \times 10^{-3}(T_{fc} - 298.15) + 4.3085 \times 10^{-5}T_{fc} \left[\ln(p_{H_2}) + \frac{1}{2} \ln(p_{O_2}) \right] V. \quad (2.8)$$

Where, T_{fc} is expressed in Kelvin, and p_{H_2} and p_{O_2} are expressed in atm. Considering that the reaction is irreversible and that the process contains losses, the FC voltage is normally less than the value calculated in (2.8). This losses, intrinsic of the FC, are the activation, ohmic, and concentration losses.

Activation Losses

This effect, also called, activation overvoltage is produced as a result of the electron transfer and the rupture of the chemical bonds in the cathode and anode [2] [32]. As shown in [20] an amount of energy is used to drive the electrons towards and from the electrodes. Due to the difference between the velocity of the reactions in the anode and cathode, the activation loss is mainly ruled by the cathode process. The Tafel equation is the better way to describe the connection between the activation loss and the current density [20].

$$v_{act} = a \ln \left(\frac{i}{i_0} \right), \quad (2.9)$$

where a and the current density (i_0) are constants that can be empirically deter-

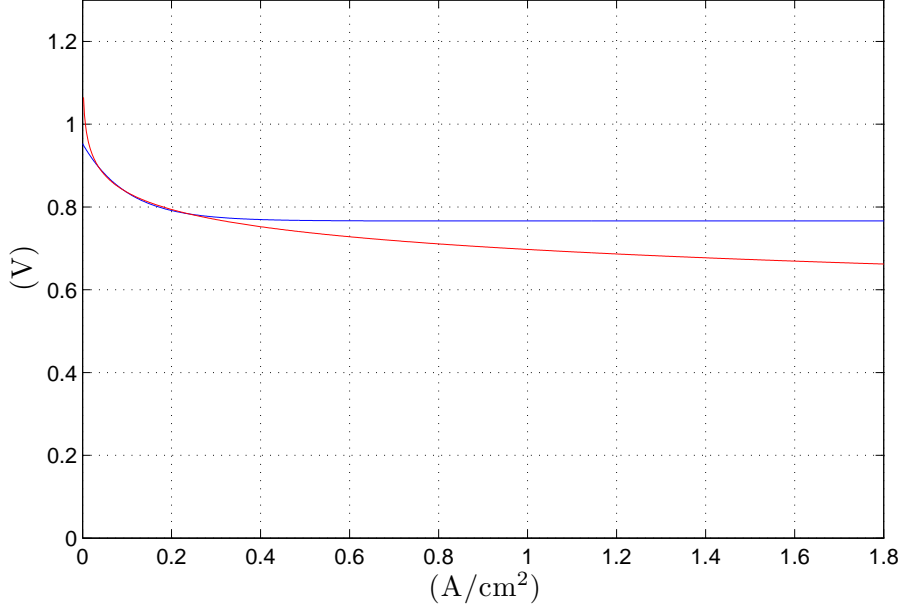


Figure 2.4: Voltage variation for activation losses. Red line for (2.9) and blues line for (2.10).

mined. This equation is valid for $i > i_0$. A the typical value for PEMFC is $i_0 \simeq 0.1$

mA/cm^2 [20]. In Fig. 2.4 is shown the activation loss in red color. Due to the restrictions of (2.9) ($i > i_0$), other function valid for all the operation conditions is desirable. To supply the requirements, the new approximation is given by

$$v_{act} = v_0 + v_a (1 - e^{-c_1 i}), \quad (2.10)$$

where v_0 (volts) is the voltage loss (in open circuit), and v_a (volts) and c_1 are constants. By means of nonlinear regression and by the utilization of (2.9), the values of v_0 , v_a , and c_1 can be determined. In Fig. 2.4 is shown (blue graph) the voltage loss obtained by using (2.10).

Ohmic Losses

This loss is generated by the resistive effect of, the pass of protons across the membrane and the flow of electrons through the electrodes. The voltage drop due to ohmic loss is proportional to the current density

$$v_{ohm} = i R_{ohm} = i \frac{t_m}{\sigma_m} \quad (2.11)$$

where R_{ohm} is the internal resistance expressed in $\Omega \cdot \text{cm}^2$, t_m is the thickness of the membrane, and σ_m is the membrane conductivity. There is a dependency between the resistance and the membrane humidity and internal temperature. The ohmic resistance is a function of the membrane conductivity σ_m , $(\Omega \cdot \text{cm})^1$, which is also a function of water content of the membrane (λ_m) and the FC temperature. As it is shown [33] the water content can take values from 0 to 14 (equivalent to relative humidity of 0% and 100%, respectively). The values of membrane conductivity is given by (2.12), as can be seen from this equation σ_m depends on the membrane humidity and temperature [33]

$$\sigma_m = (b_{11}\lambda_m - b_{12}) \exp \left(b_2 \left(\frac{1}{303} - \frac{1}{T_{fc}} \right) \right). \quad (2.12)$$

The constants b_{11} , b_{12} and b_2 are normally empirically determined.

Concentration Losses

The concentration loss is produce by the reactance variation due to the consumption of them during the operation. This loss produced a fast voltage drop at high current demand. In [2] and [32] is presented equation (2.13) which approximates the voltage loss generated by the concentration losses

$$v_{con} = i \left(c_2 \frac{i}{i_{max}} \right)^{c_3}, \quad (2.13)$$

where the constants c_2 , c_3 , and i_{max} are obtained empirically and depends on the temperature and the reactant partial pressure. In (2.13) i_{max} is the current density that generates abrupt voltage drop.

Cell Terminal Voltage

By adding the different voltage drops and the voltage given by 2.8, the operation terminal voltage of the FC is given by

$$\begin{aligned} v_{fc} &= E - v_{act} - v_{ohm} - v_{con} \\ &= E - [v_0 + v_a (1 - e^{-c_1 i})] - [i R_{ohm}] - \left[i \left(c_2 \frac{i}{i_{max}} \right)^{c_3} \right]. \end{aligned} \quad (2.14)$$

This voltage(v_{fc}) is the voltage of a single cell, the final voltage is calculated by multiplying the cell voltage by the n series assembled cells, conforming a stack. Therefore, the final voltage will be given by $v_{st} = n \times v_{fc}$.

As it is explained in [2], [32], and [34], by applying mathematic regression to the experimental results of a FC, one can obtain the empirical parameters that described the behavior characteristic curve of it.

The polarization or characteristic curves obtained by using the described method are shown in Fig. 2.5. In this figure (represented separately) are shown the influence of each loss phenomenon over the nominal voltage of a cell. It can be seen that the activation losses are the ones that most strongly shape the output voltage of the FC.

In Fig. 2.6 are shown the activation (a), ohmic (b), concentration overvoltage (c) and voltage output (d), all of them for a range of pressure of 1 to 2 bar at 80°C. Fig. 2.6 (a) and (c) depict the influence that the pressure has over the activation and concentration losses.

Fuel Cell Electric Equivalence

Considering that the FC behaves as a voltage source with internal losses (previously described), is suitable to propose an equivalent electric scheme that takes into account the internal characteristics of the it. As its is described in the technical bibliography [2, 32], the internal charge double layer behaves, and can be modeled, as a capacitor. The changes produced in the charge of this double layer produced a voltage, which is the combination of the activation and concentration effect. Moreover, due to the presence of the capacitance and its time constant ($R \times C$), there exists a delay between the activation and concentration effects

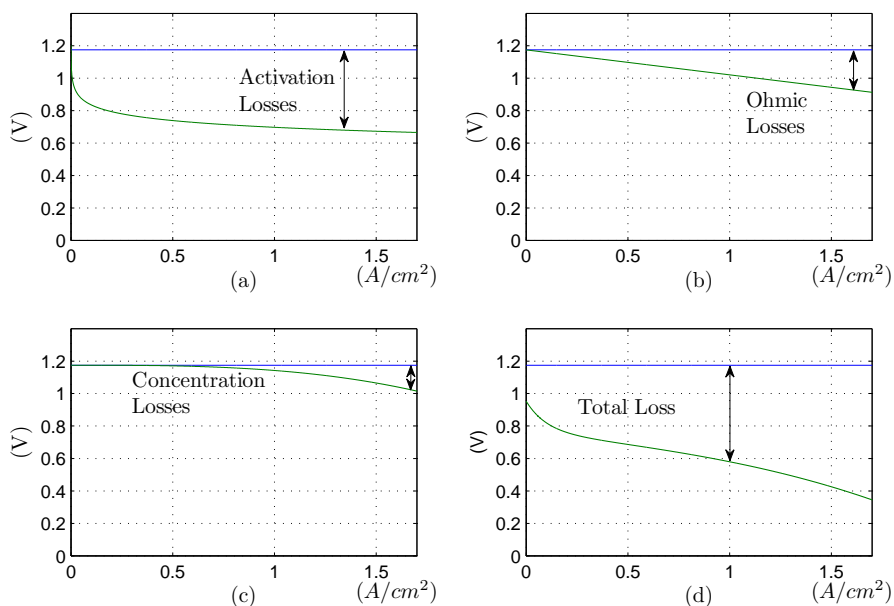


Figure 2.5: Voltage drop cause by the intrinsic losses of the FC. (a) Activation losses. (b) Ohmic losses. (c) Concentration losses. (d) Overall behavior of the voltage output.

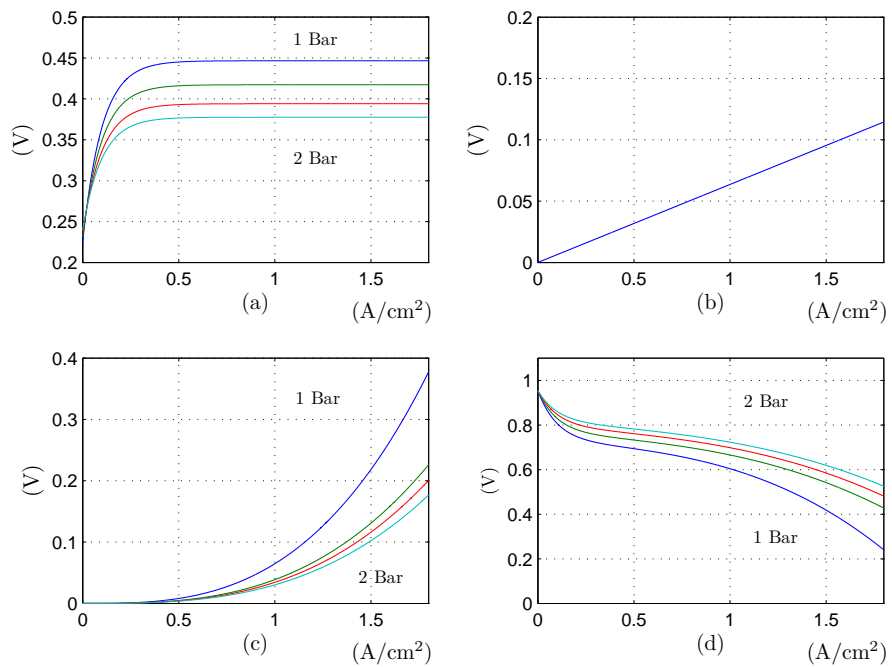


Figure 2.6: Voltage drop and FC voltage for a range of operation pressure (1 to 2 bar). (a) Variation of the activation losses. (b) Ohmic losses. (c) Variation of concentration losses. (d) Different polarization curves of the FC.

and the abrupt changes of the FC current. This delay does not exist in the case of ohmic losses, where the response to load variation is instantaneous. Finally, and according to the equivalent circuit depicted in Fig. 2.7, the activation resistance (R_{act}) and the concentration resistance (R_{con}), shown in (2.15) and (2.16) respectively, can be used to define the following electrical model of the FC.

$$R_{act} = \frac{1}{i} [v_0 + v_a(1 - e^{-c_1 i})], \quad (2.15)$$

$$R_{con} = \left(c_2 \frac{i}{i_{max}} \right)^{c_3}. \quad (2.16)$$

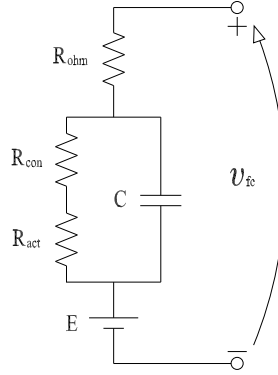


Figure 2.7: FC equivalent electric model.

Hence, the FC voltage can be described by

$$i = C \frac{dv_c}{dt} + \frac{v_c + v_0}{R_{act} + R_{con}}, \quad (2.17)$$

$$v_{fc} = E - v_c - iR_{ohm}. \quad (2.18)$$

2.3.2 Cathode Flow Model

As is shown in the literature [2, 32], this model represents the behavior of the air inside the cathode, and is developed by applying thermodynamic properties and mass conservation. The mass of oxygen, nitrogen, and water is balanced in the system, as it is depicted in Fig. 2.8. Three states are defined to study the cathode behavior, oxygen mass ($m_{O_2,ca}$), nitrogen mass ($m_{N_2,ca}$), and water mass ($m_{H_2O,ca}$). The model input are the current of the stack (I_{st}), temperature of the stack (constant), flow of water across the membrane ($W_{H_2O,membr}$), exiting pressure (p_{rm}), inlet flow temperature ($T_{ca,in}$), inlet pressure ($p_{ca,in}$), inlet mass flow rate ($W_{ca,in}$), inlet humidity ($\phi_{ca,in}$), and oxygen mole fraction ($y_{O_2,ca,in}$) (equal to 0.21 for atmospheric air).

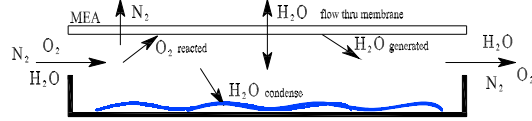


Figure 2.8: Cathode mass flow.

As shown in the literature, many assumptions are used to develop the model.

- All gases are considered to behave as ideal gases.
- The temperature of the fuel cell stack is kept constant at its nominal value ($T_{ca,out} = T_{ca} = T_{st}$).
- The temperature of the gas inside the cathode is assumed to be equal to the stack temperature.
- The values of the cathode exiting variables ($T_{ca,out}$, $p_{ca,out}$, $\phi_{ca,out}$, and $y_{O_2,ca,out}$) are assumed to be the same as the inlet cathode variables (T_{ca} , p_{ca} , ϕ_{ca} , and $y_{O_2,ca}$).
- The liquid coming from vapor condensation does not leave the stack and will either evaporate or it will accumulate as water in the cathode.
- The volume variations is dismissed.

Therefore, the following state equations are defined

$$\frac{dm_{O_2,ca}}{dt} = W_{O_2,ca,in} - W_{O_2,ca,out} - W_{O_2,reacted}, \quad (2.19)$$

$$\frac{dm_{N_2,ca}}{dt} = W_{N_2,ca,in} - W_{N_2,ca,out}, \quad (2.20)$$

$$\frac{dm_{H_2O,ca}}{dt} = W_{v,ca,in} - W_{v,ca,out} + W_{v,ca,gen} + W_{v,membr} - W_{l,ca,out}, \quad (2.21)$$

where $W_{O_2,ca,in}$ is the mass flow rate of oxygen entering the cathode,
 $W_{O_2,ca,out}$ is the mass flow rate of oxygen exiting the cathode,
 $W_{O_2,reacted}$ is the reacted oxygen ,
 $W_{N_2,ca,in}$ is the mass flow rate of nitrogen entering the cathode,
 $W_{N_2,ca,out}$ is the mass flow rate of nitrogen exiting the cathode,
 $W_{v,ca,in}$ is the mass flow rate of water vapor entering the cathode,
 $W_{v,ca,out}$ is the mass flow rate of water vapor exiting the cathode,
 $W_{v,ca,gen}$ is the rate of water vapor produced in fuel cell reaction,
 $W_{v,membr}$ is the mass flow rate of water transfer through the FC membrane,
 $W_{l,ca,out}$ is the rate of liquid water exiting the cathode.

The incoming flows are denoted by the subscript *in* and the exiting flows with the subscript *out*.

By using thermodynamics principles and the mass of oxygen, nitrogen, and vapor inside the cathode, the partial pressures can be calculated. Using this last results, the partial pressure of dry air can be written as

$$p_{a,ca} = p_{O_2,ca} + p_{N_2,ca}, \quad (2.22)$$

and in the same way, the addition of the air and vapor partial pressure will give us the total cathode pressure (p_{ca}),

$$p_{ca} = p_{a,ca} + p_{v,ca} = p_{O_2,ca} + p_{N_2,ca} + p_{v,ca}. \quad (2.23)$$

Further details are given in the specialized literature [1, 2, 32] about the calculation of the inlet mass flow rate of oxygen ($W_{O_2,ca,in}$), nitrogen ($W_{N_2,ca,in}$), vapor ($W_{v,ca,in}$), and cathode exit flow rate ($W_{ca,out}$), which are not part of the objectives of this work. Finally, by using electrochemistry principles, $W_{O_2,reacted}$ and $W_{v,ca,gen}$ can be expressed as follows

$$W_{O_2,reacted} = M_{O_2} \times \frac{nI_{st}}{4F}, \quad (2.24)$$

$$W_{v,ca,gen} = M_v \times \frac{nI_{st}}{2F}, \quad (2.25)$$

where I_{st} is the stack current, n is the cell number, F is the Faraday number, M_{O_2} is the molar mass of oxygen, and M_v is the molar mass of water.

2.3.3 Anode Flow Model

In standard applications hydrogen is supplied from high pressure bottles. On the other hand, it is also considered that the resistance to flow in the anode is less than in the cathode. Other assumptions mentioned in the previous section stands for the anode model. The calculation of the mass dynamic inside the anode is

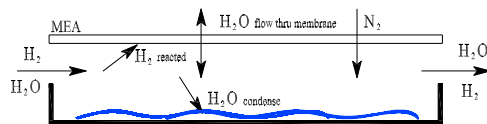


Figure 2.9: Anode mass flow.

determined following the same procedure as in the previous case (cathode), yet in this case two state equations are derived (2.26) and (2.27). Fig. 2.9 depicts the

mass flow of the different gases and water inside the anode. As it is shown in the bibliography [2, 32] the model inputs are the anode inlet mass flow ($W_{an,in}$), inlet humidity ($\phi_{an,in}$), inlet pressure ($p_{an,in}$), inlet temperature ($T_{an,in}$), stack current (I_{st}), stack temperature (T_{st}), and $W_{v,membr}$. On the other hand the states are the hydrogen mass and the water mass, described by,

$$\frac{dm_{H_2,an}}{dt} = W_{H_2,an,in} - W_{H_2,an,out} - W_{H_2,reacted}, \quad (2.26)$$

$$\frac{dm_{H_2O,an}}{dt} = W_{v,an,in} - W_{v,an,out} - W_{v,membr} - W_{l,an,out}, \quad (2.27)$$

where $W_{H_2,an,in}$ is the mass flow rate of hydrogen entering the anode,
 $W_{H_2,an,out}$ is the mass flow rate of hydrogen exiting the anode,
 $W_{H_2,reacted}$ is the rate of hydrogen reacted,
 $W_{v,an,in}$ is the mass flow rate of vapor entering the anode,
 $W_{v,an,out}$ is the mass flow rate of vapor exiting the anode,
 $W_{v,membr}$ is the mass flow rate of water transfer through the FC membrane,
 $W_{l,an,out}$ is the rate of liquid water exiting the anode.

Due to the fact that hydrogen comes from the high pressure bottle, its flow rate can be instantaneously adjusted with an electronic valve. Moreover, considering that 0 hydrogen is wasted in the anode, the hydrogen consumption due to the reaction is

$$W_{H_2,reacted} = M_{H_2} \times \frac{nI_{st}}{2F}. \quad (2.28)$$

Where, M_{H_2} is the hydrogen molar mass. On the other hand, if the purge is known, the hydrogen and the water vapor can be also calculated using other equations.

2.4 Fuel Cell Auxiliary Components Models

In this section, a brief description of the main auxiliary subsystems of a FC system is presented. As it was mentioned, the dynamic behaviors due to manifold filling, membrane water content, and temperature may impact the performance of the application. Since it is governed by a slow dynamics, the temperature of the system is normally considered constant while analyzing it.

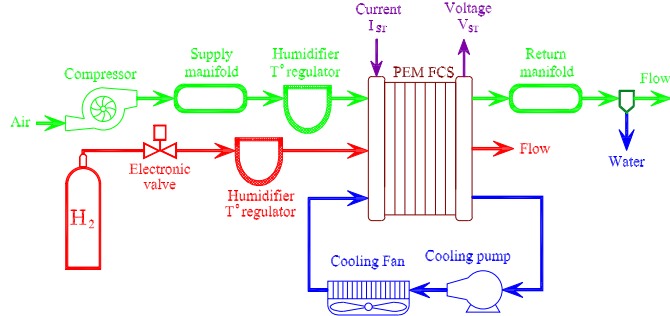


Figure 2.10: System basic diagram.

In Fig. 2.10 is shown a block diagram with the subsystem blocks together with the corresponding flow directions. The fundamental subsystems and devices of an standard implementation of FC stack are included in this diagram. These are compressor, supply manifold, return manifold, hydrogen tank, electronic valve, humidification system, FC stack, and cooling system. The instrumentation is not included in this diagram and will be discussed in detail in Chapter 3. On the other hand, a scheme containing the main flows associated with the FC process is shown in Fig. 2.11, where the flow of H_2 and *air* inside the anode and cathode are presented, respectively.

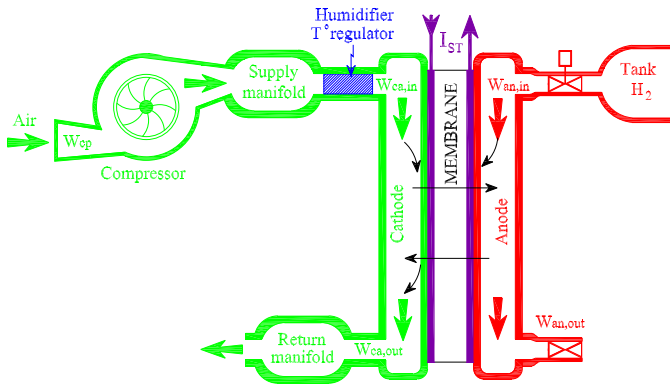


Figure 2.11: Reactant supply diagram.

The auxiliary components described in this work are the compressor dynamic model and the manifold model. More detailed auxiliary models can be found in the literature.

2.4.1 Compressor Model

In a standard analysis the model of the compressor is separated into a static compressor map and the compressor and motor inertia, therefore, the speed could be then used in the compressor map to find the air mass flow rate.

The model considers one state, this is the compressor speed (ω_{cp}). The model inputs are the inlet air pressure ($p_{cp,in}$), its temperature ($T_{cp,in}$), compressor feeding voltage (v_{cpm}), and exiting pressure ($p_{cp,out} = p_{sm}$). The input of the compressor is commonly atmospheric air and its conditions are assumed known ($p_{atm} = 1\text{ atm}$ and $T_{atm} = 25^\circ C$). By using the compressor map and the speed is possible to determined the compressor air mass flow rate, W_{cp} (kg/sec). Yet, as is mentioned in [35], using the compressor map as a lookup table is unlike for dynamic simulations. Therefore, the modeled technique proposed by [2] is based on a nonlinear curve fitting method [35].

In the first step, a lookup table (η_{cp}) together with the mass flow rate and differential pressure ratio, are used to find the efficiency of the compressor. The exiting air temperature is calculated from

$$T_{cp,out} = T_{atm} + \frac{T_{atm}}{\eta_{cp}} \left[\left(\frac{p_{sm}}{p_{atm}} \right)^{\frac{\gamma-1}{\gamma}} - 1 \right], \quad (2.29)$$

where the maximum efficiency of the compressor is 80%. By using thermodynamic equations, the torque of the compressor is calculated as

$$\tau_{cp} = \frac{C_p}{\omega_{cp}} \frac{T_{atm}}{\eta_{cp}} \left[\left(\frac{p_{sm}}{p_{atm}} \right)^{\frac{\gamma-1}{\gamma}} - 1 \right] W_{cp}, \quad (2.30)$$

where τ_{cp} is the torque in N-m, C_p is the specific heat capacity of air = 1004 J·kg⁻¹·K⁻¹, and γ is the heat capacity ratio of the air ($\gamma=1.4$).

A concentrated model of the rotational parameter is used to represent the compressor dynamic behavior

$$J_{cp} \frac{d\omega_{cp}}{dt} = (\tau_{cm} - \tau_{cp}), \quad (2.31)$$

where J_{cp} is inertia (kg·m²), ω_{cp} is the speed (rad/sec), and τ_{cm} is the torque input (N-m).

Finally, the compressor motor torque is calculated using the following static equation

$$\tau_{cm} = \eta_{cm} \frac{k_t}{R_{cm}} (v_{cm} - k_v \omega_{cp}), \quad (2.32)$$

where k_t , R_{cm} , and k_v are motor constants, v_{cm} is the feeding voltage and η_{cm} is the efficiency.

2.4.2 Lumped Model of the Manifold Dynamics

As shown in [2, 32], the lumped volume of the complete pipeline is referred to the manifold model. Therefore, the model have to take into account the volume of the compressor, connection pipes, humidifiers, and FC volume. The same analysis has to be done for the return manifold. In this work only the general expressions of this models will be given, for further details see the mentioned bibliography.

The manifold model is obtained by applying mass conservation. Therefore, we have

$$\frac{dm}{dt} = W_{in} - W_{out}, \quad (2.33)$$

where m is the amount of gas inside the manifold and W_{in} and W_{out} are the manifold inlet and outlet mass flow rates. Assuming the air temperature constant inside the manifold and moreover, of the same value as the incoming flow ($T = T_{in}$), we can write the following expression for the pressure dynamics

$$\frac{dp}{dt} = \frac{R_a T}{V} (W_{in} - W_{out}), \quad (2.34)$$

where the gas constant of the air is R_a and V is the total volume of the manifold. If we assumed that the temperature of the incoming gas change while it gets into the manifold, equation (2.34) can be written as

$$\frac{dp}{dt} = \frac{\gamma R_a}{V} (W_{in} T_{in} - W_{out} T). \quad (2.35)$$

By using the ideal gas law, m from (2.33), and p in (2.35), the temperature of the air is calculated (T). Therefore, we can used (2.34) if there is no temperature variation, or (2.33) and (2.35), if we face variation of the temperature gas in the manifold.

Chapter 3

FC Test Bench Design and Development

3.1 Introduction and Objectives

In order to experimentally verify the models and test controllers, a dedicated FC test bench is developed and implemented. The conceptualization of the FC test bench is restricted only for performing tests in proton exchange membrane (PEM) FC stacks. As is shown in the previous chapter, to test and characterize the model of a FC, one must be able to manipulate pressure, flow, temperature, stoichiometry, and humidity of the reactants and also temperature of the stack. Safe operation of the FC stack must also be taken into consideration while the test bench is designed. Therefore, dedicated hardware and software data acquisitions are developed and successfully implemented in the laboratory taking into consideration the limit operation values of the FC stack. In this chapter an overview of the experimental setup is given, also information about the data display interface is provided, and, in the last section, some experimental results to show the potential applications are performed. In section 3.2 the process subsystems, and all the instrumentation therein, are explained. In section 3.3 a complete description of the data acquisition, automation and display interface is given. As it was mentioned, in order to expose the potential application of the test bench is included, in section 3.4 some basic experimental tests are shown. The chapter is closed with some conclusions and remarks of the work.

In Fig. 3.1 the complexity of a system with the desired potentiality is depicted. The equipment and subsystems described in this chapter are the link between the

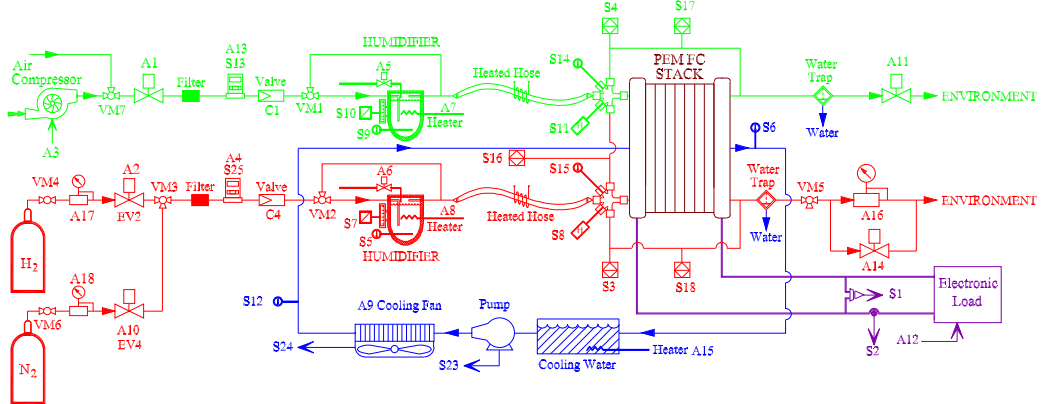


Figure 3.1: FC test bench diagram.

user and the operating conditions of the FC stack. Therefore, most of these devices and subsystems have a meaningful influence over the total system behavior.

3.1.1 FC Stack Specifications

The chosen FC stack is a PEM-FC-Stack of approximately 600 Watts. The stack is operated with air at the cathode and hydrogen in the anode. It is strongly recommended the use of $H_2 - N_2$ or $H_2 - CO_2$ mixtures for the examination of the stack performance under reformatte operations. A maximum concentration of 10 ppm of CO is allowed. In all cases, the valid anode and cathode pressure limits must be obeyed. The cooling media is demineralized water.



Figure 3.2: FC test bench diagram.

Table 3.1: Limit Operation values of the FC stack.

Variable	Limit value
Open cell voltage	$v_{cell} < 0.85 \text{ V}$
Under voltage	$v_{cell} < 0.5 \text{ V}$ then current reduce
Shut off voltage	$v_{cell} < 0.45 \text{ V}$ then cut off load
Maximum current	55 A
Maximum temperature	65°C cooling outlet
Maximum anode pressure (max p_{an})	1.5 bar _{abs}
Maximum cathode pressure (max p_{ca})	1.6 bar _{abs}
Maximum gas differential pressure	0.5 bar
Minimum H_2 flow	0.05 l/min/Cell, 50 to 70% utilization
Maximum H_2 flow	1 l/min/Cell
Minimum air flow	0.2 l/min/Cell, 20 to 40% utilization
Maximum air flow	5.8 l/min/Cell

The limit values, used to ensure safety operation, are shown in Table 3.1 and the main design and process characteristics of the FC stack are shown in Table 3.2.

Table 3.2: Design and process characteristics of the FC stack PEM-FC-Stack BZ 100.

<i>FC stack design</i>	
Type	Polymer exchange membrane fuel cell (PEM-FC)
Number of cells	20 cells
Active cell area	100 cm ²
Operating temperature	10 to 65°C
Nominal temperature	55°C
Operating Voltage	0.6 V/Cell (v_{cell})
<i>Media inlet</i>	
Cathode	humidified air with dew point between 25 and 45°C
Humidify medium	demineralized water, conductivity < 1 µS/cm
Anode	dry hydrogen
Cooling	demineralized water, conductivity < 5 µS/cm
<i>Gas utilization</i>	
Anode	40 – 90%
Cathode	25 – 40%
Open circuit voltage	0.95 V _{DC} /cell approximate
DC power (max)	35 W/Cell (depending on operating conditions)
DC nominal power	approximately 30 W/Cell at $v_{cell} = 0, 60$ V

3.2 Process Subsystems

In this section all the subsystems that are implicated in the electrochemical energy conversion process are presented, i.e., humidifiers, compressor, temperature regulating, and gas supply subsystems. For the selection of this equipment, the first step is to define the maximum output power of the FC stack. With this parameter it is possible to calculate the reactants flow (W_a and W_{H_2}), which is the starting point for the definition of the whole system. After clarifying this, the FC stack is specified, and with it, the maximum pressures of the reactants (cathode pressure p_{ca} and anode pressure p_{an}) and its differential limit. The temperature comes with the technical restrictions of the stack designer, even though this value

is tied to physical material specifications (*MEA* conforming materials). Finally, knowing the power, pressure, flow, and temperature of the FC stack, the compressor, humidifiers, fittings and, pipes can be designed. The temperature regulating subsystem must be specified according to the FC stack power and thermal characteristics, as it will be shown, the FC stack chosen for experimentation includes its custom cooling system. Fig. 3.1 depicts the gas supply system is composed of two different subsystems; the air pipeline (green) and the hydrogen pipeline (red). Although the instruments of both subsystems are similar, due to the characteristics of the gas and flow capacity, the operation of both pipelines is different. Only the main characteristics of the instruments will be mentioned in this section, for further technical information refer to the corresponding data sheets.

3.2.1 Humidifier Subsystems

In order to run the fuel cell system at any desired humidity degree, humidifiers are installed before the gas inlet of the FC stack. The schematics of the humidifier of the air inlet is shown in Fig. 3.3. This humidifier is filled with deionized water from a reservoir and automatically heated to the desired dew point temperature. The process air is fed through the humidifier core where it takes up the sufficient water. If this is not desired, a manual bypass valve (*MV*) allows air to be directly accessed into the heat-hose. Electric heating elements are powered and driven by electronic temperature controllers whose set-points are manually or automatically adjusted. The time constants for increasing temperatures are given by available heating power compared to the thermal inertia. As it is shown in Fig. 3.3, there

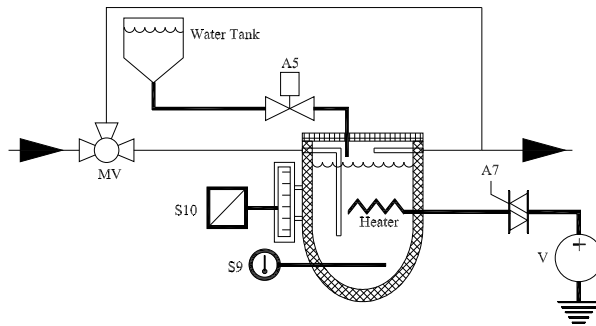


Figure 3.3: Humidification subsystem diagram.

is a subsystem to refill the bubbler, where sensor *S10* is a capacitive sensor that measures the level of water inside the humidifier, if the level is under the reference,

the electro valve (A_5) will open for a defined period of time. On the other hand, the adjustment of the temperature is achieved by sensing it with the thermocouple (S_9), later comparing the measurement with the reference and triggering the Triac. As it will be shown in a next section, the use of this particular electronic switch permits, not only on/off connection, but also continuous control of the power of the heater.

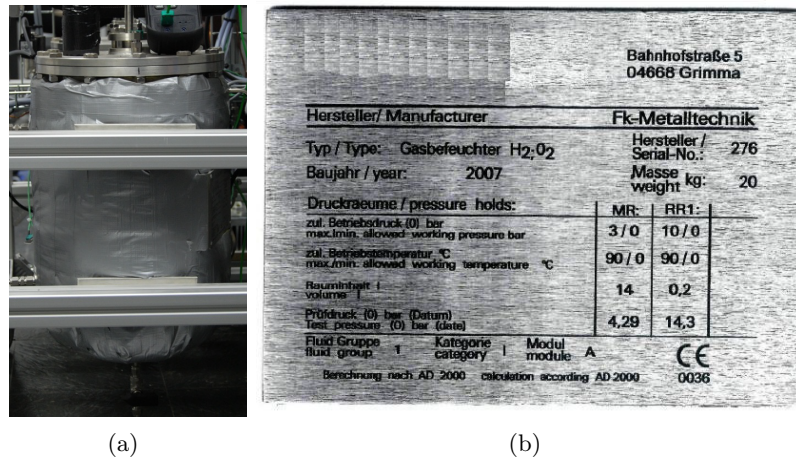


Figure 3.4: Humidifier used in the test bench. (a) Photograph of the humidifier. (b) Photograph of the plate data.

In Fig. 3.4 photographs of the humidifier and the plate data are shown. It can be seen that the maximum working temperature is 90°C and that the system can tolerate 10 bar maximum of input pressure.

3.2.2 Compressor Subsystem

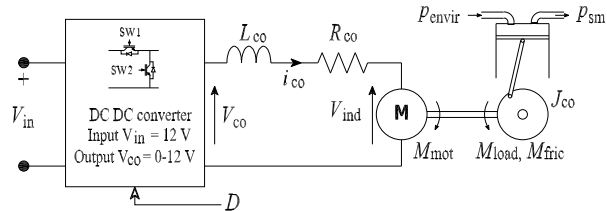


Figure 3.5: Compressor system diagram.

As it is shown in Fig. 3.5, the compressor subsystem is composed of a piston

compressor, a permanent magnet dc motor, and a power dc converter (buck converter). The topology enables full voltage control of V_{co} (0 to V_{dc}), with it, full speed control of the compressor and therefore, control of the air flow of the FC stack. The current dynamics of the compressor is given by

$$V_{in} \cdot D = L_{co} \frac{di_{co}}{dt} + R_{co} \cdot i_{co} + K_{b,co} \cdot \omega_{co}. \quad (3.1)$$

Where D is the duty cycle of the power converter and the control input of the system, and L_{co} , R_{co} , i_{co} , $K_{b,co}$ and, ω_{co} are the, series inductance, series resistance, current, constant, and speed of the motor, respectively. The voltage V_{in} is 12 V which is the nominal operation voltage of the FC stack and compressor, hence, the power converter must be a buck-converter. From the mechanical point of view, the speed dynamics are described by a torque balance on the compressor shaft, as it is shown in (3.2).

$$J_{co} \cdot \dot{\omega}_{co} = M_{mot} - M_{fric} - M_{load} \quad (3.2)$$

The load torque is proportional to the difference between the outlet and inlet pressure, and so it could be written as $K_{p,co} \cdot (p_{psm} - p_{envir})$. Measurements on the air compressor have shown an approximated linear relationship between compressor speed (ω_{co}) and the air flow rate (W_{air}). For more information about compressor dynamics, and moreover control design, refer to [36].

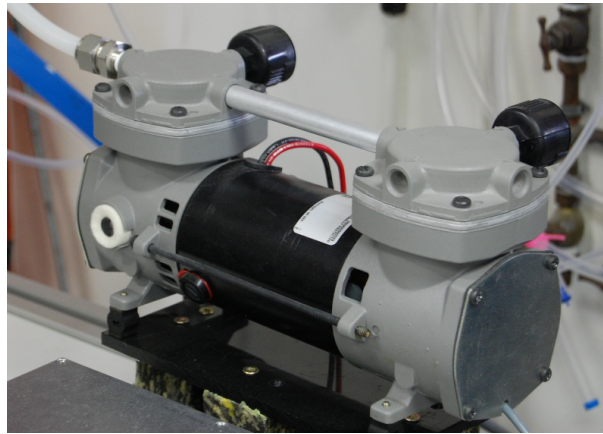


Figure 3.6: Compressor photograph.

The installed compressor is shown in Fig. 3.6, due to vibration issues, it can be seen that it is mounted over a motion isolator. According to the manufacturer's information the compressor fits the requirements of the FC stack and therefore, it is appropriate for energy balancing study and real application evaluation.

3.2.3 Temperature Regulating Subsystem

The temperature regulating system is shown in Fig. 3.7(a) This subsystem is composed of a cooling pipeline, a water pump, cooling fan, water container, controlled heater, and two temperature sensors (S_{12} and S_6). The system allows the warming of the FC stack up to the desired temperature (max 65°C measured by S_6), during this operation the cooling fan is turned off. While the stack is reaching the reference temperature, the Triac (A_{15}) gradually decreases the heater power until it disconnected from the voltage source. Since during a normal operation the FC stack is heated by the internal reaction, when the stack reaches the operation condition the heater is turned off and the cooling fan becomes the only means to regulate the temperature of the stack.

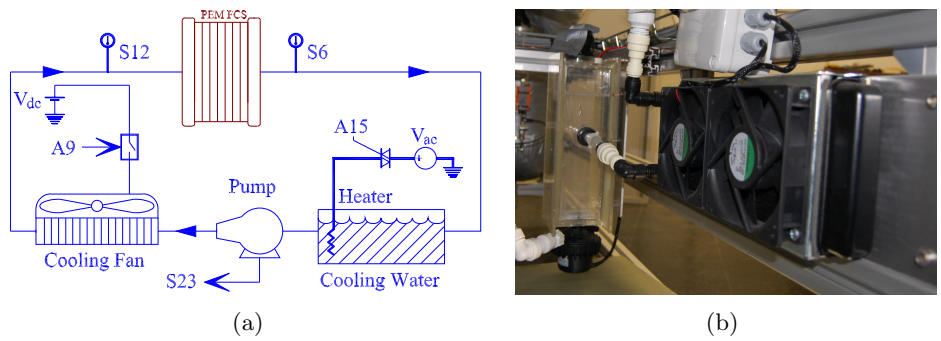


Figure 3.7: Temperature regulating system. (a) System diagram. (b) Photograph of the installed system.

It can be seen that the system has only two actuators, namely, the cooling fan (A_9) and the combination of Triac-heater (A_{15}), where A_9 is only an on/off connection while A_{15} allows continuous power control of the heater. Since this whole system is considered critical for a safe operation of the FC stack, the pump working signal and the temperature sensors (S_{23} , S_{12} and S_6) are connected to a protection block. Details of this block will be given in the section 3.3. In Fig. 3.7(b) is shown a photograph of the system installed in the test bench. The feeding voltage of the fan is 12 V dc, whereas the feeding voltage of the heater is 230 V ac, the operation with ac supply voltage permits the used of a Triac, which is a flexible device yet it has the disadvantage of introducing electromagnetic noise in the measurements.

3.2.4 Air Supply Subsystem

As shown in Fig. 3.8 the compressor and humidifier subsystems could be considered part of the air supply subsystem, yet due to their complexity they are analyzed separately in sections 3.2.2 and 3.2.1, respectively. From left to right in Fig. 3.8 the following components can be seen; the compressor subsystem (that appears as an actuator of the air supply subsystem) (A_3), manual interchange valve (VM_7), electronic valve (A_1), gas filter, mass-flow controller ($A_{13} - S_{13}$), protection valve (C_1), manual interchange valve (VM_1), humidifier with its corresponding sensors and actuators (S_9, S_{10}, A_5 and A_7), heated hose, temperature sensor (S_{14}), humidity sensor (S_{11}), absolute pressure sensor (S_4), differential pressure sensors (S_{16} and S_{17}), water trap and an electronic valve (A_{11}).

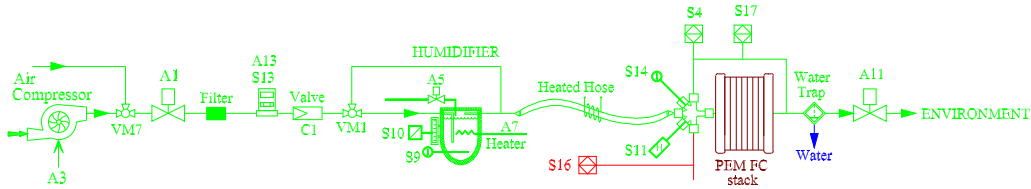


Figure 3.8: Scheme of the air supply subsystem where, the letter A stands for actuator and S for sensor.

In order to enable the utilization of industrial air (bottles of 200 bar), the manual valve VM_7 has been disposed. Although it seems to be redundant with VM_7 , the electronic valve A_1 is critical for a safe operation of the system, since this device can be automatically driven, it is interconnected with the protection block (explained section 3.3.2) and used as a protection device. Due to the utilization of compressed air, the installation of a low pressure drop filter is also critical for the operation, in this case a $7 \mu\text{m}$ filter is setup. One of the main instruments of this subsystem is the mass-flow controller $A_{13} - S_{13}$, this instrument can be used as a sensor and/or an actuator (it can measure the flow and/or control it), as will be seen in section 3.3.2, the flow is controlled by the compressor and so the mass-flow controller will be used as a flow sensor to close the flow control loop. To avoid reverse flow, which can harm some instruments, a valve (C_1) of low pressure drop is installed in series with the pipeline. To test the FC stack with dry air, a valve VM_1 is installed, it permits to bypass the humidifier and introduces the air directly into the FC stack. Given that the gas humidity is sensitive to temperature variations, the connection between the humidifier and the inlet fitting of the FC stack is done with a special self-heated hose that avoids

the condensation by keeping the temperature constant along it. To monitor the temperature of the inlet gas, directly in the fitting there is a type *K* thermocouple (*S14*) installed. Also in the fitting connection a humidity sensor is installed, this particular instrument is composed of a probe (*S11*) and a signal conditioning box that displays the measurement on its screen and also wires the signal to the acquisition system. Three pressure sensors are installed in the air intake of the FC stack, an absolute pressure sensor (*S4*), a differential between the input and exit of air (*S17*), and a differential between the air intake and the hydrogen intake (*S16*). On the air output of the Stack a water trap device and an electronic valve (*A11*) are installed, for operational and safety conditions, respectively.

3.2.5 Hydrogen Supply Subsystem

Fig. 3.9 depicts the connection of the instrumentation and subsystems of the H_2 pipeline. As in the case of the air pipeline, the humidifier subsystem is also used in the H_2 supply subsystem. From left to right in Fig. 3.9 one can see; the bottles of hydrogen and nitrogen with their manual valves (*VM4* and *VM6*), manual pressure regulators (*A17* and *A18*), and electronic valves (*A2* and *A10*), a manual valve (*VM3*), a gas filter, mass-flow controller (*A4*), protection valve (*C4*), manual interchange valve (*VM2*), humidifier with its corresponding sensors and actuators (*S7*, *S5*, *A6* and *A8*), heated hose, temperature sensor (*S15*), humidity sensor (*S8*), absolute pressure sensor (*S3*), differential pressure sensors (*S16* and *S18*), water trap, manual interchange valve (*VM5*), and a manual pressure regulator (*A16*) in a parallel connection with an electric valve (*A14*).

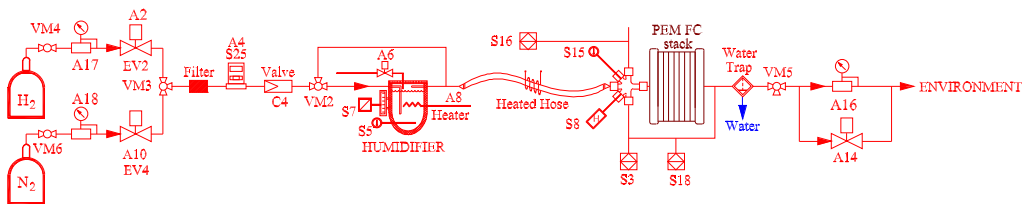


Figure 3.9: Scheme of the H_2 supply subsystem.

The connection of a 200 bar gas bottle requires the utilization of a manual valve and a manual pressure regulator in order to reduce the pressure to the appropriate value for the system. It can be seen in Fig. 3.9 that, by means of *VM3*, it is possible to exchange between H_2 and N_2 . The insertion of N_2 into the pipeline is executed only after the utilization and is part of the turning off

procedure of the system in order to expel the remaining H_2 . The use of a gas filter is a precautionary measure, even though H_2 and N_2 are almost 100% pure, at the moment of the connection of the pipes (when the pipelines are open to the environment) dust contamination can occur. One of the main instruments of the subsystem is the mass-flow $A4 - S25$, in this case the instrument is used as an actuator to control the flow of hydrogen in the pipeline, the importance and operational use of $A4$ is described in detail in section 3.3.2. In the same way as in the air pipeline, H_2 subsystem contains a security valve (to avoid reverse flow) and a humidifier subsystem with its corresponding sensors ($S5$ and $S7$) and actuators ($A6$ and $A8$). By means of the manual valve $VM2$ it is possible to bypass the humidifier and introduce dry H_2 into the stack. The heated hose used to transport the gas from the humidifier to inlet fitting, is used also to avoid condensation when humidified H_2 is used, or to warm up the gas in case of using dry H_2 . The temperature sensor installed in the inlet fitting of the FC stack ($S15$) is a type K thermocouple sensor. The absolute pressure sensor $S3$ is installed for safety and operational reasons. The measurement of absolute pressure is used to protect the system in case of exceeding the limit tolerated by the stack, this measurement can also be used to control the power delivered by the FC stack. As in the case of the absolute pressure sensor, the differential sensor $S16$ (between H_2 and air) has safety and operational purposes. In the present work, the measurement of $S16$ is used to protect the system in case of exceeding the differential pressure limit of the stack, yet it is a common practice to control the FC stack chemical reaction by differential pressure. The differential pressure sensor $S18$ is installed to measure the pressure drop inside the FC stack. At the H_2 output, a water trap is installed to extract the liquid water that comes with the remaining gas. In the case of using a feedback of the remaining H_2 into the system, the manual switch valve $VM5$ is installed. Finally, the parallel assembly of the manual pressure regulator $A16$ and the electric valve $A14$ allows to increase the output pressure of hydrogen. This can be done by closing $A14$ and regulating the pressure with $A16$. In case of exceeding the limit pressure tolerated by the stack, $A14$ will be automatically opened and in this way it is possible to run a safe operational test.

3.3 Acquisition, Automation, and Data Display

In this section an overview of the signal conditioning is presented, this includes the specification of the communication standard of sensors and actuators, and

the design and implementation of the printed circuit board (PCB) designed to conditioned the signals. Also in this section the programmed logic of control and protection of the system is presented, control loops, as the temperature of the bubbler, or the air flow are explained together with the protection block. Finally, a brief description of the control panel designed for online control of the test bench is included, here the warning measurement and the general display of the screen are considered.

3.3.1 Data Acquisition

The main challenge from this point of view is the interconnection of a development acquisition card (dSPACE) with industrial standard instrumentation (electric valves or pressure sensors). Since the main restrictions are imposed by the dSPACE card, which main characteristics are shown in Table 3.3, as an starting point it is assumed that the output signal of all sensors must be adapted to range from -10 to 10 volts and the driving signal of the actuators must be adapted to a voltage range of -10 to 10 and ± 5 A maximum of current demand. This last restriction is critical, so special care must be taken in order not to exceed the maximum delivered power of the card.

Table 3.3: dSPACE acquisition card main characteristics.

Board	Channels	Resolution	Sampling time	Sampling time (all channels)
DS2002 A/D Board	32 in	4,8,12,16 bit, shortcycling	5.0 μ sec (16 bit)	93.5 μ sec (16 bit)
DS2103 A/D Board	32 out	14 bit	10 μ sec	

Pressure Measure

The pressure sensors communication standard is the industrial current signal, linear and in the range of 4 to 20 mA, where 4 mA is the current for the lower value of the pressure range (0 bar), and 20 mA is the current for the maximum value of the pressure range (2 bar). To convert this measurement into a 0 to 10 V signal, the circuit shown on Fig. 3.10 is implemented. For further information about components and PCB layout see Appendix A.0.1.

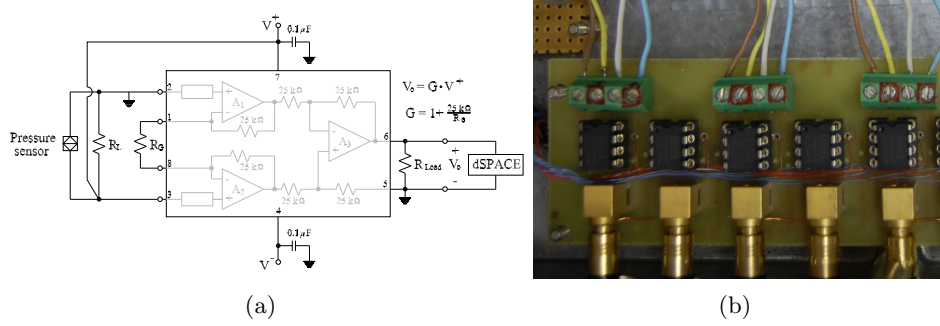


Figure 3.10: 4 – 20 mA to 0 – 10 V PCB circuit converter. (a) Layout of the designed circuit. (b) Photograph of the final PCB.

In Fig. 3.10(a) the feeding voltage (V^+) is 12 V therefore, R_L is 100 ohm. To keep the upper range of the measurement under 10 V, the value of R_G must be greater or equal to 12.5 kΩ. Since the maximum pressure allowed is 1.6 bar, the chosen value of R_G is 11 kΩ and so, 1.6 bar implies 9.316 V in the dSAPCE.

Humidity Sensors

The special features of the humidity sensors make it possible to directly connect the output signal to the acquisition card. The design of the instrument make possible to set a linear output signal range from 0 to 10 volts , by the appropriate internal configurations. Hence, 0 degree of relative humidity is 0 volts output and 100 relative humidity is equal to 10 volts in the output. Special care has to be taken in the installation since each instrument is calibrated for a specific gas, therefore two devices are installed, one for air and the other for H_2 , as shown in Fig. 3.11(a).

Mass-Flow Controllers

Due to its technical characteristics the mass-flow controllers must be customized by the vendor, the instrument is adjusted for each gas (air and H_2), the communication standard is selected, and the scale length is established. In the case of the air, the instrument characteristics are

- Air type,
- Scale Length is 120 liters/minute,
- Output signal from 0 to 5 volts,



Figure 3.11: Humidity sensor and mass-flow controllers. (a) Photograph of the humidity sensor. (b) Photograph of the mass flow controller of air.

Input signal from 0 to 5 volts,

and for the mass-flow controller of H_2 , the characteristics of the instrument are

Hydrogen type,

Scale Length is 20 liters/minute,

Output signal from 0 to 5 volts,

Input signal from 0 to 5 volts.

Notice that, since the instrument is a sensor and an actuator, there is a signal of measurement and a signal for the desired reference. Given that there is a linear relationship between the signal and the measurement; in the case of the air measurement, 0 liters/minute is 0 V and 120 liters/minute is 5 V, and for the H_2 measurement, 0 liters/minute is 0 V and 20 liters/minute is 5 V.

Temperature Measurement

The temperature measurements are ruled by the characteristics of probe used in the implementation. In this case, the probes used are metal joint thermocouple type K, hence the signal obtained from the probe is approximately 2.022 mV at 50° C. As it is expected, the level of the signal make it sensitive to electromagnetic noise, in addition, the signal coming from the probe is not linear respect to the temperature variation. Due to this reason, the wiring and conditioning of the signal is critical. In order to solve the temperature measurement problem two different approaches were taken.

The first approach is the design of a PCB with a thermocouple conditioner chip (*AD597*). The *AD597* is a special conditioner for type K thermocouple, it

linearizes the output to a signal between 0 to 1,005 V in the range from 0 to 100°C. The layout of the circuit and the photograph of the final PCB, are presented in Fig. 3.12. It can be seen in the figure that the output of the *AD597* circuit is passed through a low-pass filter. Technical information about the PCB design layout are included in Appendix A.0.2

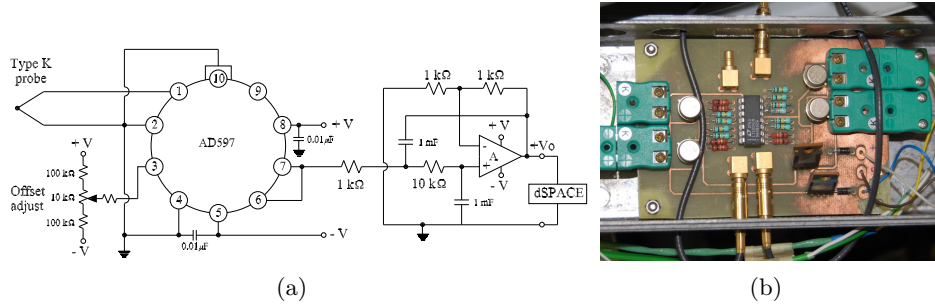


Figure 3.12: Temperature conditioning circuit and PCB. (a) Basic circuit of the signal conditioner. (b) Photograph of the final PCB.

Since the designed circuit needed to be regularly calibrated and it is susceptible to magnetic contamination, a new solution is implemented. The new setup is based on the utilization of an instrument specifically for thermocouple (type J and K) conditioning. Its special features, like the flexibility for choosing the scale length (0 to 400°C), one calibration, linear output range from 0 to 10 V makes this device suitable for the application.

Cell Voltage Measurement

The cells voltage and the total FC stack voltage are critical variables from the point of view of operation, diagnostic, and protection. Not only the overall stack voltage, but also cell individual voltage has a warning minimum and a disconnection minimum voltage (see Table 3.1). Therefore, the objective in this respect is to sense differential voltage in the 20 cells of the stack. This operation must be done considering that there is a limited amount of available ports in the acquisition card, and that the ports of the acquisition card have a common earth. It should also have to be considered that the maximum voltage of the stack is 17 V, hence the polarization voltage of the designed circuit must be more than this value to avoid saturation.

To achieve the mentioned objectives, a multiplex based PCB circuit is de-

signed and implemented. The used multiplexer is the ADG732, this device has 32 channels that can be addressed by 5 inputs, therefore, 5 outputs and 1 input of the card are used. The operation frequency of the multiplexor is 18 MHz, the sampling time (T_s) of the acquisition card is $200e^{-6}$ s, and every 1000 samples the multiplexer addresses another cell. Therefore, every 0.2 s the multiplexor changes from cell to cell. Fig. 3.13 depicts the experimental result of the cells voltage measurement, there is a clear maximum deviation of 0.1 V (approximately) between the voltages of the cells.

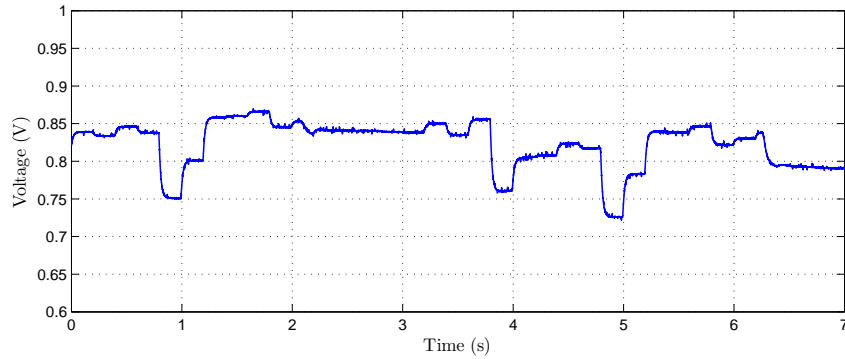


Figure 3.13: Experimental result of the multiplexed measurement of the cell voltages.

A block representation of the circuit is shown in Fig. 3.14, it can be seen that the final PCB is composed by the following three stages:

- 1- Differential amplifiers stage, where the cell voltage is measured and amplified.
- 2- Analog multiplexer, where each cell is addressed by 5 outputs of the dSPACE.
- 3- Filter amplifier stage, in which the signal is passed by a low-pass filter (cut frequency= 106 Hz) and later amplified (gain= 8.33).

Technical information about the PCB design can be found in the Appendix.

Solenoid Valves Driving

The solenoid valves are driven by connecting or disconnecting the 24 V solenoid, furthermore the demanded power of each valve is approximately 15 W, therefore is not possible to directly connect the analog output of the acquisition card to the solenoid of the valves. In order to drive the electric valves, an intermediate circuit

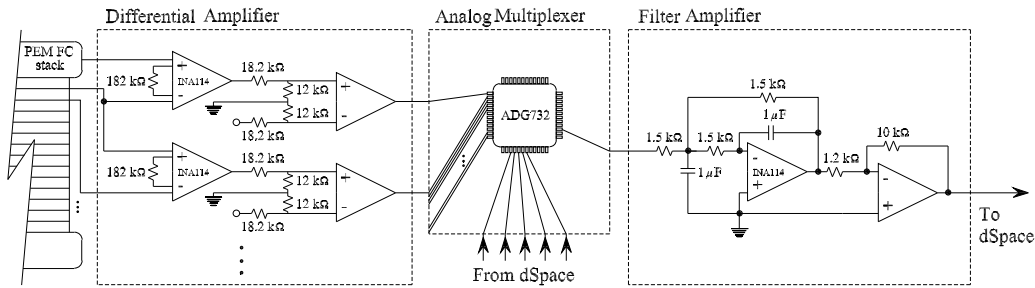


Figure 3.14: Block diagram of the voltage conditioning circuit (this a representation and not the real PCB layout).

based on solid state relays is used, in this way the acquisition card operates an electronic switch to connect or disconnect the solenoid valves. The main features of this relay are:

- The nominal input operation voltage is 5 V.
- The control input operation current is 7 mA.
- The output operation voltage 240 V.
- The output operation current 2 A.

Heaters Actuator

As in the case of the solenoid valves, due to the electric characteristics of the heaters used for temperature regulating, the utilization of intermediate power relay is necessary to drive them using the acquisition card. Different types of heater devices are used in the implementation, and therefore, they have unequal electric characteristics (see Table 3.4)

Table 3.4: Characteristics of heater devices.

Used	Power	Voltage	Current	Connection
Bubbler air	3000 W	230 Vac	13 A	Triac
Bubbler H ₂	1500 W	230 Vac	7 A	Relay
FC temperature	300 W	230 Vac	1.3 A	Triac
Heated hose air	150 W	230 Vac	0.65 A	Relay
Heated hose H ₂	150 W	230 Vac	0.65 A	Relay
Fitting tracer air	50 W	230 Vac	0.22 A	Relay
Fitting tracer H ₂	50 W	230 Vac	0.22 A	Relay

Since all heaters are fed by 230 Vac the remaining issue is the utilization of the appropriate technology. Given that the triac allows continuous power control and its main characteristics (40 A load capacity at 400 V) makes this device suitable for all the applications, the two available triac units are used in the most critical applications (see table). In this way, continuous control is applied for controlling the temperature of the FC stack and of the air bubbler. Although the relay allows only the connection of the full power or the absolute disconnection of the heater, it is appropriately suited to the applications of the system.

Photograph of both, the triac and relay implementations are shown in Fig. 3.15. The driving voltage of the triac is 0 to 5 V, therefore 0 volts means 0 power delivered and 5 V signal (coming from the acquisition card) means full power. Further details about the heater control and operation is described in the next section. 3.3.2.

3.3.2 Control Loops and Protection Block

In this section, an overview of the control loops (gas flow and the humidity) and the protection subsystem block is given. Regarding the control strategy, the calculation of the references and the design of the controllers is explained. Concerning to the protection block, the logic, limit values, and warning conditions programmed block in Matlab Simulink are explained. The limit values and warnings are given by the manufacturers of the FC stack, see tables 3.2 and 3.1 for details.

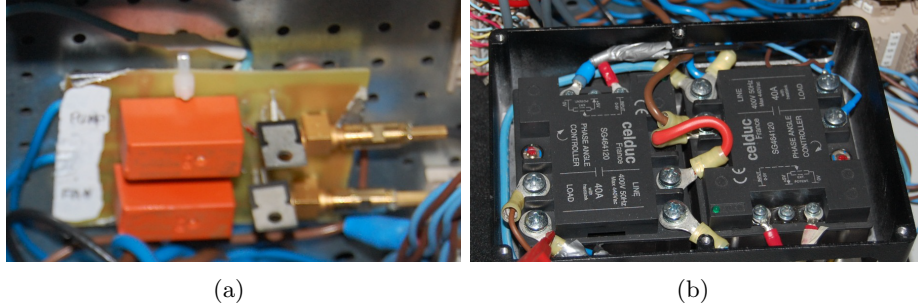


Figure 3.15: Actuators used to drive power heaters. (a) Photograph of electromechanical relay. (b) Photograph of the triac modules.

Air Humidity Control Scheme

Since there is a tight relationship between the relative humidity (RH) and the temperature of the gas, the most precise way to control the humidity of the gas (with a bubbler based humidifier system) is by measuring and controlling the temperature all along the gas course, i.e. bubbler water, heated hose, connection fitting, and FC stack.

$$\begin{aligned} T_d &= \frac{b\gamma(T, RH)}{a - \gamma(T, RH)}, \\ \gamma(T, RH) &= \frac{aT}{b + T} + \ln \left[\frac{RH}{100} \right], \end{aligned} \quad (3.3)$$

where

T_d = Dew point,

T = Temperature of the gas,

RH = Relative Humidity,

$a = 17.27$, and $b = 237.7^\circ\text{C}$.

Equation (3.3) is only valid for

$0^\circ\text{C} < T < 60^\circ\text{C}$,

$1\% < RH < 100\%$, and

$0^\circ\text{C} < T_d < 50^\circ\text{C}$.

As it is given in (3.3) the dew point (or temperature of saturation) depends on the actual temperature and the relative humidity of the gas. Since it is desirable to keep the temperature of the FC stack controlled (mostly in its higher value), equation (3.3) is used to calculate the temperature of the humidifier for a desired

RH of the gas. As it is shown in Fig. 3.16 the temperature of the humidifier is calculated and compare with the reference, later on, the temperature error (\tilde{T}) is passed through the control block and the output of this block is directly the firing angle of the triac that modulates the power of the heater.

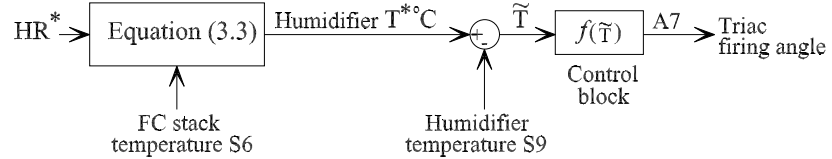


Figure 3.16: Air humidity control diagram.

The control technique, programmed in Simulink, is a saturated proportional plus an hysteresis band. The function in the block diagram ($f(\tilde{T})$) works as follows:

$$\begin{aligned}
 &\text{if } 20^\circ\text{C} < \tilde{T} \Rightarrow \text{output} = 5 \text{ V}, \\
 &\text{if } 1^\circ\text{C} < \tilde{T} < 20^\circ\text{C} \Rightarrow \text{output} = 0.25 \times \tilde{T} \text{ V}, \\
 &\text{if } -1^\circ\text{C} < \tilde{T} < 1^\circ\text{C} \Rightarrow \text{hysteresis band } 0.25 \text{ V output}.
 \end{aligned}$$

Notice that the main objective of this control technique is to reach gradually the operating temperature and then apply a hysteresis band, but without using the full power of the heater.

Hydrogen and Air Flow Control

As it is shown in technical literature [2, 20], a common practice to control fuel cell reaction, and consequently, the power delivered by the FC stack is done by controlling the air flow (W_{air}) and then controlling the pressure across the membrane (Δp_{membr}) by controlling the flow of hydrogen (W_{H_2}). This strategy is possible due to the slow dynamics of the air flow compared to the dynamics of hydrogen flow. With the purpose of evaluation, the strategy applied in this work is based

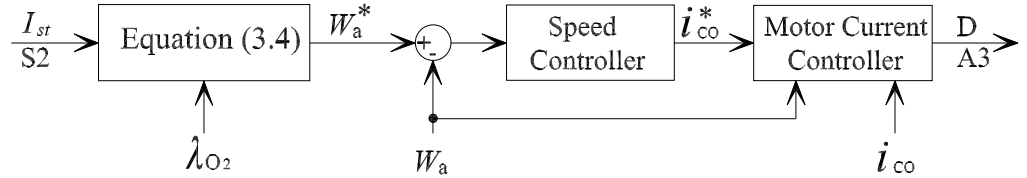


Figure 3.17: Air flow controller block diagram.

on W_a and W_{H_2} tracking. As shown in Fig. 3.17, for controlling W_a the stack current I_{st} is measured, the air stoichiometry (λ_{air}) is set, and by means of (3.4) the air flow reference (W_a^*) is obtained. In order to track this reference, a Sliding-Mode super-twisting and a PI controllers are used for controlling the speed and the compressor current, respectively. The output of the controller is the duty cycle (D) of the dc-dc converter depicted in Fig. 3.5 and D is proportional to the feeding compressor voltage (V_{co}). For further details about the compressor controller design, refer to [36].

The equation used to calculate the air flow is the following,

$$\begin{aligned} W_{O_2} \left[\frac{gr}{s} \right] &= (\lambda_{O_2} \cdot N_{cell} \cdot I_{st}) / (4 \cdot F_{ct}), \\ W_a \left[\frac{NL}{min} \right] &= \frac{(W_{O_2} \left[\frac{gr}{s} \right]) \cdot R \cdot T_N \cdot 60}{O_{2MM} \cdot p_N \cdot \text{Air}(\%_{O_2})}, \end{aligned} \quad (3.4)$$

where N_{cell} is the number of cells of the stack, F_{ct} is the Faraday constant, R is the ideal gas constant, T_N is the temperature expressed in kelvin, O_{2MM} is the molar mass of oxygen, p_N is the pressure, and $\text{Air}(\%_{O_2})$ is the percentage of oxygen contained on the air.

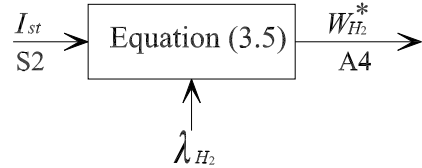


Figure 3.18: H_2 flow controller block diagram.

The equations that defines hydrogen flow is,

$$\begin{aligned} W_{H_2} \left[\frac{gr}{s} \right] &= (\lambda_{H_2} \cdot N_{cell} \cdot I_{st}) / (2 \cdot F_{ct}), \\ W_{H_2} \left[\frac{NL}{min} \right] &= \frac{(W_{H_2} \left[\frac{gr}{s} \right]) \cdot R \cdot T_N \cdot 60}{H_{2MM} \cdot p_N}, \end{aligned} \quad (3.5)$$

where N_{cell} is the number of cells of the stack, F_{ct} is the Faraday constant, R is the ideal gas constant, T_N is the temperature expressed in kelvin, H_{2MM} is the molar mass of oxygen, and p_N is the pressure. The subscript N is referred to the standard normal conditions.

Since H_2 is contained in high pressure bottles, the control of W_{H_2} requires only an adjustable valve or the utilization of a mass flow controller (denoted as A4 in Fig. 3.9). Fig. 3.18 shows the strategy used to control W_{H_2} , as a block diagram.

In the same way as the air reference is obtained, $W_{H_2}^*$ is calculated from (3.5) by replacing I_{st} and the H_2 stoichiometry (λ_{H_2}). The reference $W_{H_2}^*$ is given to the mass flow controller as a set-point and the instrument will automatically track this value.

Protection Block Subsystem

The protection block (depicted in Fig. 3.19) is a programmed logic of the limit of tolerable values of the FC stack and also operational working conditions, e.g., the cooling system operation. The tolerable limit values of the FC stack are shown in Table 3.1. The logic operates in such a way that, whatever condition

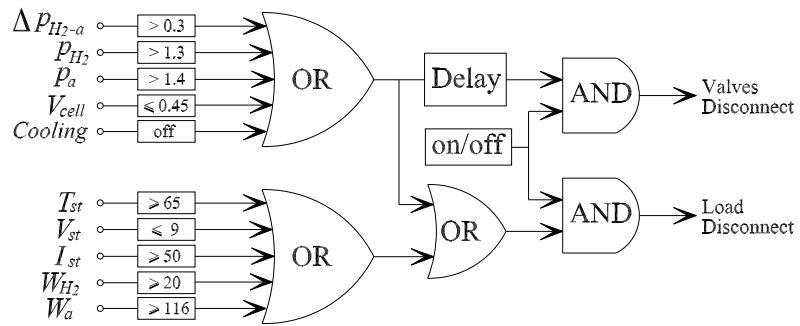


Figure 3.19: Block diagram of the fuel cell stack protection logic.

that is achieved will generate a logic 1 output, this output is turned into the disconnection of the electric load or the disconnection of the electric load and the gas feeding. The purpose of discriminating between the gas supply and the electric load disconnection is to avoid the operation of the FC stack without, or not enough, gas provision. As it is shown in [1] and [20], it is critical for a safe operation to keep enough gas supply whenever the electric load is connected. Therefore, the gas will be cut only if it is extremely necessary. Following the same strategy, when is inevitable to stop the gas supply due to over pressure or under voltage in one of the cells (V_{cell}), a small delay (of two sampling times) is added to ensure that the electric load is disconnected before the gas supply.

3.3.3 Data Display

The dSPACE data display software has all the necessary features to develop a complete online control panel, its flexibility and graphic attributes make it possible, not only to display meaningful information, but also to manipulate operational

variables. In Fig. 3.20 the main control panel screen (CPS) is shown. In the left side of the CPS three time varying graphs have been disposed, from top to bottom, the load current, air flow and air flow reference (W_a and W_a^*), and the measurements of voltage in each cell of the stack. The refreshing time of these graphs is chosen to be 10 seconds but, depending on the variable and the experiment, this time could be modified.

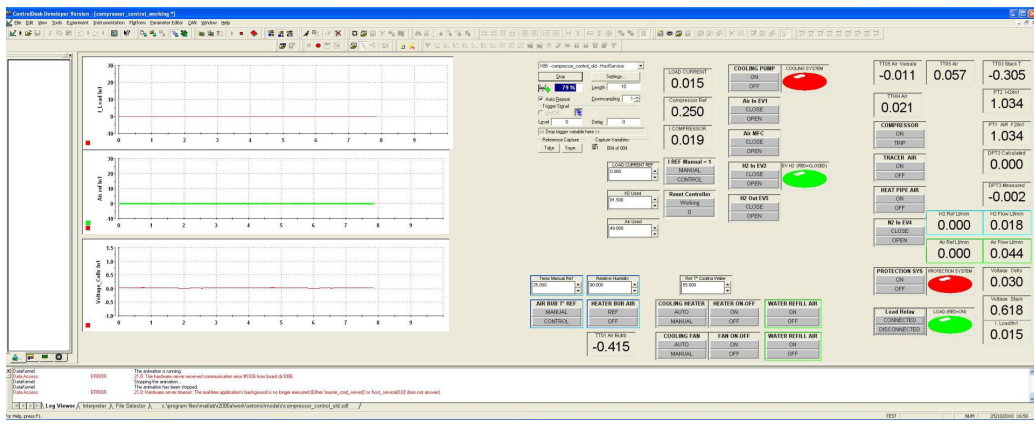


Figure 3.20: Control panel displayed on screen for monitoring and online control.

In the center of the CPS most operational variables have been disposed. In the upper center part, a sequence of commands to perform a cool startup of the system can be seen, first the cooling system has to be turned-on, then the electronic valves of air, air MFC, and H₂ input, must be opened. With the purpose of testing the controller, in the center of the CPS the option of a manual load current reference is added. To test different operational working points, the option of changing the stoichiometry of H₂ and air is also integrated. The variables related with the temperature regulation, and therefore the humidity set-points of the gases, are located in the center bottom of the CPS. Using these features it is possible to change the temperature reference of the bubblers and the FC stack manually or automatically, this by introducing a reference of humidity. In the right side of the CPS some actuators can be found (tracer, heat pipe, protection system, and electric load connection), and in extreme right side of the screen, a column of the main measurements to be aware-of is disposed.

3.4 Experimental Results

To demonstrate the united operation of the system and furthermore, to show the potential applications of the test bench, some experimental tests are presented in this section. The first test is to obtain the characteristic curve of the FC stack in an operation point, the second experimental work is the determination of the complex impedance of the stack by analyzing the spectrum of the output voltage and current, and finally a close loop operation of the system is presented.

3.4.1 Experimental Characteristic Curve

As shown in the previous chapter, the characteristic curve of a FC stack has a strong dependency on the pressure and temperature and is less influenced by the humidity of the membrane. In Fig. 3.21 the characteristic curve obtained by experimentation and the characteristic curve given by the manufacturer of the stack are depicted. The experimental shape is obtained in the operation point

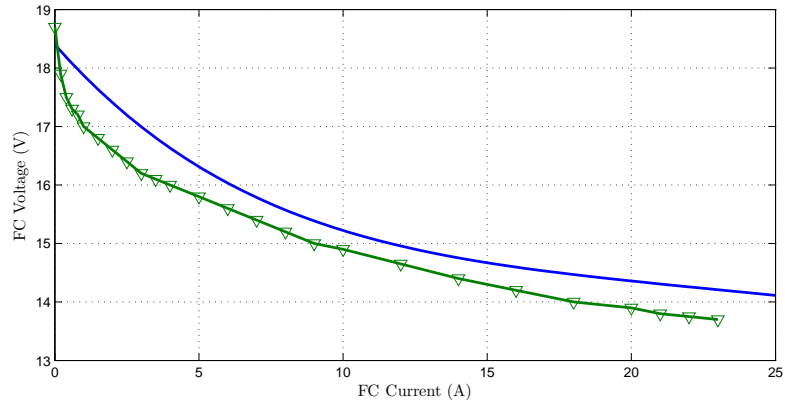


Figure 3.21: Characteristic curve (current vs voltage) of the FC stack in one operating point. The experimental results (green) and the manufacturer characteristic shape (blue) are shown.

at a temperature of 52.3°C and 1.04 bar pressure of air and H_2 supply. The slight difference between both characteristic curves is due to the difference in the operating point, not only on temperature and pressure but also on the humidity of the FC stack.

3.4.2 Equivalent Impedance

As it is shown in the literature [37, 38, 39] there is a close relationship between the complex internal impedance of the fuel cell and the state-of-health and, more specifically, with the water managed inside the FC stack. Using fast Fourier transformation in order to obtain the internal impedance of the fuel cell, a new online method of state-of-health monitoring is proposed. Initial simulation analysis of the method are included and later, the evaluation of the strategy using experimental data from the FC stack, are shown.

Simulation

An alternative method to make fuel cell impedance (Z_{st}) ac sweep is proposed taking advantage of the flexibility given by a power scheme as the one shown in Fig. 3.22. The main objective is to take advantage of output current variations (I_{st}) of the fuel cell in order to calculate Z_{st} . The procedure is based on the fact that any step of I_{st} contains enough frequency spectrum needed to map the internal impedance of the fuel cell. The discrete Fourier transformation (DFT) is applied in the terminal voltage (V_{st}) and output current, afterwards the calculation of Z_{st} is straightforward by calculating the impedance for each frequency. This methodology is feasible to be applied by profiting of the natural electric load variations or by imposing a small perturbation in the output voltage reference of the converter (V_o^*). In order to test this technique, the system shown in Fig. 3.22 is simulated in close loop using a control strategy shown in [40, 41].

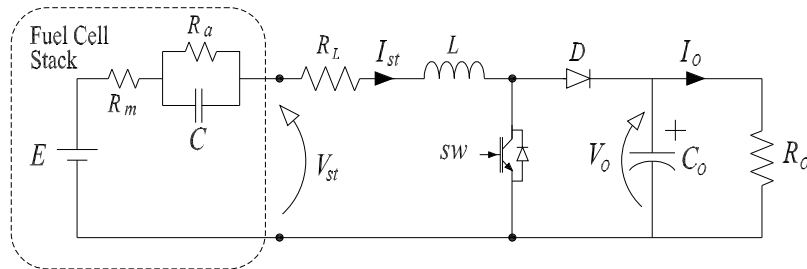
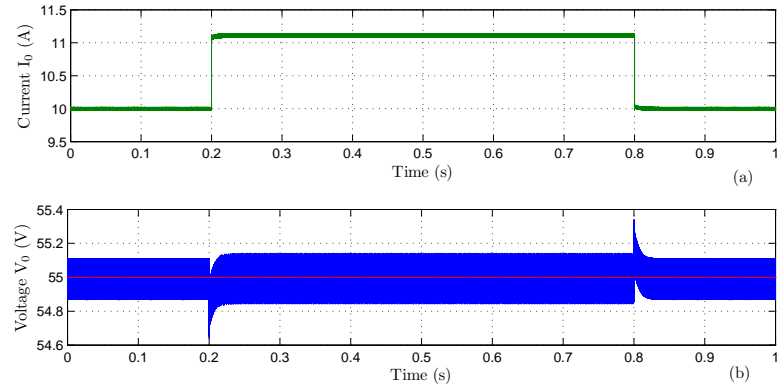


Figure 3.22: Example of an electric power connection of FC with load through a dc dc converter.

Fig. 3.23 depicts the load change imposed in order to introduce a perturbation in the FC stack output V_{st} and I_{st} . In Fig. 3.23(a) the step current of 10% imposed over the electric load during 0.6 s, i.e. changing the resistive load from 5.5 to 4.95

Table 3.5: Parameters of the power circuit Fig. 3.22 obtained from [42]

Parameter	magnitude
E	35 V
R_a	250 mΩ
R_m	50 mΩ
C	10 mF
R_L	5 mΩ
L	200 mH
C_0	900 μF
R_0	5.5 Ω

Figure 3.23: Load current and voltage of the system. (a) Output voltage in the capacitor C_o . (b) Output load current.

ohm. The voltage reference (in red) and the load voltage (V_o in blue) are shown in Fig. 3.23(b), as in real applications, the controller regulates the voltage in the load so it can track the reference and only during the transition an error is produced. In Fig. 3.24 the I_{st} and V_{st} are presented, due to the variation of the electric load, changes over the terminal voltage and current supply of the FC stack can be detected. As can be seen in Fig. 3.24(a), the load power increment produces an increase of the power supplied by the FC stack, and therefore, I_{st} raises up to 21.7 A average. Consequently with the I_{st} increment, and due to the internal impedance of the FC stack, a voltage drop of V_{st} is produced (V_{st} is reduced from 29.45 to 28.55 V in average), this result is shown in Fig. 3.24(b). The result of

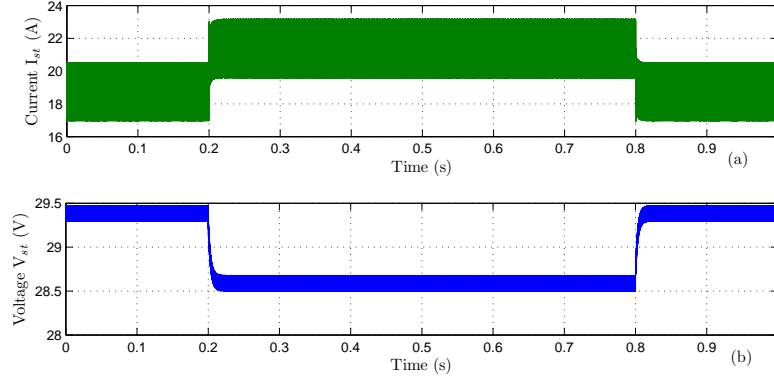


Figure 3.24: Output current and voltage of the FC stack. (a) Output current (I_{st}). (b) Voltage in the terminals of the FC (V_{st}).

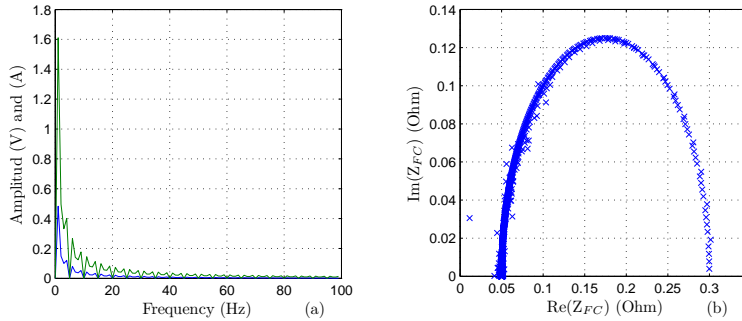


Figure 3.25: Simulation frequency analysis of the output voltage and current of the FC stack. (a) Frequency spectrum of current (green) and voltage (blue). (b) Real vs Imaginary plot of the internal impedance of the FC stack.

the frequency spectrum analysis is presented in Fig. 3.25. In Fig. 3.25(a) the frequency spectrum of V_{st} and I_{st} are shown in blue and green, respectively. In order to show appropriately the magnitude at different frequencies, the dc value (frequency 0) has been taken from the graph. The graph of *real* vs *imaginary* FC stack impedance is shown in Fig. 3.25(b), since the analysis has been done in ideal conditions the plot is a parabola, and as it is known from the literature this shape can be modified due to different operation conditions, e.g., water internal accumulation or changes on the operating point.

Experimentation

The experiment is accomplished as follows;

- a- The FC stack is connected directly to a constant current source set to 10.1 s,
- b- The current source is initially off,
- c- The FC stack is stabilized in an operating point, 53°C, 95% RH, 1.03 bar p_{H_2} , and 1.03 bar p_a
- d- The FC stack operates in an open loop, i.e., the operation variables do not change with the electric load variations,
- e- The acquisition system is turned on and after 10 s the electric load is connected.

To obtain the internal impedance of the FC stack, the step current variation (shown in Fig. 3.26(a)) is imposed, and the same mathematical analysis explained in section 3.4.2 is used to calculate the complex values of I_{st} and V_{st} . The variation of I_{st} causes the voltage decrease depicted in Fig. 3.26(b), as can be seen in both figures, while I_{st} grows from 0 to almost 10 A_{avg} (at 10.1 s), a voltage drop of approximately 3.8 V is produced (from 18.5 V_{avg} to 14.7 V_{avg})

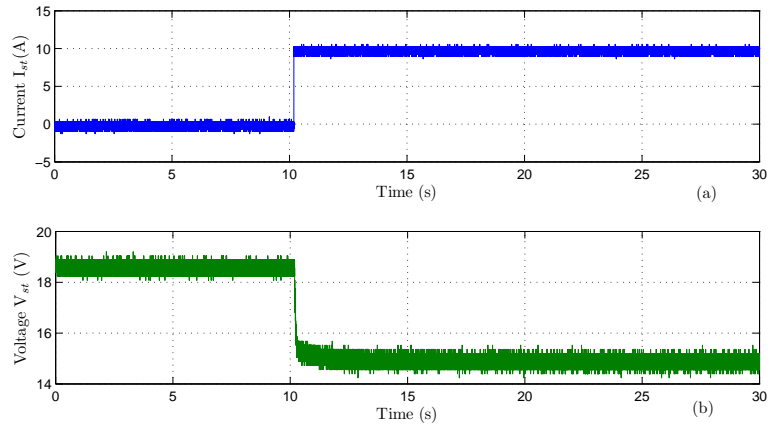


Figure 3.26: Experimental output current and voltage of the FC stack. (a) Output current (I_{st}). (b) Voltage in the terminals of the FC (V_{st}).

By applying Matlab fast fourier transformation (FFT) to I_{st} and V_{st} , the frequency swept is obtained (shown in Fig. 3.27(a)). As in the simulation, the dc value (frequency 0) is removed from the spectrum and low frequencies have higher

magnitudes. The analysis was done from 50 mHz up to 2.5 kHz, the representation in Fig. 3.27(a) is only up to 100 Hz for visualization. In Fig. 3.27(b) the graph of $\text{real}(Z_{st})$ vs $\text{imaginary}(Z_{st})$ is presented, the representation is not as clear as in the simulation, yet a parabolic tendency can be seen. As it is shown, lower frequencies values of Z_{st} are located in the right side of the plot and, close to the origin, are the high frequencies values of Z_{st} . Due to noise and perturbations introduced by the instruments, not all the spectrum corresponds to the FC stack natural oscillations, therefore a set of chosen frequencies are plotted.

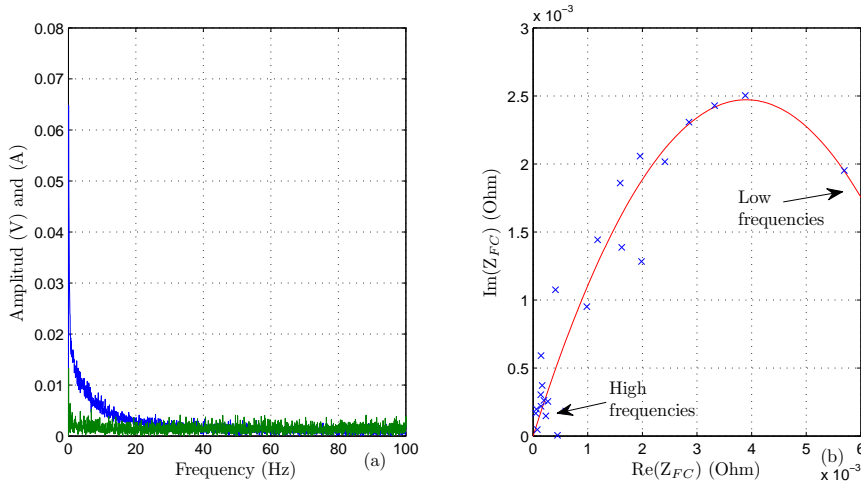


Figure 3.27: Experimental frequency analysis of the output voltage and current of the FC stack. (a) Frequency spectrum of current (green) and voltage (blue). (b) Real vs Imaginary plot of the internal impedance of the FC stack.

3.4.3 Experimentation of Close Loop Operation

In order to show the integrated system working, basic experimental tests of the close loop operation of the system is presented in this section.

Fig. 3.28 shows the response of the air flow controller due to a successive increment of the electric load and, after 9.8 s, the recovery of the flow from a decrease of the load. Fig. 3.28(a) depicts the air flow reference (W_a^*) and the air flow of the system (W_a) and in Fig. 3.28(b) the corresponding FC stack current (I_{st}) for this flow evolution is shown. The load power profile imposed by changing the electric load resistance (R_L), generates a current increment of 7 A (in the bigger step at 6.4 s). The stabilization time after a step change of 14% of the

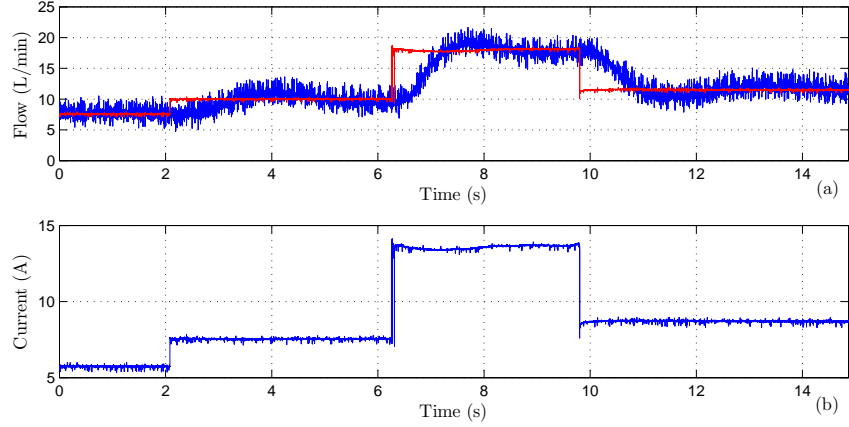


Figure 3.28: Close loop operation of the FC stack for rising and decreasing steps on the electric load. (a) Evolution of the air flow and air flow reference. (b) Load current evolution of the system.

maximum current of the FC stack is approximately 1 s.

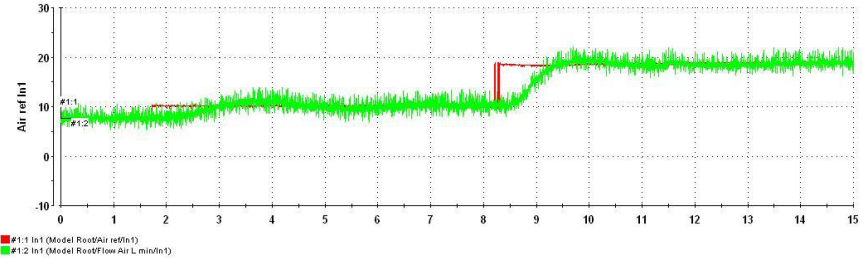


Figure 3.29: Close loop operation of the FC stack with rising steps on the electric load.

With the purpose of showing that W_a tracks its reference, a new experimental test is performed imposing a longer stabilization time for the system, the result of this experience is depicted in Fig. 3.29, where W_a^* is in red and W_a is in green. It can be seen that at 8.3 s a step of 9 NL/min is imposed over the flow (due to a change of the load), the controller follows the reference and stabilizes in, approximately, 1 s with a negligible overshoot. The experimental results exposed in the figure are presented as it is shown in the control panel screen (CPS).

3.5 Conclusions

The main objective of the chapter, and perhaps of the thesis, has been accomplished, i.e., the design and setup of a fuel cell stack evaluation test bench. The design and development of the test bench is divided into two main sections; process subsystems and the acquisition and data display. The third section is devoted to the presentation of some preliminary experimentation results which can give an idea of the potentiality of the test bench.

Using as a starting restriction the chosen FC stack characteristics, in section 3.2 the designing criteria and equipment technical information for the different subsystem is given (humidifiers, compressor, temperature regulation, air supply, and hydrogen supply). Since the objective is to test and evaluate, the amount of instruments used overpass those of a common practical application, furthermore in some cases instrument redundancy can be found. Yet, this dose not disable the system to run tests closer to real applications, which is, in fact, the next step of this long term project.

One of the most sensitive stages in the development is the one presented in section 3.3. The first main issue is the signal conditioning, from a industrial standard to the acquisition card characteristics. This restriction could have been avoided by using an industrial acquisition system, yet since the system requires high sampling speed, the chosen acquisition card is the appropriate technology. Consequently, custom PCB cards for signal conditioning were designed and setup. From the point of view of control, standard controllers where designed to be applied in the auxiliary subsystems, i.e., bubbler temperature regulation, FC stack temperature regulation, and bubbler water refill. To ensure a safe and friendly operation, the data display, together with the digital protection system, are implemented taking advantage of the flexibilities of acquisition card and its interface software.

Although, all the subsystems and signals of the test bench were tested individually during the installation, the final experimental test gives certainty of the appropriate operation of the integrate system. The characteristic curve obtained and its proximity to the manufacture's information, ensures the proper condition of the stack. By acquiring the internal impedance of the stack a new research branch is being explored, i.e., FC state of health monitoring. Finally, the close loop operation of the FC stack is the mayor achievement of the present work. In order to accomplish automatic tracking of electric load power the instrumentation, acquisition, auxiliary equipment, and subsystems must be working as a whole.

Chapter 4

Dynamic Energy Router

4.1 Introduction

In this chapter the efficient transfer of electric energy between subsystems is considered, where each subsystem can generate, store, or consume energy. An application example is a multi-domain system consisting of a fuel-cell-based generating unit, batteries, supercapacitors, and electric motors or generators; this topology is used in some electric cars. Depending on the operation regime, energy must be transferred between the various units, which we refer to as multiports, according to some energy-management policies. In order to ensure energy exchange, the interconnection of the storage and load devices is performed by using power converters. These subsystems are electronically switched circuits capable of adapting the port voltage or current magnitudes to a desired value.

To achieve energy transfer between multiports, it is common practice to assume that the system operates in steady state and then translates the power demand (flow sense and magnitude) of the multiports into current or voltage references. These references are then tracked with control loops, usually proportional plus integral (PI). Since the various multiports have different time responses, it is often necessary to discriminate between quickly and slowly changing power-demand profiles. For instance, due to physical constraints, it is not desirable to demand quickly changing power profiles to a fuel-cell unit. Hence, the peak demands of the load are usually supplied by a bank of supercapacitors, whose time response is fast. To achieve this objective, a steady-state viewpoint is again adopted, and the current or voltage references to the multiports are passed through lowpass or highpass filters. For further details, see 4.1.1.

The steady-state approach currently adopted in practice can only approxi-

mately achieve the desired objectives of energy transfer and slow–versus–fast discrimination of the power demand. In particular, during the transients or when fast dynamic response is required, the delivery of demanded power in response to current or voltage references and the time response action of the filters might be far from satisfactory.

In this chapter an energy router that dynamically controls energy flow is presented. The router operational principle presented in [4], [5] discriminates between “good” and “bad” energy within the context of walking robots. A brief review of this device, which we call the Duindam–Stramigioli energy router (DSER), is given below from the perspective of electrical networks. The DSER embodies a nonlinear transformation that instantaneously transfers energy among multiports. The flow direction and rate of change of the energy transfer are regulated by means of a single scalar parameter. The goal of this work is to show that the DSER can be implemented by using standard power electronic converter topologies. Moreover, it is shown in [12], [41] that nonlinear controllers can be used to determine the switching policy of the power converter. Therefore, the DSER can provide the basis for a physically viable device for high–performance energy–management applications. A DESR design of two–subsystem interconnection based on a external bus voltage regulation is tested by simulation and experimentation, and three different controllers (linear proportional plus integral (PI), feedback linearization (FL) without considering the system dynamic, FL considering the system dynamic) are evaluated to illustrate the performance of this approach. Finally, the same two–subsystem, yet without external bus voltage regulation, is tested by simulation and experimentation using FL controller (incorporating the system dynamic).

The chapter is organized as follows. In section 4.2, the energy–management problem is formulated, and a procedure used for its solution is reviewed. Section 4.3 is devoted to the description of the DSER, while in the following sections (4.4 and 4.5) simulation and experimental results under different conditions are presented. The chapter ends with some concluding remarks in section 4.6.

4.1.1 Criteria for Current Reference Selection

The definition of the reference current $i_j^*(t)$ described in section 4.4 can complement additional constraints aimed at satisfying, for example, instantaneous reactive power specifications in electrical power applications. In addition, and in order to discriminate between quickly and slowly changing power demands, the current reference might be filtered with lowpass, highpass, or bandpass filters before being

sent to the power converter controller.

Due to the slow dynamics of fuel cells, in combined implementation with other sources, the current reference of the fuel cell port comes from the load current passed by a lowpass filter. As shown in Fig. 4.1 the sum of the current references of ports 1 and 2 is the current reference of port 3. In this way, the fast response of the supercapacitor is used to supply high power demands. Furthermore, in this particular example, the voltage terminals of the three ports are considered to have the same value; otherwise the current reference shape is given by

$$i_1 \frac{v_1}{v_3} + i_2 \frac{v_2}{v_3} = i_3.$$

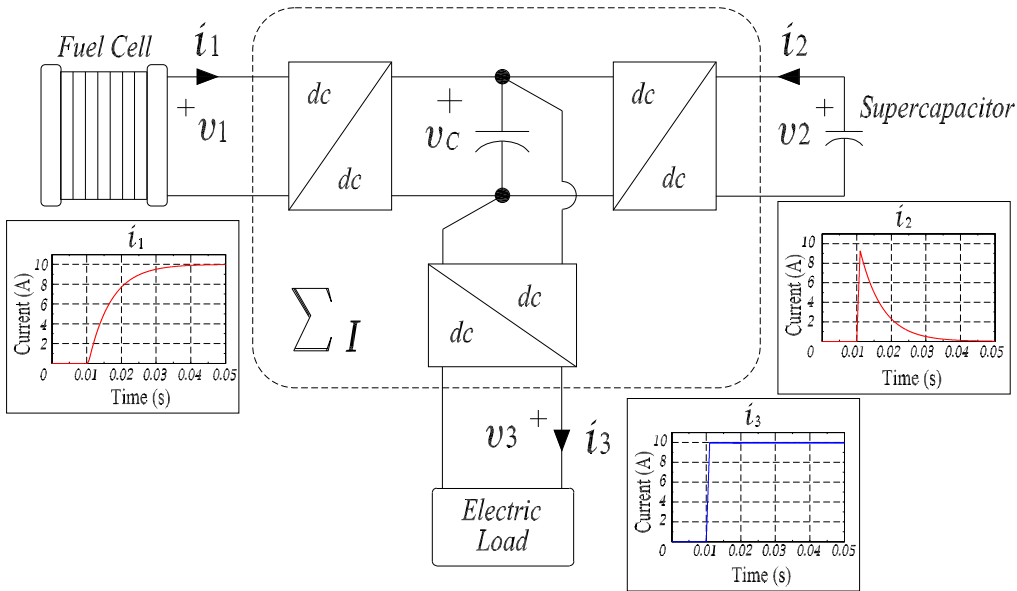


Figure 4.1: An example of current references in a multiport system with a fuel cell source unit, a supercapacitor as a storage unit, and a generic electric load. In this example, the current load experiences a fast increment.

4.2 Formulation of the Energy Transfer Problem

It is assumed that the multiports denoted by Σ have as port variables the terminal voltages and currents, which we denote as $v(t), i(t) \in \mathbb{R}^m$, respectively, see Fig. 4.2. It is also assumed that the multiports satisfy the energy-conservation law

$$\text{stored energy} = \text{supplied energy} - \text{dissipated energy}. \quad (4.1)$$

To formalize (4.1) the following assumptions are made.

- (i) The stored energy is represented by the nonnegative scalar function $\tilde{H} : \mathbb{R}^n \rightarrow [0, \infty)$, whose argument $x \in \mathbb{R}^n$ is the state vector of the multiport. In an electrical circuit, x consists of electric charges in the capacitors and magnetic fluxes in the inductors.
- (ii) The supplied energy is given by the integral of the power delivered by or demanded from the external environment, that is,

$$H_S(t) = \int_0^t v^\top(s) i(s) ds. \quad (4.2)$$

- (iii) For $t \geq 0$ the dissipated energy is given by the integral of a nonnegative function representing power. For instance, the rate of energy flow through the resistive element R is given by $Ri_R^2(t)$, where $R > 0$ is the value of the resistor and $i_R(t)$ is the current flowing through the resistor. Therefore the dissipated energy is

$$d(t) = \int_0^t Ri_R^2(s) ds. \quad (4.3)$$

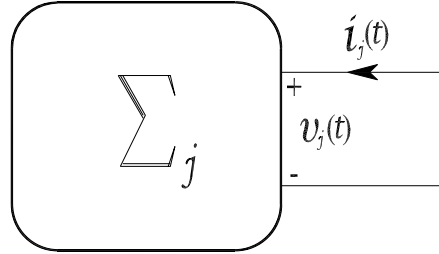


Figure 4.2: Representation of a subsystem, such as fuel cell or battery, as a multiport, denoted by Σ_j , with port variables $v_j(t)$ and $i_j(t)$. It is assumed that the multiport satisfies the energy-conservation law, which implies that the supplied energy is equal to the stored energy plus the dissipated energy. The studied system consists of q multiport systems Σ_j , with energy functions $H_j(t)$ and port variables $(v_j(t), i_j(t))$, $j = 1, \dots, q$, satisfying the power relation (4.6).

With this notation the energy–conservation law (4.1) becomes

$$H(t) - H(0) = \int_0^t v^\top(s) i(s) ds - d(t), \quad (4.4)$$

where $H(t) := \tilde{H}(x(t))$. Since $d(t) \geq 0$, we have

$$H(t) - H(0) \leq \int_0^t v^\top(s)i(s)ds. \quad (4.5)$$

The inequality (4.5) implies that, at each instant of time, the increase of stored energy cannot exceed the external supplied energy (4.2).

Differentiating (4.4) and noting that $\dot{d}(t) = Ri_R^2(t) \geq 0$ for all t , we obtain

$$\dot{H}(t) \leq v^\top(t)i(t), \quad (4.6)$$

which means that the rate of increment of stored energy is less than or equal to the power delivered by or demanded from the system. In order to accomplish the energy exchange, the system we consider is composed of q multiport subsystems Σ_j , with energy functions $H_j(t)$ and port variables $(v_j(t), i_j(t))$, $j = 1, \dots, q$, satisfying the power relation (4.6). These multiport subsystems are interconnected to exchange energy according to a specified energy–management policy.

The typical procedure for achieving energy transfer proceeds as follows [43]–[46]. Assume that at time $t \geq 0$ a demand $P_j^*(t)$ of power is requested from multiport Σ_j . Measuring the voltage $v_j(t)$, the power demand is then transformed into a current reference $i_j^*(t)$, solving the instantaneous power relation

$$P_j^*(t) = v_j^\top(t)i_j^*(t).$$

The terminal variables of the multiports are usually interconnected by power converters, which are circuits that apply the desired current or voltage profile to the multiport. In steady state, the desired energy-transfer objective is achieved asymptotically, thereby driving the current tracking error $i_j^*(t) - i_j(t)$ to zero. Toward this end, the switching policy of the converter is determined with a PI loop around the current error.

4.3 The Duindam–Stramigioli Energy Router

Dynamic energy transfer is a time–varying energy rate according to the operational energy needs of the system. The operation of the DSER is briefly reviewed in this section; for further details see [5].

For simplicity, we first consider temporarily the case of two multiports. Moreover, we are interested in energy–management applications where the dissipated energy is negligible, that is, $d_1(t), d_2(t) \approx 0$. Therefore, the power inequality (4.6) becomes

$$\dot{H}_1(t) = v_1^\top(t)i_1(t), \quad \dot{H}_2(t) = v_2^\top(t)i_2(t). \quad (4.7)$$

Assume that, at time $t \geq 0$, it is desired to instantaneously transfer energy from multiport Σ_1 to multiport Σ_2 without losses. Therefore, we require that

$$v_1^\top(t)i_1(t) + v_2^\top(t)i_2(t) = 0, \quad (4.8)$$

with

$$\dot{H}_1(t) > 0, \quad \dot{H}_2(t) < 0. \quad (4.9)$$

Equation (4.9) ensures that $H_1(t)$ decreases, while $H_2(t)$ increases, as desired.

To accomplish the energy transfer objective we couple the multiports through another multiport subsystem Σ_I , called the interconnection subsystem shown in Fig. 4.3. To satisfy the constraint (4.8), the device Σ_I must be lossless, that is, the total energy loss is zero; this condition is traditionally called *power-preserving*, which refers equivalently to the fact that the rate of energy loss is zero.

A lossless interconnection that satisfies (4.9) is the DSER, which is defined by

$$\begin{bmatrix} 0 & \alpha(t)v_1(t)v_2^\top(t) \\ -\alpha(t)v_2(t)v_1^\top(t) & 0 \end{bmatrix}, \quad (4.10)$$

therefore, the relation between the port variables is

$$\begin{bmatrix} i_1(t) \\ i_2(t) \end{bmatrix} = \begin{bmatrix} 0 & \alpha(t)v_1(t)v_2^\top(t) \\ -\alpha(t)v_2(t)v_1^\top(t) & 0 \end{bmatrix} \begin{bmatrix} v_1(t) \\ v_2(t) \end{bmatrix}, \quad (4.11)$$

where $\alpha(t) \in \mathbb{R}$ is a possibly time-varying designer-chosen parameter that, as shown below, controls the direction and rate of change of the energy flow.

Multiplying (4.11) on the left by the row vector $[v_1^\top(t) \ v_2^\top(t)]$ yields (4.8). Hence, Σ_I is lossless. Furthermore, substituting the current expressions of (4.11) into (4.7) yields

$$\dot{H}_1(t) = \alpha(t)|v_1(t)|^2|v_2(t)|^2, \quad \dot{H}_2(t) = -\alpha(t)|v_1(t)|^2|v_2(t)|^2, \quad (4.12)$$

which shows that if $\alpha(t) > 0$, then (4.9) is satisfied. Note that the DSER ensures only that $H_1(t)$ is nonincreasing and $H_2(t)$ is nondecreasing. However, when the voltages are different from zero, which is the normal operating condition, the desired energy exchange occurs.

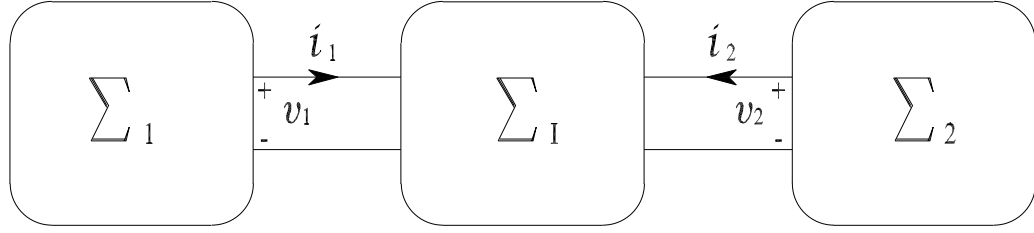


Figure 4.3: Interconnection subsystem, denoted by Σ_I . In order to couple multiports Σ_1 and Σ_2 satisfying the power preservation restriction, the interconnection subsystem must be lossless. The power-preserving interconnection Σ_I controls the energy-flow magnitude and direction.

The energy direction can also be inverted, that is, if $\alpha(t) < 0$, then the energy flows from Σ_2 to Σ_1 . Moreover, the energy transfer rate can also be regulated with a suitable selection of $\alpha(t)$. For instance, regulating the rate of change of $\alpha(t)$, the energy flow can be made faster or slower providing the ability to comply with restrictions on time responses of the multiports. These features of the DSER are illustrated in the sections 4.4 and 4.5.

The DSER defined by (4.11) is a current-tracking multiport. That is, given $v_1(t), v_2(t)$, (4.11) defines the desired values to be imposed on the multiport currents. A dual, voltage-tracking DSER can be defined as

$$\begin{bmatrix} v_1(t) \\ v_2(t) \end{bmatrix} = \begin{bmatrix} 0 & \alpha(t)i_1(t)i_2^\top(t) \\ -\alpha(t)i_2(t)i_1^\top(t) & 0 \end{bmatrix} \begin{bmatrix} i_1(t) \\ i_2(t) \end{bmatrix},$$

which yields

$$\dot{H}_1(t) = \alpha(t)|i_1(t)|^2|i_2(t)|^2, \quad \dot{H}_2(t) = -\alpha(t)|i_1(t)|^2|i_2(t)|^2.$$

The selection between current-tracking or voltage-tracking implementations of the DSER depends on technological considerations. In the current-tracking case $\alpha(t)$ controls the direction and rate of change of the energy flow. Therefore, $\alpha(t)$ must be selected by considering the energy-exchange needs and physical constraints on the system, for example, the maximum current or voltage tolerated by the system.

A more general form for the energy router is obtained by considering the generic interconnected system

$$\begin{bmatrix} i_1(t) \\ i_2(t) \end{bmatrix} = \begin{bmatrix} 0 & \beta(t) \\ -\beta(t) & 0 \end{bmatrix} \begin{bmatrix} v_1(t) \\ v_2(t) \end{bmatrix}, \quad (4.13)$$

where the matrix $\beta(t) \in \mathbb{R}^{m \times m}$ is chosen such that the power conditions (4.9) are satisfied. Multiplying both sides of (4.13) by $\begin{bmatrix} v_1(t)^\top & v_2(t)^\top \end{bmatrix}$ yields

$$\begin{bmatrix} v_1^\top(t)i_1(t) \\ v_2^\top(t)i_2(t) \end{bmatrix} = \begin{bmatrix} v_1^\top(t)\beta(t)v_2(t) \\ -v_2^\top(t)\beta(t)v_1(t) \end{bmatrix}.$$

In the DSER, $\beta(t) = \alpha(t)v_1(t)v_2^\top(t)$, while alternative choices of this parameter are suitable for achieving the desired energy transfer, for example, the introduction of a saturation function in $\beta(t)$ is a technique for limiting the energy exchange between multiports. Therefore, a useful choice for energy management is

$$\beta(t) = \alpha(t)\phi_1(v_1(t))(\phi_2(v_2(t)))^\top,$$

where $\phi_i : \mathbb{R}^m \rightarrow \mathbb{R}^m$ are first–third quadrant mappings, that is, ϕ_i satisfies $a^\top\phi_i(a) > 0$ for all $a \in \mathbb{R}^m$. By suitable selection of these functions, it is possible to modulate the contribution of each multiport to the overall power delivered.

In the development above it is assumed that the dissipated energy is negligible. More precisely, the dissipated energy in the resistors is assumed to be smaller than the energy transferred between the multiports, which is the case in many energy–management scenarios. The correct performance of the DSER cannot be ensured when this is not the case.

4.4 Design with external bus voltage regulation

In this section, a practical implementation to achieve the energy transfer defined by (4.11) is proposed. For simplicity, and without loss of generality, only scalar multiports are considered. Since the objective is evaluate the performance of the DSER under different operational conditions a power electronic scheme with external voltage regulation over the bus link is tested and different controllers are designed and tested over this topology. The fundamental characteristic of the power converter is its bidirectional energy exchange feature. The port variables, namely, voltages $(v_{S1}(t), v_{S2}(t))$ and currents $(i_{S1}(t), i_{S2}(t))$, are specified on both sides of the converter. The selection of the port characteristics imposes additional technological constraints on the circuit topology, which are briefly discussed in the conclusions.

The power electronics scheme shown in Fig. 4.4 is a two port energy router with external battery for bus-voltage regulation. Applying Kirchhoff's laws over the different switched states of the circuit, the final dynamics of the scheme are given by

$$L_{S1} \frac{di_{S1}}{dt}(t) = -R_{S1}i_{S1}(t) - v_{bus}(t)u_1(t) + v_{S1}(t), \quad (4.14)$$

$$L_{S2} \frac{di_{S2}}{dt}(t) = -R_{S2}i_{S2}(t) - v_{bus}(t)u_2(t) + v_{S2}(t), \quad (4.15)$$

$$L_{batt} \frac{di_{batt}}{dt}(t) = -R_{batt}i_{batt}(t) - v_{bus}(t)u_3(t) + v_{batt}(t), \quad (4.16)$$

$$C_{bus} \frac{dv_{bus}}{dt}(t) = u_1(t)i_{S1}(t) + u_2(t)i_{S2}(t) + u_3(t)i_{batt}(t), \quad (4.17)$$

where $i_{S1}(t)$, $i_{S2}(t)$, and $i_{batt}(t)$ are the inductor currents, $v_{bus}(t)$ is the voltage in the bus capacitor, $v_{batt}(t)$ is the voltage of the battery, and $u_1(t)$, $u_2(t)$, and $u_3(t) \in (0, 1)$ are the duty cycles of the switches, which represent the control signals. The specified resistance (R_{S1} , R_{S2} , and R_{batt}) are the series resistance of the inductors.

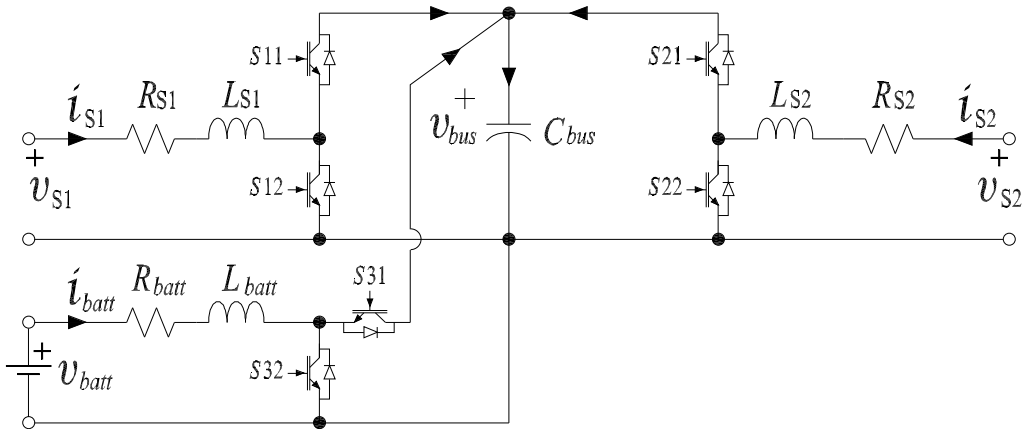


Figure 4.4: Power electronics implementation of the energy router with external energy supply to regulate the bus-voltage (v_{bus}).

The chosen subsystems connected to ports 1 and 2 are supercapacitors (C_{S1} and C_{S2}) which model contains a parallel resistor R_C . For model and simulation purpose, the capacitors and resistors are considered linear. The capacitance of supercapacitors, used normally as storage devices, is in the order of hundreds of F and the parallel resistance is in order of MΩ. Since the capacitance is related to the storage capability and voltage variation, only slight variations of the voltages $v_{S1}(t)$ and $v_{S2}(t)$ are expected. Capacitance on the order of hundreds or thousands of μF are normally used for voltage regulation. On the other hand, capacitances of the order of hundreds of F are used as storage elements.

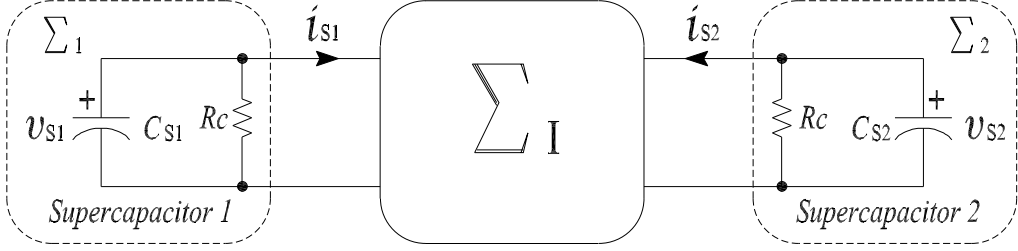


Figure 4.5: Interconnection of the subsystems, chosen as linear supercapacitors.

The multiports Σ_1 and Σ_2 (linear RC circuits) are shown in Fig. 4.5. The energy functions of the multiports are

$$H_1(t) = \frac{C_{S1}}{2}v_{S1}^2(t), \quad (4.18)$$

$$H_2(t) = \frac{C_{S2}}{2}v_{S2}^2(t). \quad (4.19)$$

Their dynamics are described by

$$C_{S1}\dot{v}_{S1}(t) = -i_{S1}(t) - \frac{1}{R_C}v_{S1}(t), \quad (4.20)$$

$$C_{S2}\dot{v}_{S2}(t) = -i_{S2}(t) - \frac{1}{R_C}v_{S2}(t). \quad (4.21)$$

Where C_{S1} and C_{S2} are the capacitance of the super capacitors and v_{S1} , v_{S2} , i_{S1} and i_{S2} are the voltages and currents of ports 1 and 2, respectively. An experimental test bench is implemented to evaluate the performance of the DSER, the experimental setup corresponds to the interconnection of two multiports of Fig. 4.5 using the power electronics implementation shown in Fig. 4.4. The experimental setup is shown in Fig. 4.6, in the upper part of this experimental desk, from left to right, we can see two supercapacitors (blue), two batteries (black), three inductors in the center, and the current and voltage sensors (two black boxes of the right). In the lower part of the desk, from left to right, the power converter and the switches drivers, with its corresponding source, are installed.

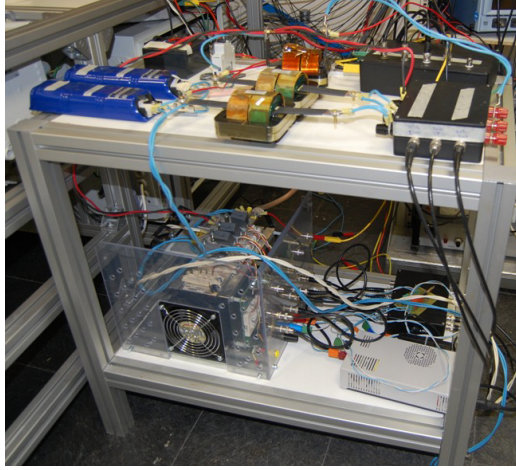


Figure 4.6: Photograph of the implemented test bench for the DSER.

The nominal value chosen for v_{bus} is 20V and the initial voltage condition of v_{S1} and v_{S2} is 10V. All the parameters of the experimental implementation and therefore, used for simulations purposes, are shown in Table 4.1.

Table 4.1: Parameters of the power electronics implementation.

Component	Value
L_{S1}, L_{S2} , and L_{batt}	$195 \mu\text{H}$
R_{S1}, R_{S2} , and R_{batt}	0.01Ω
C_{S1}, C_{S2}	52 F
C_{bus}	1.05 mF
R_C	$1 M\Omega$
V_{batt}	12 V
<i>Switching Frequencies</i>	20 kHz

Three different control strategies are developed and evaluated via simulation and experimentation. The problem of controller design for power converter systems of the form described by (4.14), (4.15), (4.16), and (4.17) is considered in the power electronics and control literature [12, 41, 8]. In this work, the main objective is to track the current references defined in (4.11), namely,

$$\begin{bmatrix} i_{S1}^*(t) \\ i_{S2}^*(t) \end{bmatrix} = \begin{bmatrix} \alpha(t)v_{S1}(t)v_{S2}^2(t) \\ -\alpha(t)v_{S2}(t)v_{S1}^2(t) \end{bmatrix}, \quad (4.22)$$

where i_{S2}^* and i_{S1}^* are the desired port currents and $\alpha(t)$ is the time varying signal shown in Fig. 4.7. The same general shape of $\alpha(t)$ is used in the different tests, yet in simulation of the switched system, due to time computational restrictions, the total time is, in the case of switched simulation, reduced to 1s. Moreover, in experimentation, signal shift is expected due to the triggered of $\alpha(t)$. The variable $\alpha(t)$ can be constant or time varying, as shown in the plot.

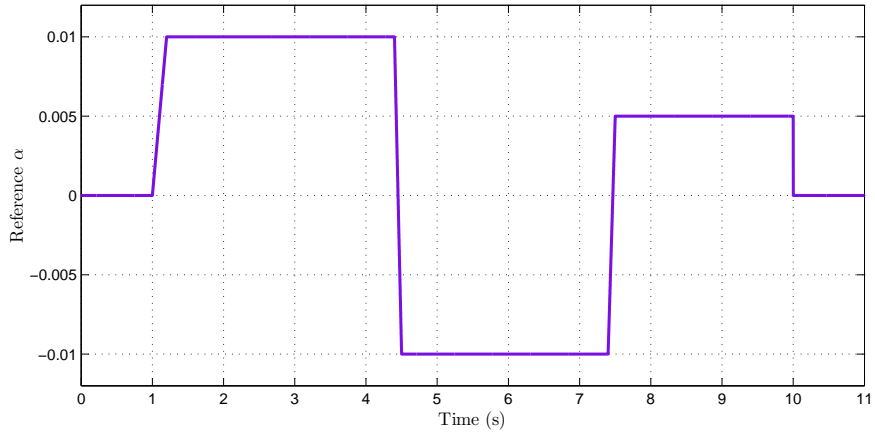


Figure 4.7: Time evolution of $\alpha(t)$, which controls the energy rate and direction.

As it is shown Fig. 4.7 the starting value of $\alpha(t)$ is zero, hence the energy exchange between C_{S1} and C_{S2} is null. At time 1 s $\alpha(t)$ start increasing at a constant rate and reach the value 0.01 at the time 1.2s. The variable $\alpha(t)$ remains in 0.01 during 3.2 seconds, period while the energy should be flowing from C_{S1} to C_{S2} . At time 4.4s, a decreasing ramp is imposed over $\alpha(t)$, i.e., abrupt inversion of sign of $\alpha(t)$ in the period 4.4 to 4.5 seconds. In order to recharge the supercapacitor C_{S1} with energy coming from C_{S2} , the value of $\alpha(t)$ is kept in -0.01 up to time 7.4s, in this instant, an other abrupt change of $\alpha(t)$ (from -0.01 to 0.005) is produced in a period of 0.1s. The signal $\alpha(t)$ remains in this value for 2.5s, where once again, the energy should be flowing from C_{S1} to C_{S2} , yet this time with half of the initial magnitude. In the final part of the profile of $\alpha(t)$, an instantaneous change of the signal is produced at time 10s, where the signal change in the minimum possible time from 0.005 to 0 and remains in this value until the end of the test.

4.4.1 Linear controller, proportional plus integral (PI)

The block diagram of the general control scheme is the one depicted in Fig. 4.8, the strategy works as follows:

- PI _{i_{S1}} drives to zero the error between the i_{S1} and i_{S1}^* , reference which comes from the first term in (4.22).
- PI _{i_{S2}} drives to zero the error between the i_{S2} and i_{S2}^* , in the same way as before, the reference comes from the second term in (4.22).
- PI _{i_{batt}} drives to zero the error between the i_{batt} and i_{batt}^* . The reference of the battery current comes from the output of the bus voltage controller (PI _{v_{bus}}), where the chosen bus-voltage reference is $v_{bus}^* = 20V$.

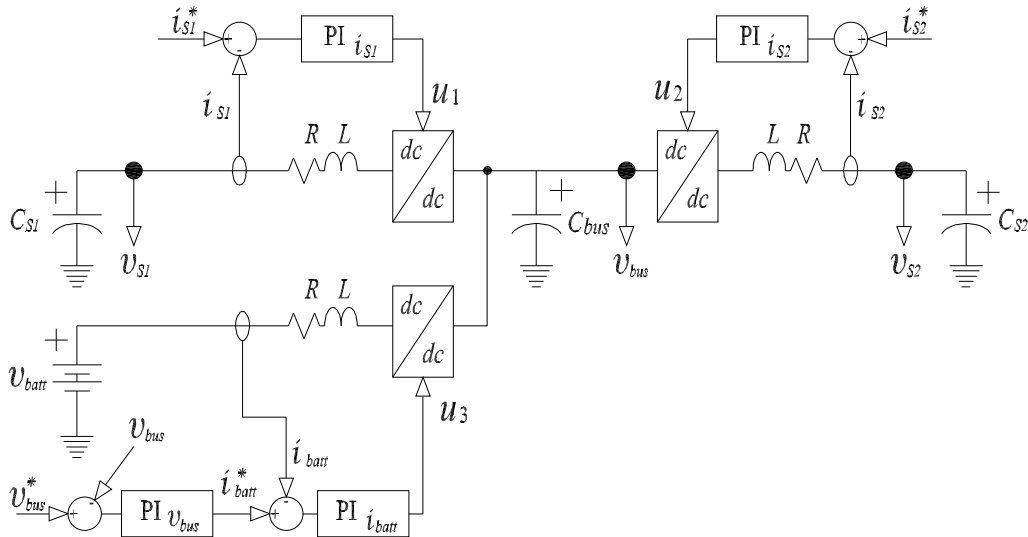


Figure 4.8: Control scheme of the DSER using linear PI controllers to follow the current references.

The controllers design is accomplished by using liner control techniques [9], [47], therefore the first step is to obtain the linearized system around the operation point, later, and by a small signal analysis simplification, the dynamic of each

state variable it's obtained. The linearize model of the system is the following,

$$\begin{bmatrix} \Delta \dot{i}_{S1} \\ \Delta \dot{i}_{S2} \\ \Delta \dot{i}_{batt} \\ \Delta \dot{v}_{S1} \\ \Delta \dot{v}_{S2} \\ \Delta \dot{v}_{bus} \end{bmatrix} = [A] \begin{bmatrix} \Delta i_{S1} \\ \Delta i_{S2} \\ \Delta i_{batt} \\ \Delta v_{S1} \\ \Delta v_{S2} \\ \Delta v_{bus} \end{bmatrix} + \begin{bmatrix} \frac{-v_{bus0}}{L_{S1}} & 0 & 0 \\ 0 & \frac{-v_{bus0}}{L_{S2}} & 0 \\ 0 & 0 & \frac{-v_{bus0}}{L_{batt}} \\ 0 & 0 & 0 \\ 0 & 0 & 0 \\ \frac{i_{S10}}{C_{bus}} & \frac{i_{S20}}{C_{bus}} & \frac{i_{batt0}}{C_{bus}} \end{bmatrix} \begin{bmatrix} \Delta u_1 \\ \Delta u_2 \\ \Delta u_3 \end{bmatrix} + \begin{bmatrix} 0 \\ \frac{\Delta P_{batt}}{L_{batt}} \\ 0 \\ 0 \\ 0 \\ 0 \end{bmatrix}, \quad (4.23)$$

with

$$[A] = \begin{bmatrix} \frac{-R_{S1}}{L_{S1}} & 0 & 0 & \frac{1}{L_{S1}} & 0 & \frac{-u_{10}}{L_{S1}} \\ 0 & \frac{-R_{S2}}{L_{S2}} & 0 & 0 & \frac{1}{L_{S2}} & \frac{-u_{20}}{L_{S2}} \\ 0 & 0 & \frac{-R_{batt}}{L_{batt}} & 0 & 0 & \frac{-u_{30}}{L_{batt}} \\ \frac{-1}{C_{S1}} & 0 & 0 & \frac{-1}{R_C C_{S1}} & 0 & 0 \\ 0 & \frac{-1}{C_{S2}} & 0 & 0 & \frac{-1}{R_C C_{S2}} & 0 \\ \frac{u_{10}}{C_{bus}} & \frac{u_{20}}{C_{bus}} & \frac{u_{30}}{C_{bus}} & 0 & 0 & 0 \end{bmatrix}, \quad (4.24)$$

where u_{10} , u_{20} , u_{30} , v_{bus0} , i_{S10} , i_{S20} and i_{batt0} , are the states values in the operation point and Δx represents the deviation of the variable x from its operation point x_0 .

Current Controller Design

From the linearized system (4.23) and (4.24), neglecting the parallel resistance of the supercapacitors (R_C) due to its high value, and considering that the capacitance is big enough to kept the voltages constant during operation of the system, it is assumed that the dynamics of the currents are governed by a first-order type of system. Therefore, the current equations are,

$$\Delta i_{S1} = \frac{\Delta u_1 - v_{bus0}}{sL_{S1} + R_{S1}}, \quad (4.25)$$

$$\Delta i_{S2} = \frac{\Delta u_2 - v_{bus0}}{sL_{S2} + R_{S2}}, \quad (4.26)$$

$$\Delta i_{batt} = \frac{\Delta u_3 - v_{bus0}}{sL_{batt} + R_{batt}}. \quad (4.27)$$

Hence, PI controllers of the form $k_j(sT_j + 1)/sT_j$ can provide an appropriate performance in close-loop, thus the resulting close-loop dynamics are

$$\frac{\Delta i_{S1}}{\Delta i_{S1}^*} = \frac{k_{is1}v_{bus0}}{T_{is1}L_{S1}} \frac{sT_{is1} + 1}{s^2 + s(\frac{R_{S1} + k_{is1}v_{bus0}}{L_{S1}}) + \frac{k_{is1}v_{bus0}}{T_{is1}L_{S1}}}, \quad (4.28)$$

$$\frac{\Delta i_{S2}}{\Delta i_{S2}^*} = \frac{k_{is2}v_{bus0}}{T_{is2}L_{S2}} \frac{sT_{is2} + 1}{s^2 + s(\frac{R_{S2} + k_{is2}v_{bus0}}{L_{S2}}) + \frac{k_{is2}v_{bus0}}{T_{is2}L_{S2}}}, \quad (4.29)$$

$$\frac{\Delta i_{batt}}{\Delta i_{batt}^*} = \frac{k_{ibatt}v_{bus0}}{T_{ibatt}L_{batt}} \frac{sT_{ibatt} + 1}{s^2 + s(\frac{R_{batt} + k_{ibatt}v_{bus0}}{L_{batt}}) + \frac{k_{ibatt}v_{bus0}}{T_{ibatt}L_{batt}}}. \quad (4.30)$$

$$(4.31)$$

As it can be seen from (4.28), (4.29), and (4.30), the dynamics in close-loop of the currents can be approximated by a second order system, in which case the damping ratio is identified as

$$\begin{aligned} \xi_{i_{S1}} &= \frac{R_{S1} + k_{is1}v_{bus0}}{L_{S1} \cdot 2 \cdot \omega_{i_{S1}}}, \\ \xi_{i_{S2}} &= \frac{R_{S2} + k_{is2}v_{bus0}}{L_{S2} \cdot 2 \cdot \omega_{i_{S2}}}, \\ \xi_{i_{batt}} &= \frac{R_{batt} + k_{ibatt}v_{bus0}}{L_{batt} \cdot 2 \cdot \omega_{i_{batt}}}. \end{aligned} \quad (4.32)$$

Moreover, we can identify the oscillation frequency of the current close loop controller as

$$\omega_{i_{S1}} = \sqrt{\frac{k_{is1}v_{bus0}}{T_{is1}L_{S1}}}, \quad \omega_{i_{S2}} = \sqrt{\frac{k_{is2}v_{bus0}}{T_{is2}L_{S2}}}, \quad \text{and} \quad \omega_{i_{batt}} = \sqrt{\frac{k_{ibatt}v_{bus0}}{T_{ibatt}L_{batt}}}. \quad (4.33)$$

Choosing the settling time for the currents of the system (T_{Sis1} , T_{Sis2} , and T_{Sibatt}) and a proper damping ratio (ξ_{is1} , ξ_{is2} , and ξ_{ibatt}) in order to limit the overshoot, from (4.32) and (4.33) we calculate the constants of the PI controllers T_{is1} , T_{is2} , T_{ibatt} , k_{is1} , k_{is2} , and k_{ibatt} (see Table 4.2 for details). Since the system is composed by pulse wide modulated (PWM) dc converters with switching frequency equal to 20000 Hz (carrier frequency f_Δ) and the control signals must respond slower than this frequency in order to ensure the correct operation, the settling time chosen is 10 times $1/f_\Delta$ ($T_{Sis1} = T_{Sis2} = T_{Sibatt} = 10/f_\Delta$). To guaranty a fast dynamic response with 10% maximum overshoot, the value of the damping ratio must be in the range $0.6 < \xi_i < 1$, in this work the chosen value is $\xi_{is1} = \xi_{is2} = \xi_{ibatt} = 0.707$. In Fig. 4.9 is presented the frequency response of the current controllers.

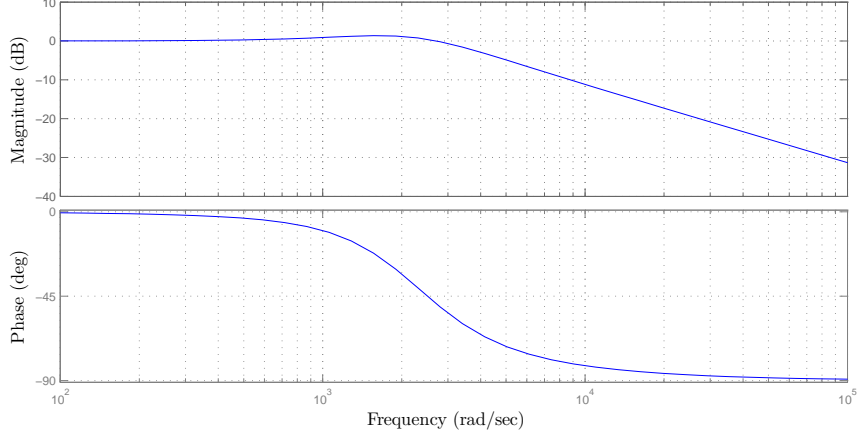


Figure 4.9: Bode diagram of the currents close-loop transfer function.

Voltage Controller Design

Since the battery is in charge of controlling the voltage of the dc-bus (v_{bus}) a proportional plus integral (PI) controller is designed to drive the v_{bus} error to zero, the output of this controller is the battery current reference (i_{batt}^*). To uncouple the voltage controller from the current controller and to avoid internal resonance, the time response is set to 10 times slower than the current controller, so the settling time of the voltage controller is $T_{Sv_{bus}} = 100/f_\Delta$. With this time separation it can be assumed that $\Delta i_{batt} = \Delta i_{batt}^*$ and that $\Delta u_1, \Delta u_2$ and Δu_3 are approximately 0. Therefore, from the linearized system (4.23) and (4.24) we obtained the dynamic of the voltage v_{bus} in terms of the current i_{batt}^* ,

$$\Delta v_{bus} = \frac{\Delta i_{batt}^*}{sC_{bus}} \frac{u_{30}}{sT_{v_{bus}}}. \quad (4.34)$$

The dynamics corresponds to a first-order system and so a linear controller of the form $k_{v_{bus}}(sT_{v_{bus}} + 1)/sT_{v_{bus}}$ can provide good performance in a close-loop. Thus the resulting close-loop dynamics is

$$\frac{\Delta v_{bus}}{\Delta v_{bus}^*} = \frac{k_{v_{bus}}u_{30}}{T_{v_{bus}}C_{bus}} \frac{sT_{v_{bus}} + 1}{-s^2 + s(\frac{k_{v_{bus}}u_{30}}{C_{bus}}) + \frac{k_{v_{bus}}u_{30}}{T_{v_{bus}}C_{bus}}}. \quad (4.35)$$

As can be seen in (4.35), the close-loop dynamics has the form of a second-order system therefore, we can identify the damping ratio ($\xi_{v_{bus}}$) and the oscillation

frequency ($\omega_{v_{bus}}$) of the close-loop as

$$\xi_{v_{bus}} = \frac{k_{v_{bus}} u_{30}}{C_{bus} 2 \omega_{v_{bus}}}, \quad (4.36)$$

$$\omega_{v_{bus}} = \sqrt{\frac{k_{v_{bus}} u_{30}}{T_{v_{bus}} C_{bus}}}. \quad (4.37)$$

Following the same design criteria of the current controllers, to establish a time separation between the two control loops, a settling time ($T_{Sv_{bus}}$) 10 times faster than the settling time of the current controller is chosen. Moreover, to ensure fast response and limit the overshoot to 10%, a value $\xi_{v_{bus}} = 0.707$ is chosen.

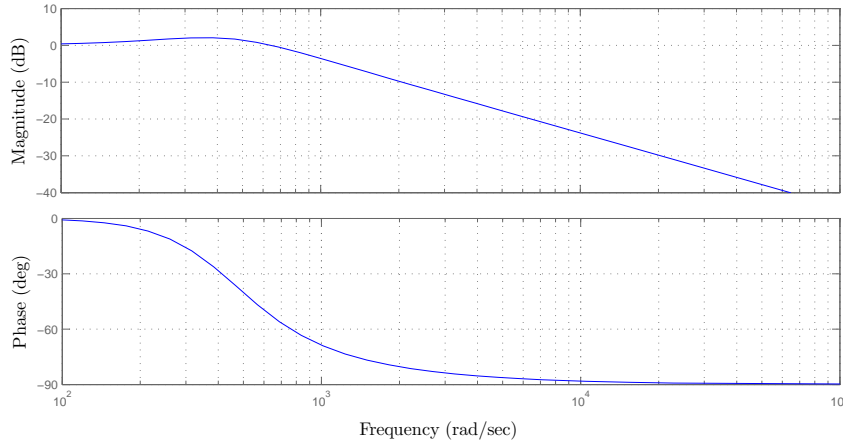


Figure 4.10: Bode diagram of the bus voltage close-loop transfer function.

In Fig. 4.10 is presented the frequency response of the system, as it can be seen the response of the v_{bus} controller is slower than the current controller. Moreover, for high frequencies the attenuation is 20dB per decade, performing as a first order system.

Simulation of the Average System

In this section some preliminary simulation results are given to evaluate the performance of the designed controllers and determine the initial conditions of the integrators before the experimentation. Due to computational restrictions, an average simulation of 10 second is run using Simulink, the implementation of a switched simulation of 20000 Hz is not viable using this software.

Table 4.2: PI controllers parameters

Controller	k_{pPI}	k_{iPI}
Current i_{S1}	-0.0265	-50.8203
Current i_{S2}	-0.0265	-50.8203
Current i_{batt}	-0.0265	-50.8203
Voltage v_{bus}	1.1084	357.9141

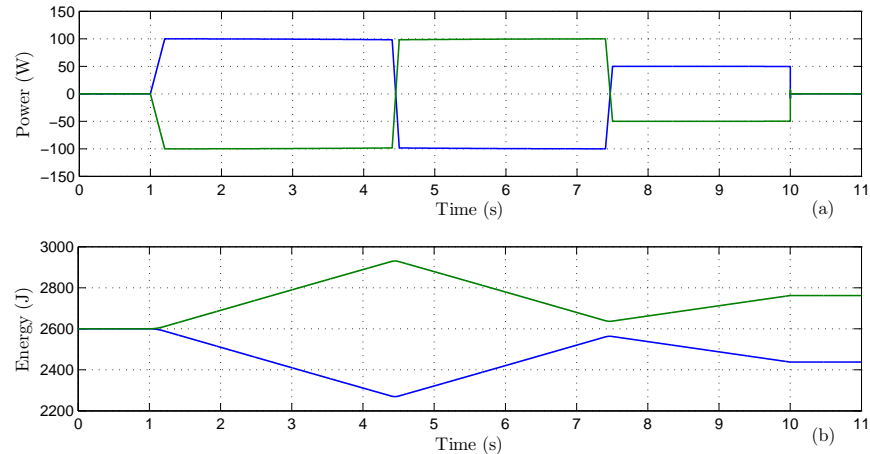


Figure 4.11: Simulation time evolution of the power and energy variation in ports 1 and 2. (a) Power $\dot{H}_1(t)$ and $\dot{H}_2(t)$ in blue and green, respectively. (b) Evolution of the energy stored in the supercapacitors C_{S1} ($H_1(t)$) and C_{S2} ($H_2(t)$) in colors blue and green, respectively.

Fig. 4.11 depicts the behavior of the instantaneous power and energy variation of Σ_1 and Σ_2 , that is, $\dot{H}_1(t)$, $H_1(t)$ and $\dot{H}_2(t)$, $H_2(t)$, respectively. It can be seen in Fig. 4.11(a) the power delivered by one supercapacitor is the negative of the energy delivered by the other supercapacitor, this is the precise effect described in section 4.3. Given that in (4.12) α is positive in port 1 (C_{S1}) the shape of $\dot{H}_1(t)$ is proportional and of the same sign moreover, $\alpha=0.01$ is equivalent to 100 W of power transferred. The energy stored in both supercapacitors (C_{S1} and C_{S2}) is depicted in Fig. 4.11(b), $H_1(t)$ is shown in blue and $H_2(t)$ is in green. Since positive power delivered implies the discharge of the supercapacitor, $H_1(t)$ decreases from 2600J to 2269J during the period (1, 4.45) and it recovered up to

2563J at 7.47s, at 10s it attain its final value of 2437J. The time evolution of H_2 is the opposite of H_1 , in the interval (1, 4.45) it changes from 2600J to 2931J, at 7.47s it reaches a local minimum of 2636J, finally it attain it 2438J at 10s.

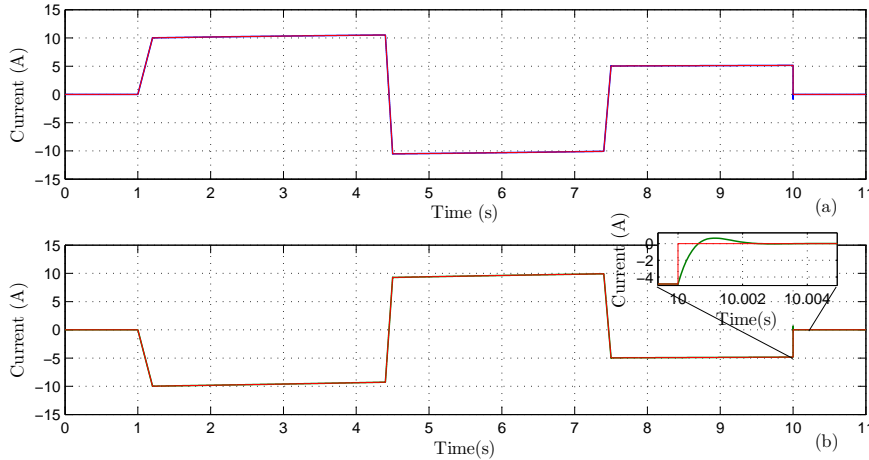


Figure 4.12: Simulation results for the evolution of i_{S1} , i_{S2} and their corresponding references. (a) Current i_{S1} in blue and its reference in red. (b) Current i_{S2} in green and its reference in red.

Fig. 4.12 depicts the currents in the terminals of the supercapacitors and their respective references. Current of C_{S1} (i_{S1}) and its reference (i_{S1}^*) are shown in Fig. 4.12(a), as it can be seen i_{S1} follows very accurately its reference. As it is expected, after the first ramp (from 1 to 1.2s) i_{S1} remains in 10A and experiments a slight variation due to the supercapacitors voltage changes. Fig. 4.12(b) shows the current evolution in capacitor C_{S2} (i_{S2}) and its corresponding reference (i_{S2}^*), as in the case of (i_{S1}), the current in C_{S2} follows closely its reference. In the magnified inset is shown the response of the current to a step change in the reference, it has to be considered that, since this is an average simulation, the results obtained for the overshoot and stabilization time are not necessary the once of the real system.

The evolution of the voltage of the bus capacitor (v_{bus}) is depicted in Fig. 4.13(a). As it is shown in the magnified inset, slights variations during the reference changes are produced and the action of the controller kept the voltage stable over its reference (20 V). In Fig. 4.13(b) the current i_{batt} is depicted. It can be seen, that during the periods where the power exchange is 100W ,(1.2,4.4) and (4.5,7.4), i_{batt} stabilized in 1.69A and where power exchange is 50W (7.5,10) it stabilized in 0.42A. Since the battery supply the energy to compensate the losses

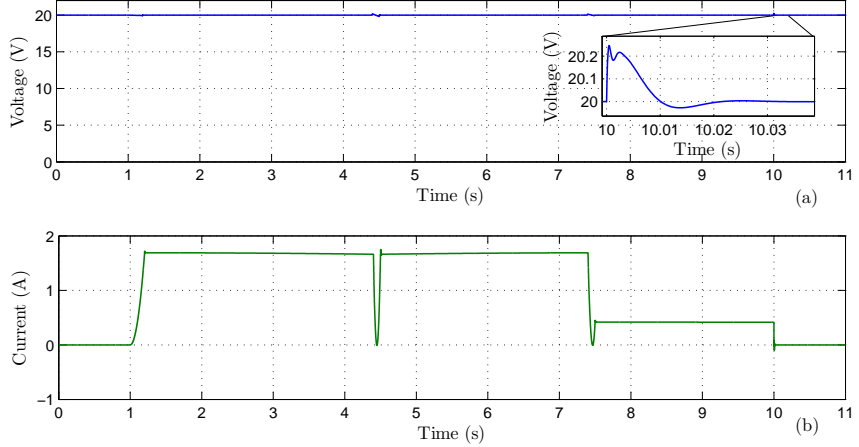


Figure 4.13: Simulation result of the time evolution of the bus-voltage capacitor v_{bus} and the current of the battery i_{batt} . (a) Voltage of the capacitor C_{bus} . (b) Current of the battery (i_{batt}).

of the system, it is possible to calculate the losses of system in terms of power by doing $i_{batt} \cdot v_{batt}$. Given that the losses are always positive, $i_{batt} \geq 0$.

Simulation of the Switched System

In order to ensure the appropriate experimental performance of the system a sampled switched simulation is accomplished. Although, the time scaling between the sampling time and the controllers is big enough to ensure a proper operation, a sampled simulation is a compulsory stage before running experiments. The sampled signal of $S_i(t)$ is defined as $S_i(kT)$, where T is the distance between the values k . Therefore, the sampled signal can be defined as

$$S_i(kT) = \sum_{i=0}^{\infty} \delta(kT - iT),$$

and the output as

$$y(kT) = \sum_{i=0}^{\infty} y(iT) \delta(kT - iT).$$

In this work the chosen sampling time is $50\mu\text{s}$, and the simulations that are shown in this section are done over a 20kHz switched using an integration time step of $0.5\mu\text{s}$. Due to computational limitation, simulation of maximum 1s are viable and in a time interval (4.35, 4.55) is presented.

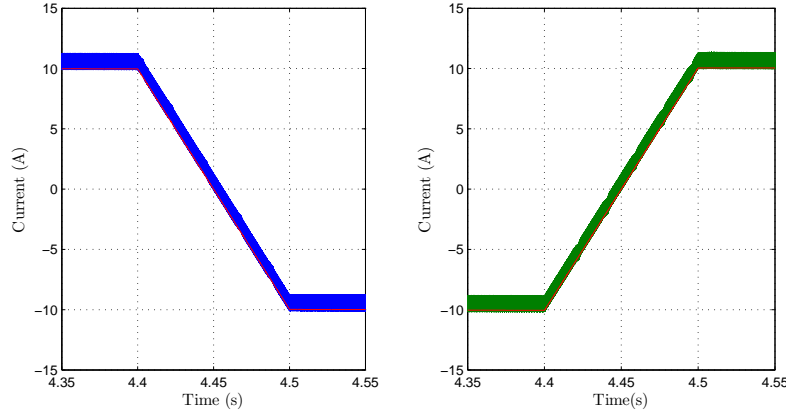


Figure 4.14: Sampled simulation results of i_{S1} , i_{S2} and their corresponding references. (a) Current i_{S1} in blue and its reference in red. (b) Current i_{S2} in green and its reference in red.

As shown in Fig. 4.14, the currents of the system follow accurately their references, and the overall performance is in agreement with what was expected. Unlike the average system, a current ripple of 1.5A is superimposed over the signal, this is a normal working condition of switched power converters. The ripple can be reduced by increasing the switching frequency or by changing the inductors L_{S1} and L_{S2} of the circuit.

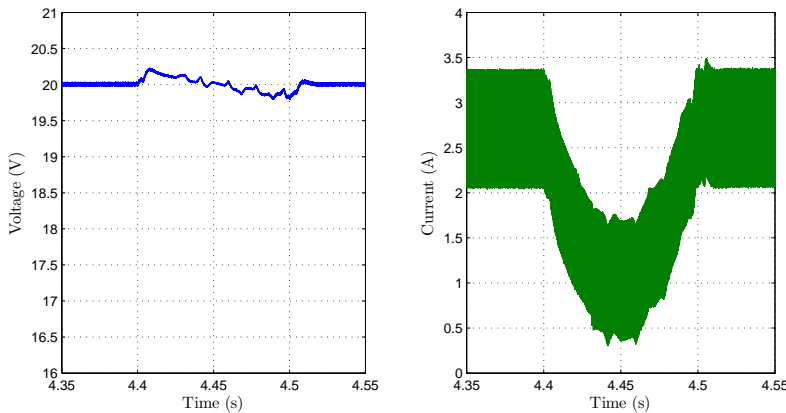


Figure 4.15: Sampled simulation result of v_{bus} and i_{batt} . (a) Voltage v_{bus} . (b) Battery current (i_{batt}).

The time evolution of the bus voltage and the battery current is depicted in

Fig. 4.15. As it is illustrated, also in the case of i_{batt} and v_{bus} controllers, the result is close to the average simulation. The time response of the system is not affected by the sampling time, and the ripple, due to the switching condition, dose not interfered in the correct operation of the power converter.

Experimental Results

Using the test bench shown in Fig. 4.6 experimental tests are carried out. The system is driven to its steady state condition ($i_{S1} = i_{S1}^*$, $i_{S2} = i_{S2}^*$, and $v_{bus} = 20V$) and, with the supercapacitors charged to 10 V, the experiment is performed. In Fig. 4.16(a) is shown the power exchange between supercapacitors C_{S1} and C_{S2} , it can be seen that as observed in simulation, the power delivered by C_{S1} has the same sign as α yet the amplitude is scaled. The first ramp occurs in the period (1.3, 1.5), at this time the power exchange stabilizes during 3.2 seconds in 120 W, for C_{S1} , and -120 W, for C_{S2} . In the period (4.7, 4.8) another referenced ramp is produced (more abrupt than the first one), due to this reference change the power of both supercapacitors is inverted and stabilizes around $\dot{H}_1 = -120$ W and $\dot{H}_2 = 120$ W. During the period (4.8, 7.7) C_{S1} and C_{S2} remain around -120 and 120 W, respectively, only a slight variation is produced. At time 7.69 s another inversion of sign occurs, a ramp of 0.1 s duration drives each power delivered to its half negative value (from 120 W to -60 W in the case of C_{S2} and from -120 W to 60 W in the case of C_{S1}). The difference of the power delivered between the simulation and the experimentation, 100 W and 120 W respectively, is due to the supercapacitors voltage deviation. In the simulation the initial voltage for both supercapacitors is 10 V, while for experimentation C_{S1} and C_{S2} are 9.9 V and 11.2 V, respectively.

In Fig. 4.16(b) are shown the stored energy variation of the C_{S1} and C_{S2} in blue and green, respectively. The initial value of the stored energy (2555 J for C_{S1} and 3271 J for C_{S2}) is different due to the deviation of the initial nominal voltage condition of each capacitor. As can be seen, the energy stored in each capacitor decreases when the power delivered in its terminals is positive. Therefore, in the case of C_{S1} the energy decreases during the periods, 1.3 to 4.74 s and 7.75 to 10 s, and increases during the period 4.74 to 7.75 s. In the case of the C_{S2} the evolution of the energy is the opposite as in C_{S1} .

In Fig. 4.17 are shown the currents i_{S1} and i_{S2} and their references i_{S1}^* and i_{S2}^* in red, as can be seen, both currents follow their references accurately. In order to simplify the experimentation, i_{S1} and i_{S2} are 0 when the experiment starts and

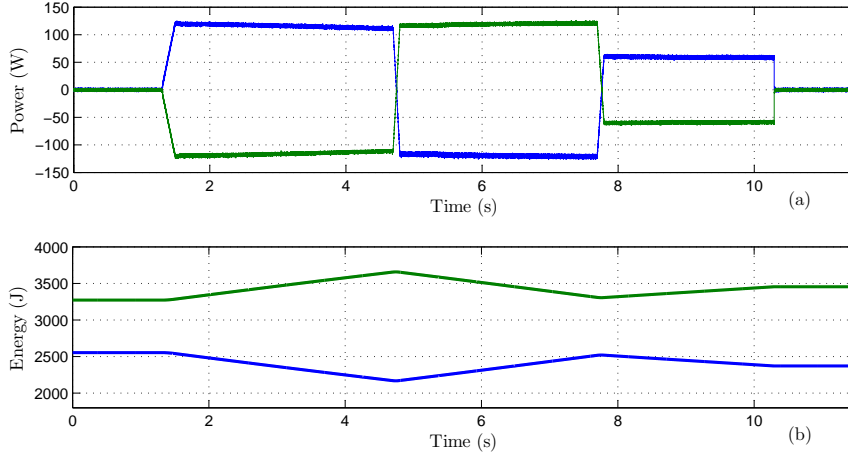


Figure 4.16: Experimental results for the time evolution of the power and energy variation in ports 1 and 2. (a) Power $\dot{H}_1(t)$ and $\dot{H}_2(t)$ in blue and red, respectively. (b) Energy evolution $H_1(t)$ and $H_2(t)$ in blue and green, respectively.

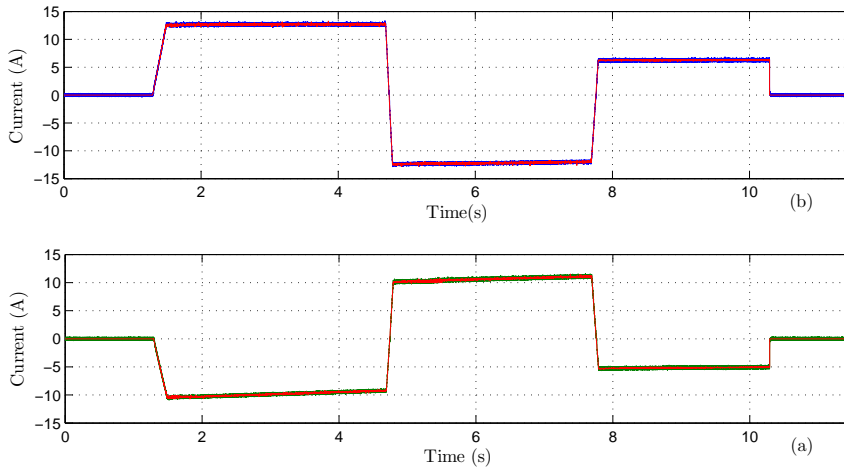


Figure 4.17: Experimental evolution of i_{S1} , i_{S2} and their corresponding references. (a) Current i_{S1} in blue and its reference in red. (b) Current i_{S2} in green and its reference in red.

when it ends.

As shown in Fig. 4.17(a), in the period (1.3, 1.5) the current varies from 0 to 12.6 A, during the interval (1.5, 4.69) i_{S1} remains almost stable around 12.7 A. An inversion of sign is produced (from 12.7 to -12.4 A) due to the abrupt ramp that

take place during (4.69, 4.79), where i_{S1} cross 0 A at 4.746 s. A slight change of the current magnitude (from -12.4 to -12.1) is produced in the period (4.79, 7.69). At time 7.69, i_{S1} changes in 0.1 s from -12.1 to 6.2 A, and during 2.5 s it remains close to 6.25 A. Finally, at 10.29 s an instantaneous reference change is imposed and i_{S1} goes from 6.25 to 0 A in approximately 0.001 s.

In Fig. 4.17(b) is depicted the time evolution of i_{S2} . After 1.3 s remaining in 0 A, a ramp occurs in the period (1.3, 1.5) where the current varies from 0 to -10.5 A. During the period (1.5, 4.7) the slight change of i_{S2} that drives it to -9.2 A. Between (4.69, 4.79) the current change abruptly from -9.2 to 10.1 A, where the cross of 0 is produced at 4.742 s. A small variation on the magnitude (from 10.1 to 11.1) take place during (4.79, 7.69). At time 7.69 i_{S2} changes in 0.1 s from 10.1 to -5.3 A and, during 2.5 seconds it remains around -5.15 A (from -5.3 to -5.05 A). Finally, at 10.29 s, an instantaneous reference change is imposed and the current changes from -5 to 0 A in approximately 0.001 s. The small variations that the currents have during the periods where α is constant and different from 0, is due to the variation over v_{S1} and v_{S2} produced by the energy exchange phenomenon.

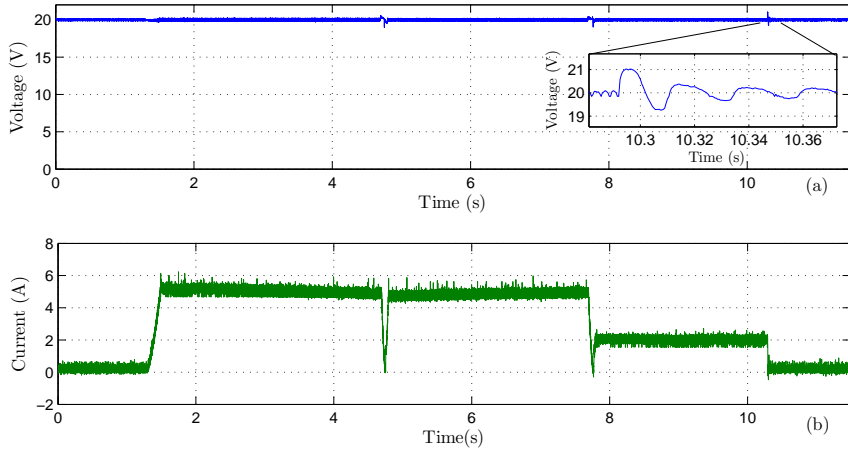


Figure 4.18: Experimental result of the time evolution of the bus-voltage capacitor (v_{bus}) and the battery current (i_{batt}). (a) Bus capacitor voltage (v_{bus}). (b) Battery current (i_{batt}).

In Fig. 4.18 are shown the bus voltage (v_{bus}) and the current supplied by the battery (i_{batt}), in (a) and (b), respectively. The v_{bus} depicted in Fig. 4.18(a) follows very accurately its reference (20 V) and only slight variations can be detected during the changes of α and therefore, changes on current and power delivered. A

magnified inset is included in order to visualize the action of the controller, moreover a variation of 1 V is shown in this inset, hence a 5% variation over the nominal voltage of the bus. The current i_{batt} , shown in Fig. 4.18(b), is compensating the losses of the system, consequence of the operation of the switches and the parasite resistance of the devices. Hence, this graph gives as relevant information in relation to the model of the system losses. At time 1.3 the current rises up to 5.2 A in 0.2 seconds, it remains around 5.2 A (with a small variation) during the period (1.5, 4.69). At time 4.74 i_{batt} touches 0 A, this happens at the same time that i_{S1} and i_{S2} are 0 A. i_{batt} raises again from 0 to 4.7 A in 0.05 s, and remains around 4.7 A during (4.79, 7.69). At the new inversion of the supercapacitor currents i_{batt} reaches 0 A (at 7.77 s) and recovers later up to 2 A (at 7.79 s). Between times (7.79, 10.29) i_{batt} remains around 2 A. Finally, at 10.29 s the battery current goes to 0.2 A and remains at this value until the end of the experiment. Given that the implementation is a switched system, although the average energy exchange is 0 switched current exists in both ports (whose average value is 0). Due to these currents, losses in the switches are produced and therefore, small i_{batt} to compensate it ($i_{batt}=0.2$ A when i_{S1} and i_{S2} are 0). A preliminary comparison between Fig. 4.18(b) and Fig. 4.13(b) gives the idea of the magnitude of the deviation while estimating the losses without considering the switching dissipation.

4.4.2 FL without considering the internal dynamics

In this section, to present the operational principles of the DSER, we consider the feedback linearization

$$u_1(t) = \frac{1}{v_{bus}(t)}[v_{S1}(t) - R_{S1}i_{S1}(t) - L_{S1}\frac{di_{S1}^*}{dt}(t) + L_{S1}\gamma\tilde{i}_{S1}(t)], \quad (4.38)$$

$$u_2(t) = \frac{1}{v_{bus}(t)}[v_{S2}(t) - R_{S2}i_{S2}(t) - L_{S2}\frac{di_{S2}^*}{dt}(t) + L_{S2}\gamma\tilde{i}_{S2}(t)], \quad (4.39)$$

where $\gamma > 0$ is a tuning parameter, and the tracking errors are defined by

$$\tilde{i}_{S1}(t) = i_{S1}(t) - i_{S1}^*(t), \quad \tilde{i}_{S2}(t) = i_{S2}(t) - i_{S2}^*(t).$$

Replacing (4.38) and (4.39) in the current equations (4.14) and (4.15), respectively, yields

$$\dot{\tilde{i}}_{S1}(t) = -\gamma\tilde{i}_{S1}(t), \quad \dot{\tilde{i}}_{S2}(t) = -\gamma\tilde{i}_{S2}(t), \quad (4.40)$$

which implies that the current-tracking errors converge to zero exponentially fast, at a rate determined by γ , achieving the desired objective.

The derivatives of the reference currents used in (4.38) and (4.39) can be obtained using approximate differentiators. Alternative schemes that avoid differentiation can be derived from the results in [12, 41]. The control signals of the DSER, generated from (4.38) and (4.39), are the duty cycles of a PWM scheme operating at 20 kHz. The controller gain is set to $\gamma = 1000$. The derivatives of the current references are obtained by passing the signals through approximate differentiation filters

$$F(s) = \frac{ks}{\tau s + 1},$$

where $k = 1$ and $\tau = 0.00003$. In order to keep the voltage v_{bus} constant in 20 V, the same controller used in the previous section (4.4.1) is implemented. Since this controller is based on the system knowledge, and the previous experimental results have proven that there exists a deviation between the real and the simulation model of the system, an adjustment is done over the inductors series resistors in order to approximate it to the real losses of the whole circuit. Hence, the new chosen value for R_{S1} and R_{S2} is 0.27Ω .

Simulation Results

The simulations shown in this section are carried out using Matlab Simulink, due to computational restrictions, an average simulation of 11 second is run, a switched simulation of 20000 Hz is not viable using this software. With this simulation results it is possible to evaluate, e.g., the performance of the approximate differentiation filter. Since these results are close to the results obtained in the previous simulations analysis, only a brief description of the figures are given.

Fig. 4.19 depicts the behavior of the instantaneous power and stored energy of Σ_1 and Σ_2 , that is, $\dot{H}_1(t)$, $H_1(t)$ and $\dot{H}_2(t)$, $H_2(t)$, respectively. Fig. 4.19(a) illustrates that the power profile is achieved as desired, controlled by $\alpha(t)$ in both the direction and rate of change. As the energy is being transferred from one capacitor to the other in the period of (1, 4.45), the energy stored in the capacitor C_2 is initially increasing, while the energy stored in the capacitor C_1 is decreasing. The opposite situation takes place in the period (4.45, 7.467). Both working conditions are shown in Fig. 4.19(b)

In Fig. 4.20 are shown the supercapacitors currents and their references. Fig. 4.20(a) depicts the profile of i_{S1} , it can be seen that there is a close relation between this current and $\alpha(t)$ in direction and rate of change. The slight variations away

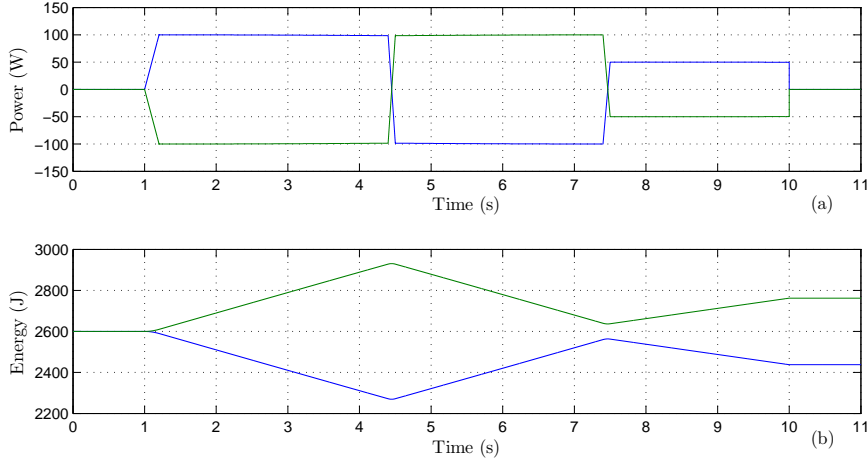


Figure 4.19: Simulation time evolution of the power and energy variation in ports 1 and 2. (a) Power $\dot{H}_1(t)$ and $\dot{H}_2(t)$ in blue and green, respectively. (b) Evolution of the energy stored in the supercapacitors C_{S1} ($H_1(t)$) and C_{S2} ($H_2(t)$) in blue and green, respectively.

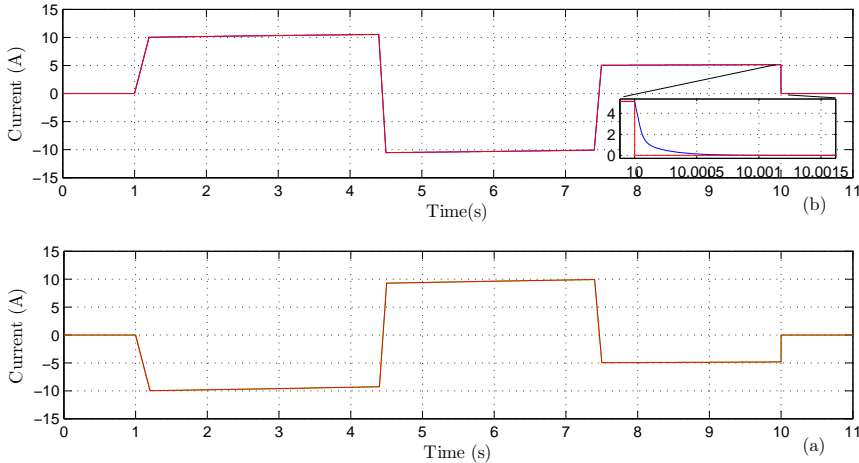


Figure 4.20: Time evolution of i_{S1} , i_{S2} and their corresponding references. (a) Current i_{S1} (blue) and its reference (red). (b) Current i_{S2} (green) and its reference (red).

from 10 A during (1.2, 4.4) is produced due to the supercapacitor voltage variation, the contrary situation takes place in the period (4.4, 7.4). In the case of i_{S2} shape, depicted in Fig. 4.20(b), it can be seen that it is almost equal to the negative

value of i_{S1} , yet the effect of the supercapacitor voltage variation has the opposite result in the current reference.

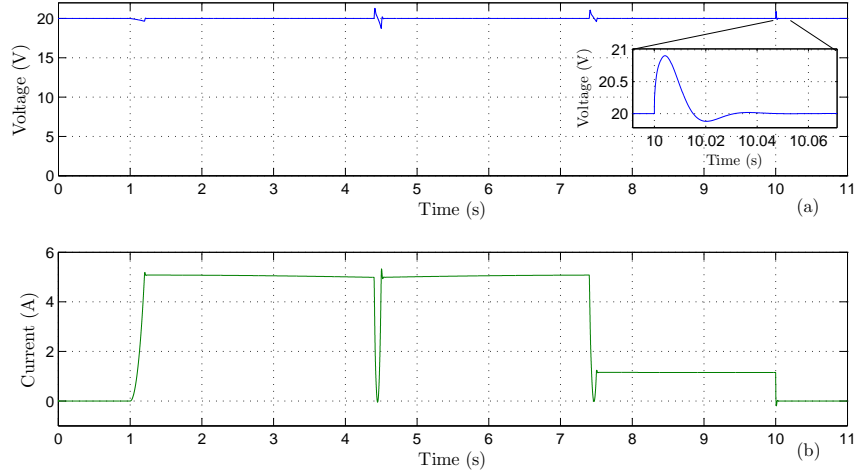


Figure 4.21: Simulation result of the time evolution of the bus-voltage capacitor (v_{bus}) and the current of the battery (i_{batt}). (a) Voltage of the capacitor C_{bus} . (b) Current of the battery (i_{batt}).

As in the previous simulation and experimental results, v_{bus} (depicted in Fig. 4.21) follows closely its reference (20 V) and only slight variations are produced during the changes of the α , i.e., in the periods (1, 1.2), (4.4, 4.5), (7.4, 7.5), and at 10 s. The controller effect is illustrated by a magnified inlet. The current supply by the battery is shown in Fig. 4.21)(b), in agreement with the changes of the circuit model, i_{batt} is closer to the experimental result shown in Fig. 4.18(b). Therefore, in the period (1.2, 4.4) and (4.5, 7.4) the value of i_{batt} is 5 A, yet during the period (7.5, 10), where the experimental behavior give us 2 A, the simulation results is 1.15 A. A priori it is evident that the model of the circuit does not perfectly match the real system.

Experimental Results

Experiments are performed using the test bench shown in Fig. 4.6 to evaluate the behavior of the controller. Due to trigger of the experiment in the dSPACE environment, α is shifted in relation to Fig. 4.7, yet the demanded magnitudes of power and energy are the same, therefore the results are comparable with the other experiments. As is illustrated in Fig. 4.22(a) the power exchanged between

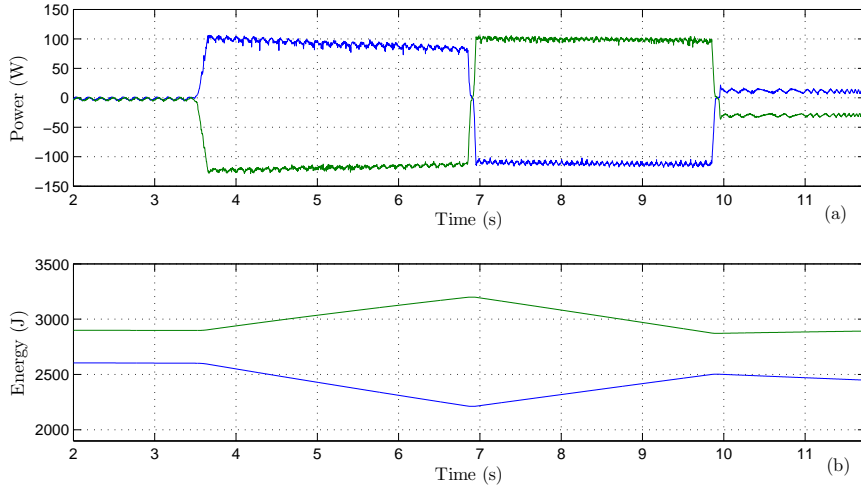


Figure 4.22: Experimental results for the time evolution of the power and energy in ports 1 and 2. (a) Power $\dot{H}_1(t)$ and $\dot{H}_2(t)$ in blue and red, respectively. (b) Energy evolution $H_1(t)$ and $H_2(t)$ in blue and green, respectively.

the supercapacitors follows the same pattern of α and of the simulation results, yet there is a clear degradation of the signal (superimposed noise of 22 W peak to peak (pp)) compared to the result depicted in Fig. 4.18. In the same way as the power exchange, the energy (shown in Fig. 4.22(b)) also has a general behavior as expected from the simulations and previous results. Although the tendency is appropriate, the variation of energy (ΔE) in the period (3.5, 6.9) is -400 J for C_{S1} and 300 J for C_{S2} . In consequence, the difference of energy is being compensated by the battery and the general behavior of the DSER is not appropriate.

There is clear mismatch between the i_{S1} and i_{S2} , and their references, i_{S1}^* and i_{S2}^* (shown in Fig. 4.23). In the period (3.65, 3.85) there is a difference between i_{S1} and i_{S1}^* of 1.25 A and between i_{S2} and i_{S2}^* of 1.5 A. Maximum (in this last case is varying). The fact that at the end of the experimentation, i.e. period (9.5, 11.75), the current mismatch increases (2.5 A for i_{S1} and 4 A for i_{S2}) means that the deviation of the signals from their references is caused by the inaccurate model of the system (respect to the dissipation) used for the controller design.

In agreement with what is expected, the voltage of the bus capacitor follows the corresponding reference (20 V), its shape is presented in Fig. 4.24(a). As can be seen, and comparing with previous results (figures 4.18 and 4.21), v_{bus} presents a clear degradation (from the point of view of noise and/or ripple). In the first

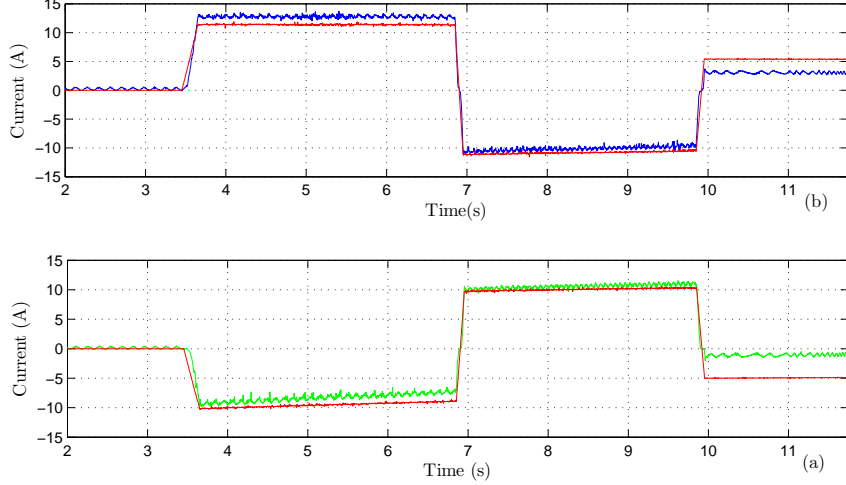


Figure 4.23: Experimental result of the evolution of i_{S1} , i_{S2} and their corresponding references. (a) Current i_{S1} (blue) and its reference (red). (b) Current i_{S2} (green) and its reference (red).

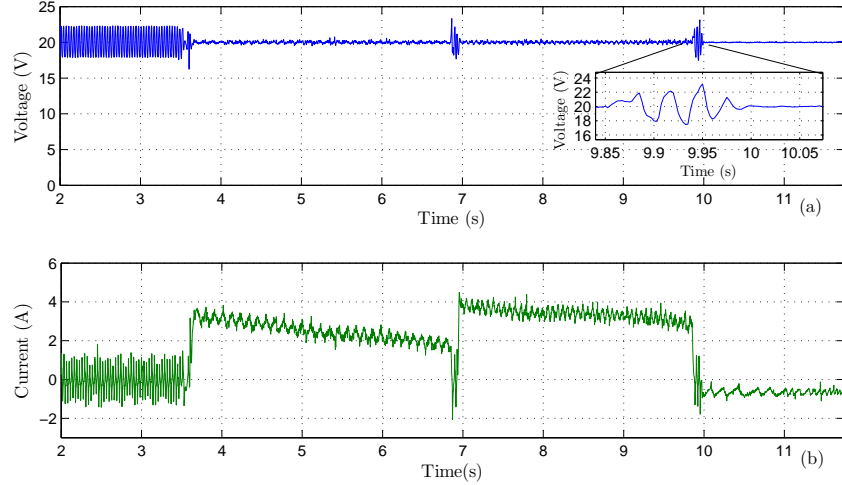


Figure 4.24: Experimental result of the time evolution of the bus-voltage capacitor v_{bus} and the battery current (i_{batt}). (a) Bus capacitor voltage (v_{bus}). (b) Battery current (i_{batt}).

period (2, 3.5), where the energy exchange is 0, the superimposed current ripple (ΔI_{Ripple}) is 4.2 A and during the ramps of α , the variation is up 5 V_{pp} . Given

that, there is a clear difference between Fig. 4.24(b) and Fig. 4.18(b), it is possible that; the losses are less, that one of the multi ports is supplying the dissipated energy, or the combination of both. Since i_{batt} is negative in the last period of Fig. 4.24(b) (from 9.95 s to the end), it is deducted that losses are supplied by one of the supercapacitors.

4.4.3 FL considering the dynamics of the system

A feedback linearization, considering all the dynamics of the system is developed and tested in this section. Considering the following outputs of the system

$$h_1(t) = i_{S1}(t) - \alpha v_{S1}(t)v_{S2}^2(t), \quad (4.41)$$

$$h_2(t) = i_{S2}(t) + \alpha v_{S1}^2(t)v_{S2}(t), \quad (4.42)$$

and their corresponding derivatives as

$$\dot{h}_1(t) = \frac{di_{S1}}{dt}(t) - \alpha v_{S2}^2 \frac{dv_{S1}}{dt}(t) - 2\alpha v_{S1}v_{S2} \frac{dv_{S2}}{dt}(t), \quad (4.43)$$

$$\dot{h}_2(t) = \frac{di_{S2}}{dt}(t) + \alpha v_{S1}^2 \frac{dv_{S2}}{dt}(t) + 2\alpha v_{S1}v_{S2} \frac{dv_{S1}}{dt}(t). \quad (4.44)$$

Replacing (4.14), (4.15), (4.20), and (4.21) in equations (4.43) and (4.44), and solving the control variables, results in

$$u_1 = \left[\frac{-R_{S1}i_{S1}+v_{S1}}{L_{S1}} + \frac{\alpha v_{S2}^2}{C_{S1}} \left(i_{S1} + \frac{v_{S1}}{R_{C1}} \right) + \frac{2\alpha v_{S1}v_{S2}}{C_{S2}} \left(i_{S2} + \frac{v_{S2}}{R_{C2}} \right) - \hat{h}_1 \right] \frac{L_{S1}}{V_{bus}}, \quad (4.45)$$

$$u_2 = \left[\frac{-R_{S2}i_{S2}+v_{S2}}{L_{S2}} - \frac{\alpha v_{S1}^2}{C_{S2}} \left(i_{S2} + \frac{v_{S2}}{R_{C2}} \right) - \frac{2\alpha v_{S1}v_{S2}}{C_{S1}} \left(i_{S1} + \frac{v_{S1}}{R_{C1}} \right) - \hat{h}_2 \right] \frac{L_{S2}}{V_{bus}}. \quad (4.46)$$

Where, \hat{h}_1 and \hat{h}_2 are the outputs of the system passed through PI controllers (driven to 0), due to the fact that $if h_i = 0 \Rightarrow \dot{h}_i = 0$. Therefore, by means of a PI controller is possible to stabilize the system and track the current references given in (4.22). Finally, the used PI controller parameters are $k_{p_{PI}} = -15000$ and $k_{i_{PI}} = -30000$.

Simulation Results

Using Matlab Simulink some preliminary simulations are carried out, to test the operation of the close-loop system. As in the previous simulation, an average simulation with the adjusted parameters ($R_{S1}=R_{S2}= 0.27 \Omega$) is performed, and only a brief description of the results is given. According to the results shown in Fig. 4.25 the performance of the controller is satisfactory, the behavior of the

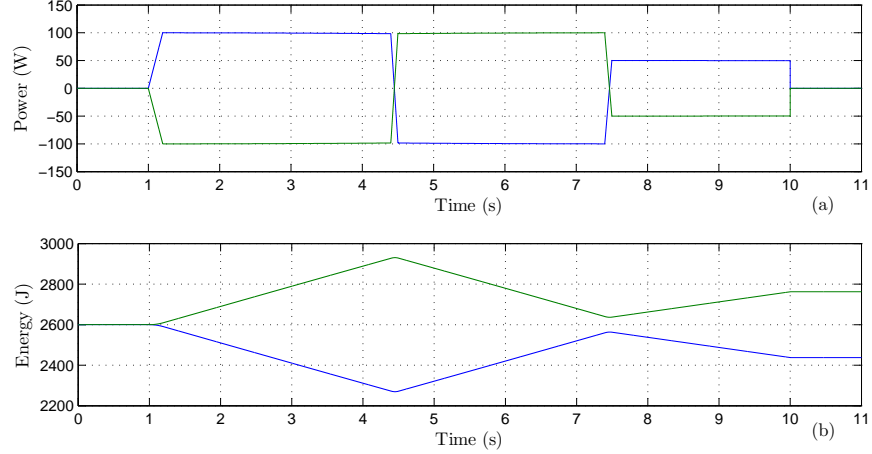


Figure 4.25: Simulation time evolution of the power and energy variation in ports 1 and 2. (a) Power $\dot{H}_1(t)$ and $\dot{H}_2(t)$ in blue and green, respectively. (b) Evolution of the energy stored in the supercapacitors C_{S1} ($H_1(t)$) and C_{S2} ($H_2(t)$) in blue and green, respectively.

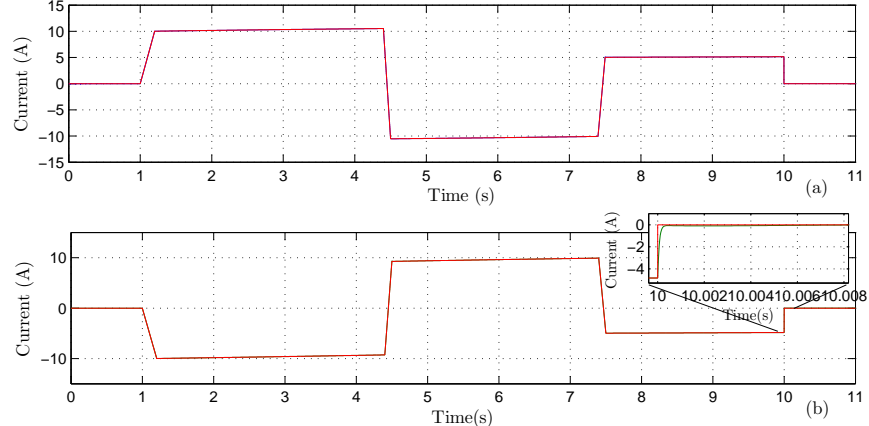


Figure 4.26: Time evolution of i_{S1} , i_{S2} and their corresponding references. (a) Current i_{S1} (blue) and its reference (red). (b) Current i_{S2} (green) and its reference (red).

instantaneous power and stored energy in the supercapacitors is in agreement with what is expected and close to the results obtained in the previous sections. In Fig. 4.26 are shown the supercapacitors currents and their references. Fig. 4.26(a)

depicts the profile of i_{S1} , it can be seen that there is a close relation between this current and $\alpha(t)$ in direction and rate of change. The slight variations away from 10 A during (1.2, 4.4) is produced due to the supercapacitor voltage variation, the contrary situation takes place in the period (4.4, 7.4). In the case of i_{S2} shape, depicted in Fig. 4.26(b), it can be seen that it is almost equal to the negative of i_{S1} , yet the effect of the supercapacitor voltage variation has the opposite result in the current reference. The stabilizing effect of the controller is illustrated in the magnified inlet of Fig. 4.26(b).

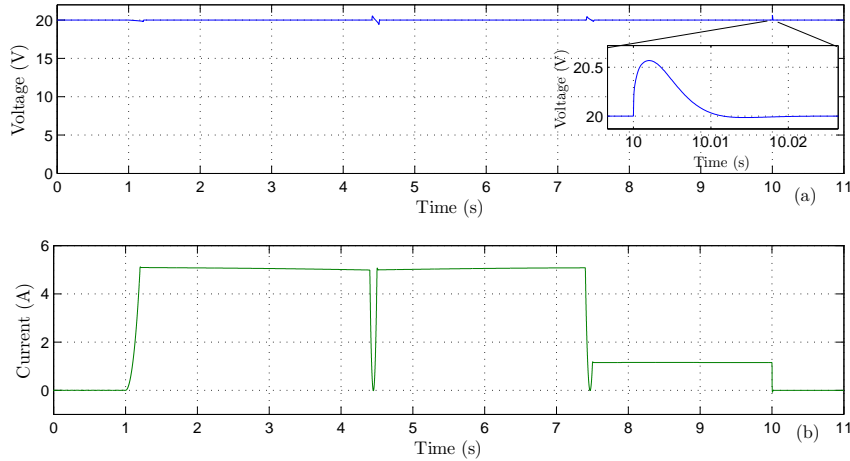


Figure 4.27: Simulation result of the time evolution of the bus-voltage capacitor (v_{bus}) and the current of the battery (i_{batt}). (a) Voltage of the capacitor C_{bus} . (b) Current of the battery (i_{batt}).

In agreement with what is expected, v_{bus} , shown in 4.27(a), follows its reference (20 V) accurately, and as in the previous simulations, only small perturbations are presented during the changes of α . The analog situation occurs in with i_{batt} , the simulation result shown in Fig. 4.27(b) is alike the simulation result depicted in Fig. 4.21. Based on the obtained results, is evident that the performance of the controller is appropriate to be tested in experimentation.

Experimental Results

By means of the test bench shown in Fig. 4.6, the new control strategy is tested. The conditions of the experimentation are almost the same as the ones explained in previous sections, i.e., the system is driven to its equilibrium condition ($i_{S1} = i_{S1}^*$,

$i_{S2} = i_{S2}^*$, and $v_{bus}=20$) and then the time varying $\alpha(t)$ (Fig. 4.7) is triggered.

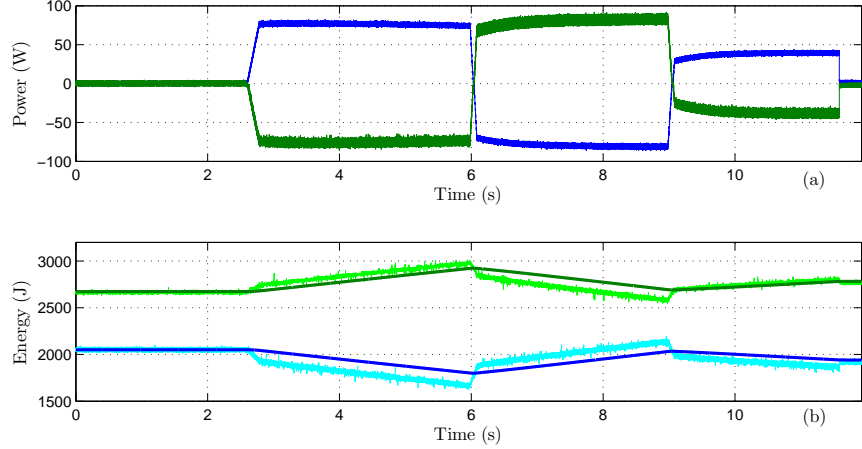


Figure 4.28: Experimental results for the time evolution of the power and energy in ports 1 and 2. (a) Power $\dot{H}_1(t)$ and $\dot{H}_2(t)$ in blue and red, respectively. (b) Energy evolution $H_1(t)$ and $H_2(t)$ in blue and green, respectively.

In Fig. 4.28(a) the power exchange between the two supercapacitors is depicted. As can be seen, the behavior of the system is analog to previous experimental results, $\dot{H}_1(t)$ and $\dot{H}_2(t)$ follow the same pattern (α) as in simulation and previous experiments. After the first ramp $\dot{H}_1(t)$ stabilizes around 76 W, later, and due to reference inversion, it reaches -80 W, and in the last period of power exchange, $\dot{H}_1(t)$ lays close to 38 W. The behavior of $\dot{H}_2(t)$ is analog with opposite sign, in the first period of power exchange it stabilizes close to -75 W, after the second ramp it crosses axis 0 and reaches 80 W, while in the last period (before going to 0) it lays around 38 W. As it is shown, the controller drives the system in order to follow the reference α in a satisfactory way. Although, a priori is clear that the response due to changes on the reference is not as fast as in the previous case (section 4.4.1).

Following the same behavior as in previous tests, the stored energy in the capacitors (shown in Fig. 4.28(b)) varies according to the magnitude of the power delivered. In the case of $H_1(t)$ (blue) it starts in 2050 J, then discharge up to 1800 J, recharged up to 2034 J, and finishes in 1941 J. As it is explained in previous section, the energy is calculated by integrating $\dot{H}_1(t)$, yet in Fig. 4.28(b) the energy calculated in the form $(C_i \cdot V_i^2)/2$ is also included, the difference between both graphs is due to the voltage drop in the series resistance of the supercapacitor

model [48, 49, 50]. The energy $H_2(t)$ (green) progresses as follows, due to the first energy exchange period, from 2675 J it reaches 2923 J, it later discharge up to 2691 J, and in the last period of the experiment it stabilizes in 2782 J.

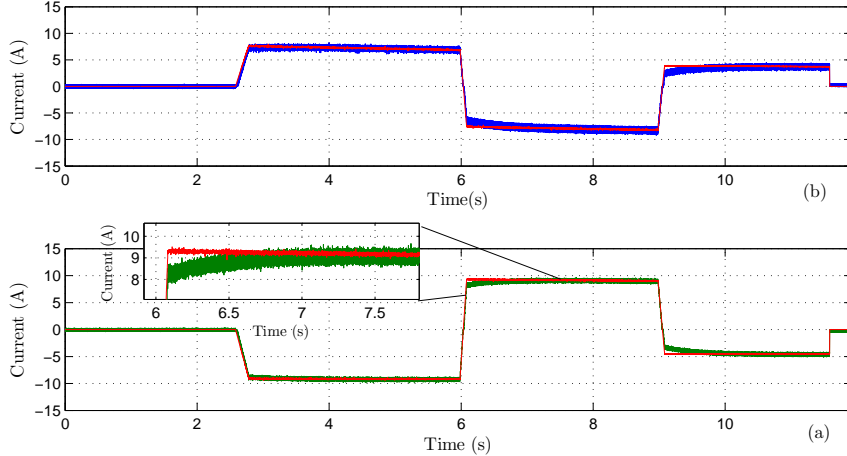


Figure 4.29: Experimental result of the evolution of i_{S1} , i_{S2} and their corresponding references. (a) Current i_{S1} (blue) and its reference (red). (b) Current i_{S2} (green) and its reference (red).

In Fig. 4.29 currents i_{S1} and i_{S2} , and the corresponding references, are depicted. Since the general evolution of the current is similar to previous experiments, only a brief description focused on the differences of the time response is given. As it is shown, a small error is produced after each imposed ramp. After the transient period (5.98, 6.08) the error of i_{S1} and i_{S2} is 1 A and after the variation produced during (8.88, 9.08) the error of i_{S1} is 1.5 A and of i_{S2} is 1.25 A. Moreover, as it is illustrated in the magnified inset, the currents track their references and they reach error equal to zero ($\tilde{i}_{S1,S2} = 0$) in approximately 1 s.

Fig. 4.30(a) depicts the time evolution of v_{bus} , the results obtained is very close to the result shown in section 4.4.1, the main difference is the increase of ripple during the periods of 0 energy exchange which might be caused by an internal controller resonance (between v_{bus} controller and i_{S1} , i_{S2} controllers). The time stabilization of currents i_{S1} and i_{S2} is transmitted to i_{batt} , this effect is shown in Fig. 4.30(b).

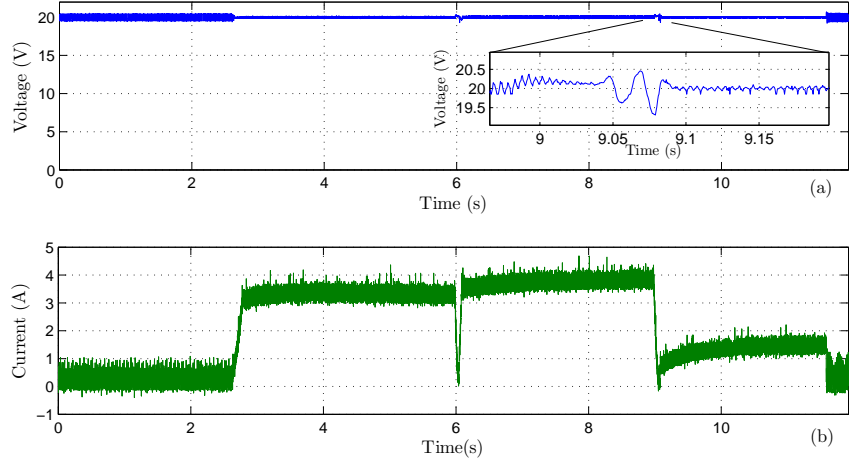


Figure 4.30: Experimental result of the time evolution of the bus-voltage capacitor (v_{bus}) and the battery current (i_{batt}). (a) Bus capacitor voltage (v_{bus}). (b) Battery current (i_{batt}).

4.5 Design with no external bus-voltage regulation

The switching circuit depicted in Fig. 4.31 is the used to implement the DSER. Assuming that the switching frequency of the power converter is sufficiently fast and applying Kirchhoff's laws to this converter, the dynamics of the DSER are described by

$$L_{S1} \frac{di_{S1}}{dt}(t) = -R_{S1}i_{S1}(t) - v_{bus}(t)u_1(t) + v_{S1}(t), \quad (4.47)$$

$$L_{S2} \frac{di_{S2}}{dt}(t) = -R_{S2}i_{S2}(t) - v_{bus}(t)u_2(t) + v_{S2}(t), \quad (4.48)$$

$$C_{bus} \frac{dv_{bus}}{dt}(t) = u_1(t)i_{S1}(t) + u_2(t)i_{S2}(t), \quad (4.49)$$

where $i_{S1}(t), i_{S2}(t)$ are the inductor currents, $v_{bus}(t)$ is the voltage in the bus capacitor, and $u_1(t), u_2(t) \in (0, 1)$ are the duty cycles of the switches, which represent the control signals. This scheme has the same general characteristics as the one presented in section 4.4, the main difference is the removal of the battery and its inductance (L_{batt}). For further details about implementation and modeling power converter devices, see [12, 8, 7].

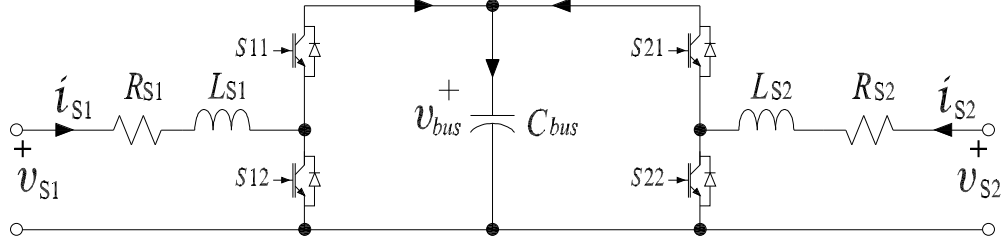


Figure 4.31: Power electronics configuration to implement the energy router without external energy supply.

4.5.1 Control Design

A feedback linearization, as the one implemented in section 4.4.3, is the chosen control strategy to accomplish the interconnection of two subsystems without external bus voltage energy supply. In this new scheme, in addition to drive to zero the outputs (4.41) and (4.42), the new defined output must be driven to zero, i.e.,

$$\tilde{v}_{bus} = v_{bus} - v_{bus}^*. \quad (4.50)$$

Therefore, the output (4.50) is passed through a PI controller of the form

$$\hat{h}_{v_{bus}} = kp_{v_{bus}}\tilde{v}_{bus} + ki_{v_{bus}} \int \tilde{v}_{bus}(s)ds, \quad (4.51)$$

where $\hat{h}_{v_{bus}}$ is annexed in the control signals (4.45) and (4.46) leading us to

$$u_1 = \left[\frac{-R_{S1}i_{S1}+v_{S1}+\alpha v_{S2}^2}{L_{S1}} \left(i_{S1} + \frac{v_{S1}}{R_{C1}} \right) + \frac{2\alpha v_{S1}v_{S2}}{C_{S2}} \left(i_{S2} + \frac{v_{S2}}{R_{C2}} \right) - \hat{h}_1 - \hat{h}_{v_{bus}} \right] \frac{L_{S1}}{v_{bus}}, \quad (4.52)$$

$$u_2 = \left[\frac{-R_{S2}i_{S2}+v_{S2}-\alpha v_{S1}^2}{L_{S2}} \left(i_{S2} + \frac{v_{S2}}{R_{C2}} \right) - \frac{2\alpha v_{S1}v_{S2}}{C_{S1}} \left(i_{S1} + \frac{v_{S1}}{R_{C1}} \right) - \hat{h}_2 - \hat{h}_{v_{bus}} \right] \frac{L_{S2}}{v_{bus}}. \quad (4.53)$$

This feedback linearization control is tested, initially, by means of simulation and later experimentally, the parameters of the scheme are the same used in section 4.4 and shown in Table 4.1, and the controller parameters are shown in Table 4.3.

Simulation Results

By means of Matlab Simulink, and using the controller parameters of Table 4.3 and the power parameters of the previous section, some average simulations are carried out before the experimental implementation.

As was expected from the analysis, the power profile, shown in Fig. 4.32(a), has change in relation to the results of section 4.4. The reference α is designed

Table 4.3: PI controllers parameters

Controller	k_{pPI}	k_{iPI}
Current i_{S1}	-15000	-30000
Current i_{S2}	-15000	-30000
Voltage v_{bus}	-10000	-15000

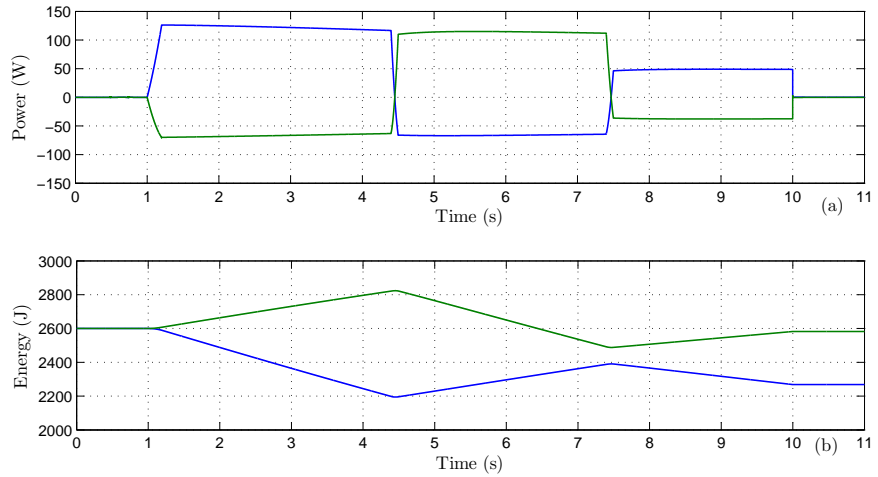


Figure 4.32: Simulation result of the time evolution of the instantaneous power and stored energy in ports 1 and 2. (a) Power $\dot{H}_1(t)$ and $\dot{H}_2(t)$ in blue and green, respectively. (b) Evolution of the energy stored in the supercapacitors C_{S1} ($H_1(t)$) and C_{S2} ($H_2(t)$) in blue and green, respectively.

in order to produced a power flow of 100 W in the first two cycles, and 50 W in the last period (Fig. 4.11). As shown in Fig. 4.32(a) $\dot{H}_1(t)$ starts in 126 W and finishes in 116 W in the period (1.2, 4.4). In the interval (4.5, 7.4), $\dot{H}_1(t)$ starts in -66 W, has a minimum of -67 W, and finishes in -64.5 W. In the last exchange period (7.5, 10), power $\dot{H}_1(t)$ starts in 46.4 W and finishes 48.8 W. Since noth ports contribute energy to compensate losses, $\dot{H}_2(t)$ is not the negative of $\dot{H}_1(t)$. Therefore, during the interval (1.2, 4.4) $\dot{H}_2(t)$ starts in -70 W and finishes in -63 W. In the second exchange period. (4.5, 7.4), $\dot{H}_2(t)$ starts in 110 W, has a maximum of 115 W, and finishes in 112 W. Finally, between the interval (7.5, 10), $\dot{H}_2(t)$ begin in -36.4 W and ends in 37.5 W.

The behavior of the supercapacitors stored energy (Fig. 4.32(b)) is in agreement with the obtained power profile. Although, different from the behavior depicted in Fig. 4.11 where both, energy in port 1 and 2, were symmetric respect to 2600 J. $H_1(t)$ decreases from 2600 J to 2194 J in the interval (1, 4.45), it recovered up to 2390.5 J at 7.47 s, and finally, $H_1(t)$ attains its definite value 2268 J at 10 s. With a different time evolution, in the period (1, 4.45) $H_2(t)$ increases from 2600 J to 2823 J, it attains its minimum 2488 J at 7.47 s, and it ends the experiment in 2582 J.

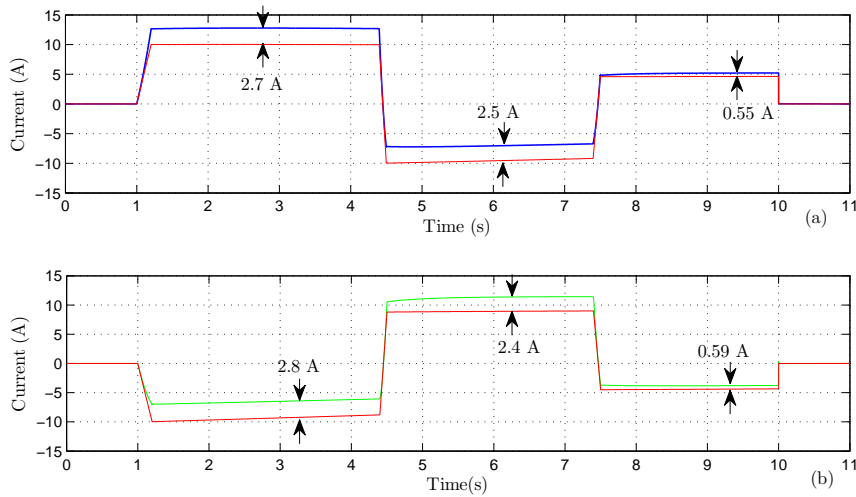


Figure 4.33: Time evolution of i_{S1} , i_{S2} and their corresponding references. (a) Current i_{S1} (blue) and its reference (red). (b) Current i_{S2} (green) and its reference (red).

In Fig. 4.33(a) the i_{S1} and i_{S1}^* are presented, as it is shown the current reference obtained by means of the DSER interconnection are no longer followed by the system. The current differences specified on the graph evidence that the separation strongly depends on the operation point. Regarding i_{S2} and i_{S2}^* (shown in Fig. 4.33(b)), the behavior is analogous, there is a mismatch between the current and its reference and the difference depends on the operation point, not only in magnitude but also the sign.

As was expected form the controller designed, a deterioration on v_{bus} profile occurs. A deviation of almost 6 V from its reference (20 V) is evidence in Fig. 4.34. Considering that this variation does not interfere with the appropriate behavior of the system and that the control of the bus voltage is a secondary objective of

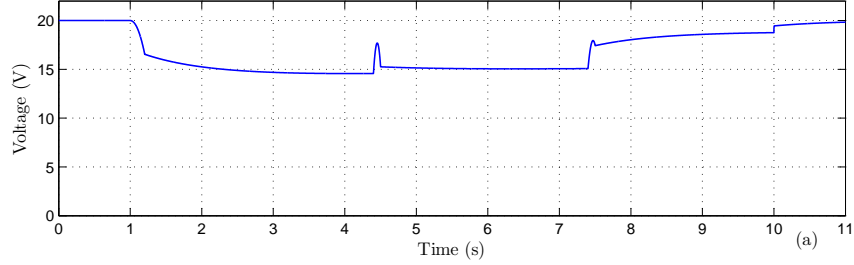


Figure 4.34: Simulation result of the time evolution of the bus voltage capacitor (v_{bus}).

the control strategy, further analysis should be done in order to take advantage of the Δv_{bus} and, in this way, get closer to the desired energy exchange profile.

Experimental Results

In order to test this new control strategy together with a dissipative DSER system, modifications are executed over the test bench shown in Fig. 4.6, mainly the battery electrical connection is taken.

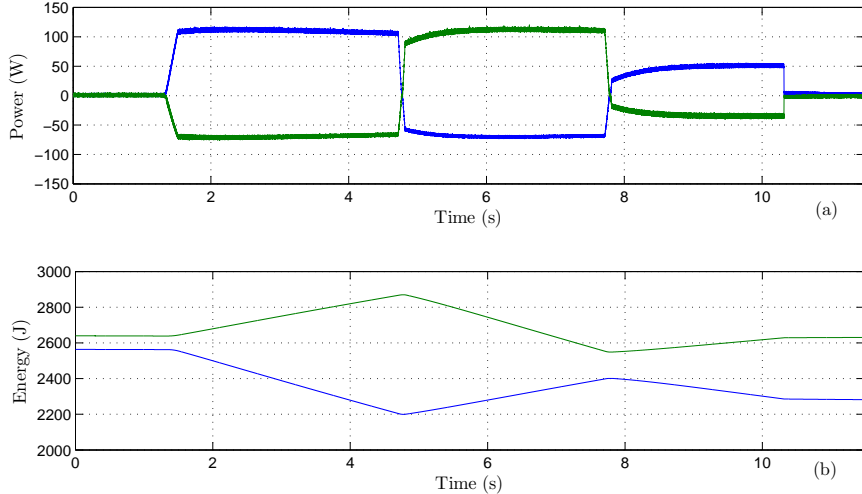


Figure 4.35: Experimental results for the time evolution of the power and stored energy in ports 1 and 2. (a) Power $\dot{H}_1(t)$ and $\dot{H}_2(t)$ in blue and red, respectively. (b) Stored energy $H_1(t)$ and $H_2(t)$ in blue and green, respectively.

The time evolution of power shown in Fig. 4.35(a) is in agreement with the simulation result. As shown, $\dot{H}_1(t)$ in the period (1.5, 4.72) moves between 106 and 112 W. After the sign inversion, in the interval (4.82, 7, 72), $\dot{H}_1(t)$ varies between -57.5 and -70 W and in the last energy exchange interval (7.82, 10.317) the magnitude of $\dot{H}_1(t)$ changes from 26 to 50 W. The behavior of $\dot{H}_2(t)$ also follows the pattern of its simulation, between the interval (1.5, 4.72) moves in the range of -69 to -66 W and during the sign inversion period (4.82, 7, 72) the power changes between 90 and 110 W. In the last interval of energy exchange (7.82, 10.317), $\dot{H}_2(t)$ varies between -18 and -35 W.

The stored energy in the capacitors, depicted in Fig. 4.35(b), has a time evolution in agreement with what was expected (close to simulation result). $H_1(t)$ changes from 2562 to 2200 J in the interval (1.34, 4.77), then it increase up to 2401 J at 7.79 s, and finally stabilizes in 2283 J after 10.32 s. With a different variation, yet following its simulation tendency, $H_1(t)$ increase from 2639 to 2870 J in the period (1.34, 4.77), it reaches its minimum value (2548 J) at 7.79 s, and stabilizes around 2630 J after 10.32 s.

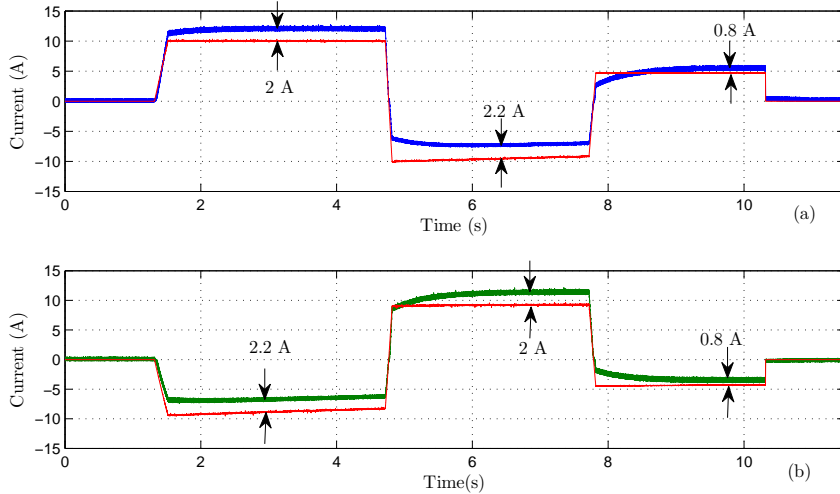


Figure 4.36: Experimental time evolution of i_{S1} , i_{S2} and i_{S1}^* , i_{S2}^* . (a) Current i_{S1} (blue) and its reference (red). (b) Current i_{S2} (green) and its reference (red).

i_{S1} and i_{S1}^* are depicted in Fig. 4.36(a), in accordance with the simulation results the current reference are no longer followed accurately by the system. The difference of current detected in steady state (2, 2.2, and 0.8A) evidence that the port is supplying energy in order to compensate the losses of the system. The

analog situation occurs with i_{S1} and i_{S1}^* (shown in Fig. 4.36(b)), a deviation from the current and its reference in steady state is imposed by the introduction of the v_{bus} controller. As shown in the graph, the deviations values are comparable between Fig. 4.36(a) and 4.36(b).

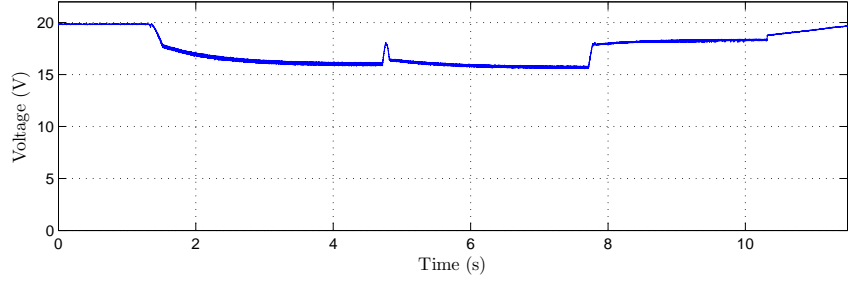


Figure 4.37: Time evolution of the bus voltage capacitor v_{bus} .

The behavior of v_{bus} profile is also close to its simulation, this result is depicted in Fig. 4.37. As it is shown there is a clear deviation between v_{bus} and v_{bus}^* (20 V), the signal reaches its minimum (15.7 V) at 7.7 s. The graph also evidence that the magnitude of the deviation depends on the operating point of the system, which is in agreement with the fact that also the losses depends on this.

4.6 Conclusions

A device to dynamically transfer energy between electrical multiports—the DSER—is presented and developed using standard switched power electronic devices. One of the central features of the DSER is the ability to control the direction and magnitude of the energy flow by changing only the parameter $\alpha(t)$, which comes directly from power port considerations. The importance of directly controlling the energy flow in microgrids is due to ability to monitor the stocks as well as the consumption of energy in the various storage and source devices of the system. In an application of energy transfer involving batteries, e.g., it is essential to be aware of the energy level of the batteries before making decisions about the appropriate energy control policy. The performance of a non-dissipative dual-port DSER for a dc-to-dc application was verified by simulations and experimentally. Moreover, a dissipative dual-port DSER was also tested by the same means. Three different controllers were evaluated in order to achieve the objectives and compare performance.

The performance of the DSER is in agreement with what was expected for a non dissipative interconnection, i.e., the current references, obtained from the lossless interconnection matrix and the variable $\alpha(t)$, determine the energy exchange and the instantaneous power in each port.

The designed PI controllers have a proper performance around the operation point, the references are tracked accurately, the time response is in agreement with the design criteria, and the error is zero in steady state. The chosen sampling time did not impact over the system performance. With this initial test it was possible to be aware of the limitations of the power electronics electrical model and, therefore, introduce important adjustments.

The feedback linearization without considering all the dynamics of the system performed appropriately in simulation (good time response and tracking). Although, and due to the mismatch in the electrical model, the result of the experimentation was poor, mainly regarding the steady state error. Due to this result it was possible to realize that the adjustments of the model were not accurate enough and more precise studies should be done considering the nonlinearities, and specifically, dependency of the dissipative units (series or parallel resistance) and the operating point. Also due to this implementation, it was possible to test (in simulation and experimentally) the approximate differentiation filter. The outcome is that the performance is appropriate and extensive use of this technique should be done, mostly for tracking controllers.

Regarding the feedback linearization that introduces all the dynamics of the system, an ideal performance is observed in simulation, yet in experimentation the performance was slightly degraded. As in the previous case, the dependency of the controller of the system parameters, impeded an ideal performance. Although, additional effort regarding the controller design should imply meaningful improvements.

Finally, the power scheme without external energy supply yielded satisfactory results. The implemented control strategy (feedback linearization) enables the system to keep the bus voltage around its reference by altering the energy exchange. Furthermore, the energy exchange magnitude is no longer defined only by alpha, i.e., an increment is inserted on the energy flow in order to compensate losses. Due to this modification, the currents do not track the initial references and the bus voltage no longer stabilized on its reference. Since the bus voltage control is a secondary objective of the control strategy, the fact that it was kept away from its reference does not impact the main goal of the DSER.

Chapter 5

DSER in Fuel Cell Applications

5.1 Introduction

Given that the result of Chapter 3 is an operative FC test bench and in Chapter 4 a new control strategy to dynamically control the energy exchange is the accomplished, the continuation of the research subject is the implementation of the DSER in FC applications. Therefore, in this chapter an example of multi source system containing a FC stack, a supercapacitor, and a variable load, is analyzed and tested by simulation. The purpose is to develop and evaluate the performance of the DSER applied on systems fed by FC stacks. The hybrid system, FC with a supercapacitor, is chosen due to the potential applications of this configuration [13, 14, 15, 16]. The difference on the time response between both turns them in sort of complementary equipment (as in the case of FC and battery).

In order to introduce the technological application, the energy exchange is solved, in the first place, using liner controllers and standard procedure, i.e., by calculating the instantaneous load power, supplying the demanded power with the FC (restricting the rate and the maximum current), and keeping the bus voltage constant. This strategy is widely discuss in the technical literature and different strategies are proposed to achieve the desire energy transfer [17, 18, 19].

In a second step, and to establish a comparison between the two approaches, the new control strategy of energy flow (DSER), first introduce in [4, 5], and extended later to electrical systems [6], is applied to the multi source system. The DSER is based on a nonlinear transformation that instantaneously transfers energy between multiports. The flow direction and rate of change of the energy transfer, initially regulated by means of $\alpha(t)$ in a two ports system, is now extended to three ports introducing a more flexible interconnection matrix, i.e., by the inclusion of

the term $\beta_{ij}(t)$ which regulates the flow between ports i and j .

5.2 Description of the System

The multi-port system studied is composed by FC, represented by voltage characteristic curve of a FC stack (v_{FC}), a super capacitor as a storage device (C_{sc}) and a resistive variable load. This hybridization of the FC with a supercapacitor is a common structure used in vehicle technology [51]. The interconnection of the energy source, energy storage and electric load is achieved by 3 boost converters connected to a common dc bus, the scheme allows bidirectional energy flow for the supercapacitor and the load, yet only positive current for the FC. In this work the FC is modeled by its static characteristic, i.e. the terminal voltage is obtained by the demanded current according to graph shown in Fig. 5.1. The general scheme of the system is shown in Fig. 5.2.

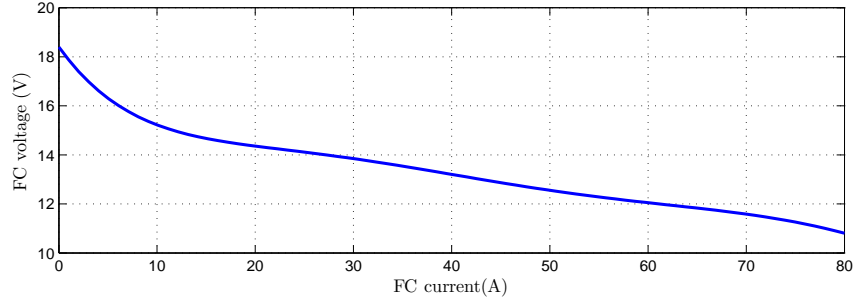


Figure 5.1: Static voltage v/s current characteristic of the FC stack.

The dynamic equations of the power system depicted in Fig. 5.2 are

$$\begin{aligned}
 L_{sc} \dot{i}_1(t) &= -R_{sc}i_1(t) - v_{sc}(t) + v_{dc}(t)u_1(t), \\
 L_{FC} \dot{i}_2(t) &= -R_{FC}i_2(t) - v_{dc}(t)u_2(t) + v_{FC}(t), \\
 L_L \dot{i}_3(t) &= -R_{LL}i_3(t) - v_L(t) + v_{dc}(t)u_3(t), \\
 C_{sc}\dot{v}_{sc}(t) &= i_1(t), \\
 C_L\dot{v}_L(t) &= i_3(t) - v_L(t)/R_L, \\
 C_{dc}\dot{v}_{dc}(t) &= -i_1(t)u_1(t) + i_2(t)u_2(t) - i_3(t)u_3(t),
 \end{aligned} \tag{5.1}$$

where $i_1(t)$, $i_2(t)$ and $i_3(t)$ are the inductor currents, $v_{sc}(t)$ is the voltage in the super capacitor, $v_{FC}(t)$ is the voltage of the FC stack, $v_{dc}(t)$ is the voltage in the

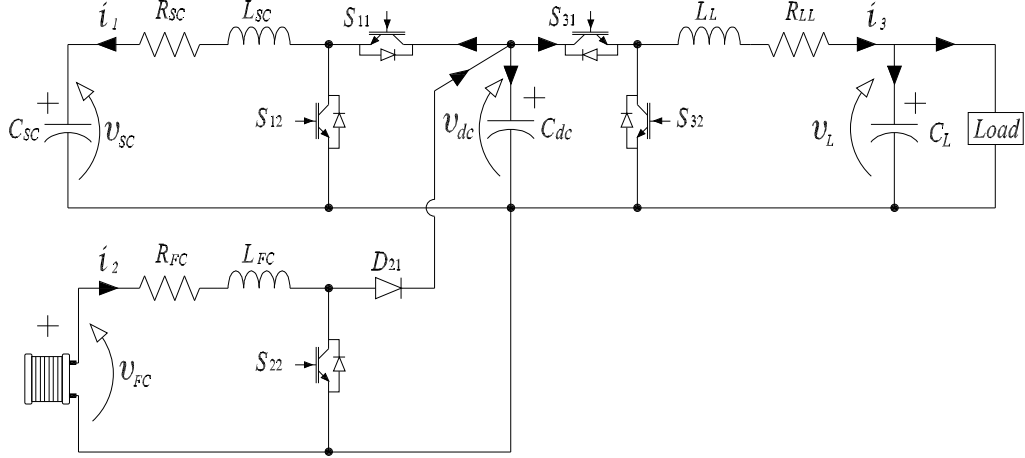


Figure 5.2: Interconnection scheme of the FC, super capacitor and electric load.

capacitor of the dc bus interconnection, $v_L(t)$ is voltage of the electric load and $u_1(t)$, $u_2(t)$ and $u_3(t) \in (0, 1)$ are the duty cycles of the switches, hence the control signals. Since the super capacitor compensates the low dynamic of the the FC, it must supply energy only during high power demand, thus the voltage of this storage device is considered to be varying in the range of 7 to 14 V. The voltage of the the dc bus capacitor must be kept constant on 40 V, as it is shown in the next section, this condition is guarantee by the inclusion of an external voltage control loop. In order to test the dynamic response of the system, the load is time-varying power unit and can take values in the range of -200 to 500 W at 12V.

5.3 Standard Approach of the Energy Management

Different solutions can be found in the literature in order to solve this energy flow control problem [52], [53], the strategy chosen in the present work operates as follows.

- i_1 controller: Due to its flexibility and fast dynamic the controller of the super capacitor current i_1 , is chosen to be the fastest of the system.
- i_2 controller: Yet the controller of the current i_2 is designed as fast as the controllers i_1 , its reference i_2^* comes from a low-pass filter, hence the behavior of the whole system in close-loop is slower. The FC is the main energy supply

of the system, consequently $v_{FC} \times i_2^*$ must match the power demanded by the load.

- i_3 controller: This controller is designed as fast as the controllers i_1 , its reference i_3^* comes from the v_L controller.
- v_{dc} controller: Since the controller of the current i_1 must respond to sudden changes of the demanded load, this device is also in charge of controlling the bus voltage v_{dc} . Therefore, i_1^* is the output of the v_{dc} controller.
- v_L controller: A common practice in power electronics applications is to supply constant voltage to a non-regulate load, e.g., the domiciliary electric supply. Therefore, and since the device in this port is a bidirectional converter, v_L is controlled indirectly by controlling the current of the inductor.
- v_{sc} controller: Given that the operation of the super capacitor depends on its state, the demanded load power, and the operation condition of the fuel cell, the logic behind its control is complex. In this work a simple strategy is used in order to charge the supercapacitor when the voltage v_{sc} is under its reference; in case of not being fully demanded, the FC is used and if the load is regenerating, the energy coming from the load charges the supercapacitor.

The specification of the controllers is accomplished by using liner control techniques explained in [9, 47]. Therefore, the first step is to linearize system around the operation point later, and by a small signal analysis and simplification, the dynamic of each state variable it is obtained.

In order to designed the liner PI controllers of the system we write the linearize system,

$$\begin{bmatrix} \Delta \dot{i}_1 \\ \Delta \dot{i}_2 \\ \Delta \dot{i}_3 \\ \Delta \dot{v}_{sc} \\ \Delta \dot{v}_L \\ \Delta \dot{v}_{dc} \end{bmatrix} = \begin{bmatrix} A \end{bmatrix} \begin{bmatrix} \Delta i_1 \\ \Delta i_2 \\ \Delta i_3 \\ \Delta v_{sc} \\ \Delta v_L \\ \Delta v_{dc} \end{bmatrix} + \begin{bmatrix} \frac{v_{dc0}}{L_{sc}} & 0 & 0 \\ 0 & \frac{v_{dc0}}{L_{FC}} & 0 \\ 0 & 0 & \frac{v_{dc0}}{L_L} \\ 0 & 0 & 0 \\ 0 & 0 & 0 \\ \frac{-i_{10}}{C_{dc}} & \frac{i_{20}}{C_{dc}} & \frac{-i_{30}}{C_{dc}} \end{bmatrix} \begin{bmatrix} \Delta u_1 \\ \Delta u_2 \\ \Delta u_3 \end{bmatrix} + \begin{bmatrix} 0 \\ \frac{\Delta P_{FC}}{L_{FC}} \\ 0 \\ 0 \\ 0 \\ 0 \end{bmatrix} \quad (5.2)$$

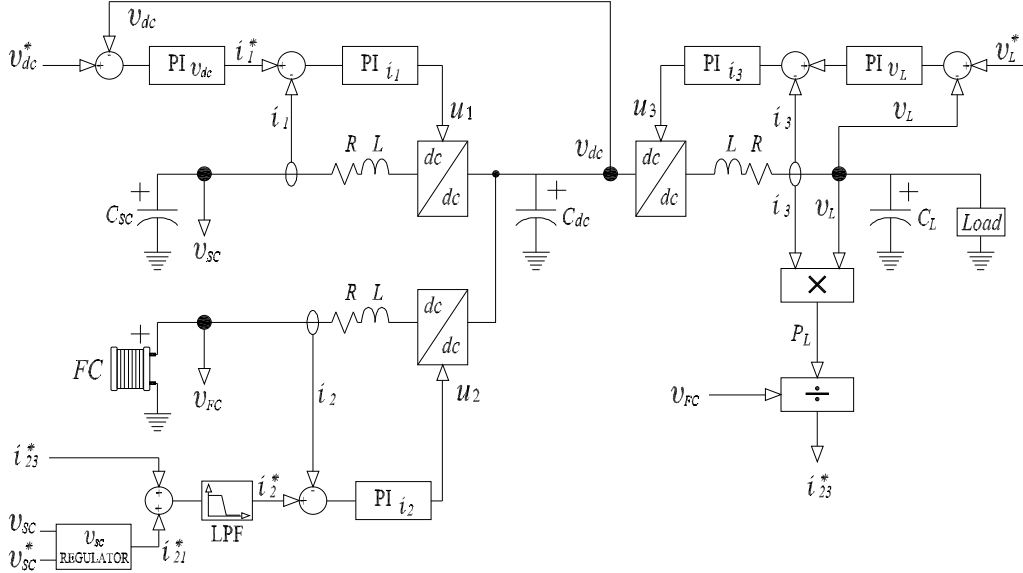


Figure 5.3: Standard control scheme of a multi-source multi-load system.

with

$$\left[\begin{array}{c} A \end{array} \right] = \left[\begin{array}{cccccc} \frac{-R_{sc}}{L_{sc}} & 0 & 0 & \frac{-1}{L_{sc}} & 0 & \frac{U_{10}}{L_{sc}} \\ 0 & \frac{-R_{FC}}{L_{FC}} & 0 & 0 & 0 & \frac{-U_{20}}{L_b} \\ 0 & 0 & \frac{-R_{LL}}{L_L} & 0 & \frac{-1}{L_L} & \frac{U_{30}}{L_L} \\ \frac{1}{C_{sc}} & 0 & 0 & 0 & 0 & 0 \\ 0 & 0 & \frac{1}{C_L} & 0 & \frac{1}{R_L C_L} & 0 \\ \frac{-U_{10}}{C_{dc}} & \frac{U_{20}}{C_{dc}} & \frac{-U_{30}}{C_{dc}} & 0 & 0 & 0 \end{array} \right]. \quad (5.3)$$

Where U_{10} , U_{20} , U_{30} , v_{dc0} , i_{10} , i_{20} and i_{30} , are the states values in the operation point and Δx represents the deviation of the variable x from its operation point x_0 .

5.3.1 Current Controllers Design

From the linearized system (5.2) and (5.3), and considering that the capacitance of C_{sc} , C_{dc} and C_L are big enough to kept the voltages constant during operation of the system, it is assumed that the dynamics of the currents are governed by a

first-order type of system, whose equations are,

$$\Delta i_1 = \frac{\Delta U_1 - v_{dc0}}{sL_{sc} + R_{sc}}, \quad (5.4)$$

$$\Delta i_2 = \frac{\Delta U_2 - v_{dc0}}{sL_{FC} + R_{FC}}, \quad (5.5)$$

$$\Delta i_3 = \frac{\Delta U_3 - v_{dc0}}{sL_L + R_{LL}}. \quad (5.6)$$

Therefore, PI controllers of the form $k_j(sT_j + 1)/sT_j$ can provide an appropriate performance in close-loop, thus the resulting close-loop dynamics are

$$\frac{\Delta i_1}{\Delta i_1^*} = \frac{k_{i1}v_{dc0}}{T_{i1}L_{sc}} \frac{sT_{i1} + 1}{s^2 + s(\frac{R_{sc} + k_{i1}v_{dc0}}{L_{sc}}) + \frac{k_{i1}v_{dc0}}{T_{i1}L_{sc}}}, \quad (5.7)$$

$$\frac{\Delta i_2}{\Delta i_2^*} = \frac{k_{i2}v_{dc0}}{T_{i2}L_{FC}} \frac{sT_{i2} + 1}{s^2 + s(\frac{R_{FC} + k_{i2}v_{dc0}}{L_{FC}}) + \frac{k_{i2}v_{dc0}}{T_{i2}L_{FC}}}, \quad (5.8)$$

$$\frac{\Delta i_3}{\Delta i_3^*} = \frac{k_{i3}v_{dc0}}{T_{i3}L_L} \frac{sT_{i3} + 1}{s^2 + s(\frac{R_{LL} + k_{i3}v_{dc0}}{L_L}) + \frac{k_{i3}v_{dc0}}{T_{i3}L_L}}. \quad (5.9)$$

As it can be seen from (5.7), (5.8) and (5.9), due to the equivalence values of inductances and resistors, the dynamics respond identically. Moreover, the dynamics of the currents can be approximated by a second order system, in which case we can identify the damping ratio of the close-loop system as

$$\xi_{i1} = \frac{k_{i1}v_{dc0} + R_{sc}}{2L_{sc}\omega_{i1}}, \quad \xi_{i2} = \frac{k_{i2}v_{dc0} + R_{FC}}{2L_{FC}\omega_{i2}} \quad \text{and} \quad \xi_{i3} = \frac{k_{i3}v_{dc0} + R_{LL}}{2L_L\omega_{i3}}, \quad (5.10)$$

and the oscillation frequency of the close-loop current controller as

$$\omega_{i1} = \sqrt{\frac{k_{i1}v_{dc0}}{T_{i1}L_{sc}}}, \quad \omega_{i2} = \sqrt{\frac{k_{i2}v_{dc0}}{T_{i2}L_{FC}}} \quad \text{and} \quad \omega_{i3} = \sqrt{\frac{k_{i3}v_{dc0}}{T_{i3}L_L}}. \quad (5.11)$$

Choosing the settling time for the currents of the system (T_{Si1} , T_{Si2} and T_{Si3}) and a proper damping ratio (ξ_{i2} , ξ_{i2} and ξ_{i3}) in order to limit the overshoot, from (5.10) and (5.11) the constants of the PI controllers T_{i1} , T_{i2} , T_{i3} , k_{i1} , k_{i2} , and k_{i3} are calculated. Since the system is composed by pulse wide modulated (PWM) dc converters with switching frequency equal to 20000 Hz (carrier frequency f_Δ) and the control signals must respond slower than this frequency in order to ensure the correct operation, the settling time is chosen 10 times $1/f_\Delta$ ($T_{Si1} = T_{Si2} = T_{Si3} = 10/f_\Delta$). To guaranty a fast dynamic response with 10% maximum overshoot, the value of the damping ratio must be in the range $0.6 < \xi_i < 1$, in this work is chosen as $\xi_{i1} = \xi_{i2} = \xi_{i3} = 0.707$.

5.3.2 Dc–bus Voltage Controller Design

A convenient and practical solution to control the voltage in the dc–bus (v_{dc}) is by regulating the energy supplied by the super capacitor, in other word the dc bus voltage is controlled by the super capacitor port [51, 54]. In order to decouple the voltage controller from the current controller and avoid internal resonance, the time response is set 10 times slower than the current controller, so the settling time of the voltage controller is $T_{Sv_{dc}} = 100/f_\Delta$. With this time decoupling it could be assume that $\Delta i_1 = \Delta i_1^*$ and that Δi_2 , Δi_3 , Δu_1 , Δu_2 and Δu_3 are approximately 0. Therefore, from the linearize system (5.2) and (5.3) we obtained the dynamic of the voltage v_{dc} in terms of the current i_1^* ,

$$\Delta v_{dc} = \frac{\Delta i_1^*}{sC_{sc}} \cdot \frac{U_{10}}{sC_{sc}}.$$

It can be seen that the dynamic corresponds to a first–order system and therefore a linear controller of the form $k_{v_{dc}}(sT_{v_{dc}} + 1)/sT_{v_{dc}}$ can provide good performance in close-loop. Thus the resulting close-loop dynamic is

$$\frac{\Delta v_{dc}}{\Delta v_{dc}^*} = \frac{k_{vdc}U_{10}}{T_{vdc}C_{dc}} \cdot \frac{sT_{vdc} + 1}{-s^2 + s(\frac{k_{vdc}U_{10}}{C_{dc}}) + \frac{k_{vdc}U_{10}}{T_{vdc}C_{dc}}}.$$
(5.12)

Since the close-loop dynamic behaves as a second–order system we can identify the damping ratio ($\xi_{v_{dc}}$) and the oscillation frequency ($\omega_{v_{dc}}$) of the close-loop system as

$$\xi_{vdc} = \frac{k_{vdc}U_{10}}{C_{dc}2\omega_{vdc}},$$
(5.13)

$$\omega_{vdc} = \sqrt{\frac{k_{vdc}U_{10}}{T_{vdc}C_{dc}}}.$$
(5.14)

Following the same design criteria of the current controllers and as it was mentioned before, to effectively decouple the two control loops, a settling time ($T_{Sv_{dc}}$) 10 times slower than the settling time of the current controller is chosen. Moreover, to ensure fast response and limit the overshoot to 10%, it is chosen $\xi_{v_{dc}} = 0.707$.

5.3.3 Load Voltage Controller Design

In order to provide the enough flexibility to the electric load, a boost dc converter regulates the output voltage of the load. Therefore, the the dynamics equation of the load voltage (v_L) is obtained from equations 5.2 and 5.3. Applying the same

Table 5.1: PI controllers parameters

Controller	k_{pPI}	k_{iPI}
Current i_1	0.02	40.72
Current i_2	-0.02	-40.72
Current i_3	0.02	40.72
Voltage v_{dc}	-10.65	-2150.11
Voltage v_L	5.44	537.52

time scaling criteria, i.e., assuming that $\Delta i_3 = \Delta i_3^*$, the dynamic of the voltage v_L can be written as,

$$\Delta v_L = \frac{\Delta i_3^*}{sC_L - \frac{1}{R_L}},$$

which dynamic corresponds to a first-order system. Therefore, a linear controller of the form $k_{v_L}(sT_{v_L} + 1)/sT_{v_L}$ can provide good performance in close-loop. Hence the close-loop dynamic is

$$\frac{\Delta v_L}{\Delta v_L^*} = \frac{k_{v_L}}{T_{v_L} C_L} \frac{sT_{v_L} + 1}{s^2 + s(\frac{k_{v_L}}{C_L} - \frac{1}{C_L R_L}) + \frac{k_{v_L}}{T_{v_L} C_L}}. \quad (5.15)$$

Given that the close-loop dynamic behaves as a second-order system we can identify the damping ratio (ξ_{v_L}) and the oscillation frequency (ω_{v_L}) of the close-loop system as

$$\xi_{vdc} = \frac{k_{v_L} - \frac{1}{R_L}}{C_L 2\omega_{v_L}}, \quad (5.16)$$

$$\omega_{v_L} = \sqrt{\frac{k_{v_L}}{T_{v_L} C_L}}. \quad (5.17)$$

As in the case of v_{dc} controller, a settling time (T_{Sv_L}) 10 times slower than the settling time of i_3 is chosen, and to ensure fast response and limit the overshoot to 10%, ξ_{v_L} is set to 0.707. Finally, the different controller parameters used in this work are shown in Table 5.1.

5.3.4 Stability of the Close-Loop System

In order to study the stability of the complete systems, the eigenvalues of the matrix A of the linearized close-loop system are obtained. Since the super capacitor is

a limited energy storage device, whatever operating point of its current i_1 (except 0), will end in a complete discharge or an explosion of its terminal voltage v_{sc} . Either way, the final result is the instability of the whole system. Therefore, in this particular analysis the super capacitor is replace by a voltage source. After replacing the control signals ($u_1(t)$, $u_2(t)$ and $u_3(t)$) with the corresponding outputs of the *PI* controllers shown in (5.1), the equations of the close-loop system are obtained (5.18). Where k_p and k_i are the proportional and integral gain constants of the controllers of the system obtained from the values of Table 5.1.

$$\begin{aligned}
\dot{\hat{i}}_1 &= [-R_{sc}i_1 - v_{sc} + kp_{i1}v_{dc}(kp_{vdc}\tilde{v}_{dc} + ki_{vdc}x_{11} - i_1) + \\
&\quad + ki_{i1}x_7v_{dc}]/L_{sc} \\
\dot{\hat{i}}_2 &= [-R_{FC}i_2 - kp_{i2}v_{dc}\tilde{i}_2 - ki_{i2}x_8v_{dc} + v_{FC}]/L_{FC} \\
\dot{\hat{i}}_3 &= [-R_{LL}i_3 - v_L + kp_{i3}v_{dc}(kp_{vL}\tilde{v}_L + ki_{vL}x_{10} - i_3) + \\
&\quad + ki_{i3}x_9v_{dc}]/L_L \\
\dot{v}_L &= [i_3 - v_L/R_L]/C_L \\
\dot{v}_{dc} &= [-kp_{i1}i_1(kp_{vdc}\tilde{v}_{dc} + ki_{vdc}x_{11} - i_1) - ki_{i1}x_7i_1 + kp_{i2}i_2\tilde{i}_2 + \\
&\quad + ki_{i2}x_8i_2 - kp_{i3}i_3(kp_{vL}\tilde{v}_L + ki_{vL}x_{10} - i_3) - ki_{i3}x_9i_3]/C_{dc} \\
\dot{x}_7 &= i_1^* - i_1 \\
\dot{x}_8 &= i_2^* - i_2 \\
\dot{x}_9 &= i_3^* - i_3 \\
\dot{x}_{10} &= v_L^* - v_L \\
\dot{x}_{11} &= v_{dc}^* - v_{dc}.
\end{aligned} \tag{5.18}$$

The system (5.18) is of the form $\dot{x}(t) = f(x(t), u(t), p(t))$, where x are the states of the system plus the states of the controllers, the control inputs (u) are no longer available since they were replaced and p is the voltage sources of the system. In order to obtain a linear representation of the system, in the form $\Delta\dot{x}(t) = A\Delta x(t) + B\Delta u(t) + E\Delta p(t)$, the *Jacobians* of $f(x(t), u(t), p(t))$ is calculated as it is shown below.

$$A = \frac{\partial f(x, u, p)}{\partial x} \Bigg|_{\substack{x = x_0 \\ u = u_0 \\ p = p_0}}, \quad B = \frac{\partial f(x, u, p)}{\partial u} \Bigg|_{\substack{x = x_0 \\ u = u_0 \\ p = p_0}} \quad \text{and} \quad E = \frac{\partial f(x, u, p)}{\partial p} \Bigg|_{\substack{x = x_0 \\ u = u_0 \\ p = p_0}},$$

where Δ denotes the variation around the operation point. Notice that $B = 0$ since the control inputs have been replaced by the controller outputs. The eigenvalues

of the matrix A are presented in Fig. 5.4, it can be seen that the poles of the system are located in open left half plane and also in the origin, hence, the stability analysis of system is not straight forward and can be carried out by tools available in literature such as the center manifold theory [11].

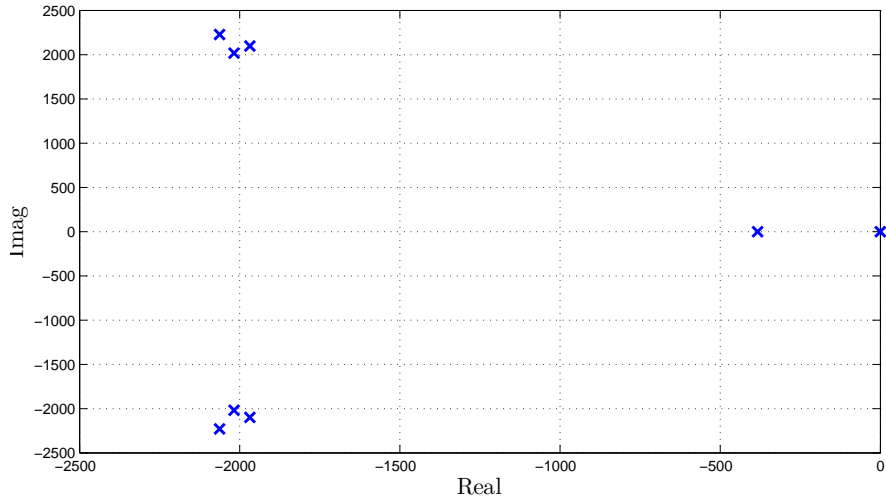


Figure 5.4: Eigenvalues of the close-loop system.

In order to evaluate the impact over the stability of the v_{dc} control loop, in Fig. 5.5 are presented the evolution of the eigenvalues for different values of the constants kp_{vdc} and ki_{vdc} . In Fig. 5.5(a) the value of kp_{vdc} is kept constant to its designed value (-10.65), it can be seen that while ki_{vdc} is increasing in magnitude one eigenvalue is displaced to right half plane, the cross of the axis take place when $ki_{vdc} = -125000$. In Fig. 5.5(b) the value of ki_{vdc} is kept constant in its designed value (-2150.11) while kp_{vdc} is varying from $-1m$ to -500 , as in the previous case, one eigenvalue start decreasing until it cross to the right semi plane when $kp_{vdc} = -98$, thus the system becomes unstable.

5.3.5 Simulation Results

Simulation results using Matlab Simulink have been carried out to illustrate the performance of the system. Since a long simulation period is required (100 s) to produce variation on the supercapacitor voltage and in this way, generate the different working conditions, only an average simulation is performed. An arbitrary load power profile is imposed with different power demanded levels and variation ramps.

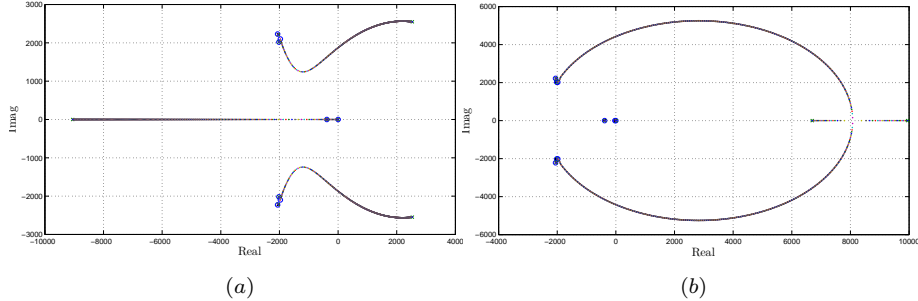


Figure 5.5: Evolution of the eigenvalues. (a) Fix kp and $-0.1m < ki_{vdc} < -1M$. (b) Fix ki and $-1m < kp_{vdc} < -500$.

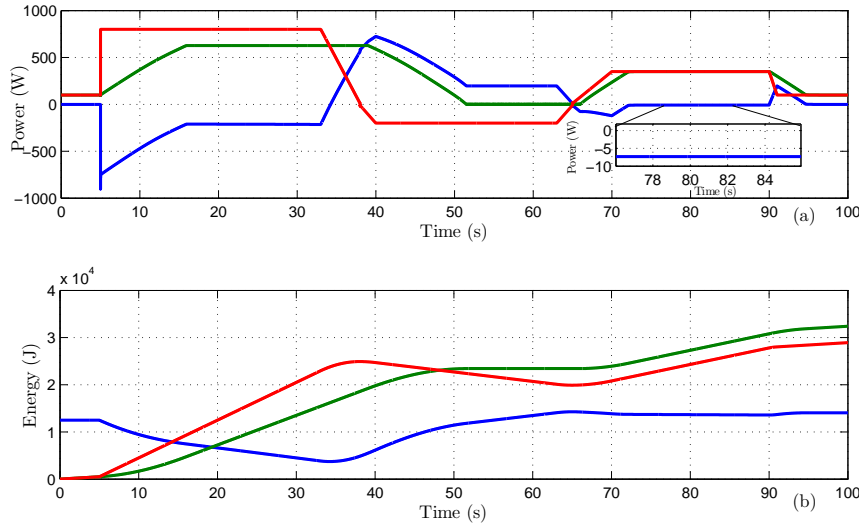


Figure 5.6: Energy flow and power delivered in the load (red), FC (green), and supercapacitor (blue). (a) Power demanded or supplied by the different components. (b) Energy stored and energy flow in the different components, energy flow at the load connection port in red, the energy supplied by the FC in green, and the energy stored by the supercapacitor is un blue.

In Fig. 5.6(a) are depicted the instantaneous power in the different ports of the system. As it is illustrated in red, the load power (\dot{H}_L) starts at 100W and at 5s changes to 800W where it remains for 28s. At time 33s a negative ramp during 7s is imposed, consequently the load power crashes 0 at time 38s and reaches -200W at time 40, where it remains during the period (40, 63). At time 63s a positive

ramp makes the load power cross zero again (time 65) and reaches 350W at time 70, it remains in this value for 20s. At time 90s a last negative ramp is imposed during 1s, finally the load power remains in 100W until the end of the simulation

The FC power (\dot{H}_{FC}) delivered is shown in Fig. 5.6(a), in green. As can be seen, due to the utilization of a lowpass filter, the FC is unable to follow the abrupt changed of the power demanded by the load. Therefore, at time 5 the FC power starts increasing at its maximum allowed rate (the equivalent to 4A per second) until it reaches its maximum power capacity 628W. The FC continues delivering the maximum power until time 39, even though the power load has reduced the FC has to recharge the supercapacitor. After time 39 the FC power starts decreasing until it reaches 0 at time 52, it remains in 0 until time 66, during all this last period (39, 66) the supercapacitor has been recharged by the regeneration of the load. During the interval (66, 73) the FC power increases at its maximum rate until it reaches the load power demand (350W), the difference is supplied by the supercapacitor. During the period (90, 94.7) the opposite situation occurs, the FC power decreases at its maximum rate until it reaches the load power demand (100W) and the difference is compensated by the supercapacitor.

The power supplied, or demanded, by the supercapacitor (\dot{H}_{sc}) is shown in blue in Fig. 5.6(a). The operation of this device is mainly governed by the dynamics limitations of the FC to deliver the load power and also by the changing operational losses of the system. In agreement with this, and considering that the losses are almost negligible, is clear that during all the operation the supercapacitor power is the difference between the load power and the FC power. This effect is illustrated in the magnified inset where, while the demanded power is supplied by the FC, the power delivered by the supercapacitor is 7.33W (equivalent to the losses in that operation point).

In Fig. 5.6(b) are shown the energy profile of the load (H_L), of the FC (H_{FC}), and of the supercapacitor (H_{SC}), in red, green, and blue, respectively. The capacitor C_L is considered as a filter device, therefore, there is no stored energy and its initial value is 0, the same situation occurs with H_{FC} . It can be seen that the evolution of the energy is in agreement with the instantaneous power of each device, e.g., when \dot{H}_L becomes negative, H_L starts decreasing. Since the FC can not stand negative energy flow its profile is always constant or increasing. Due to its physical characteristics, H_{SC} has an initial condition different from 0 ($H_{SC}(0) > 0$) and although, it supplied considerable amount of energy, the control strategy kept it around a defined energy stored level (12.5 kJ).

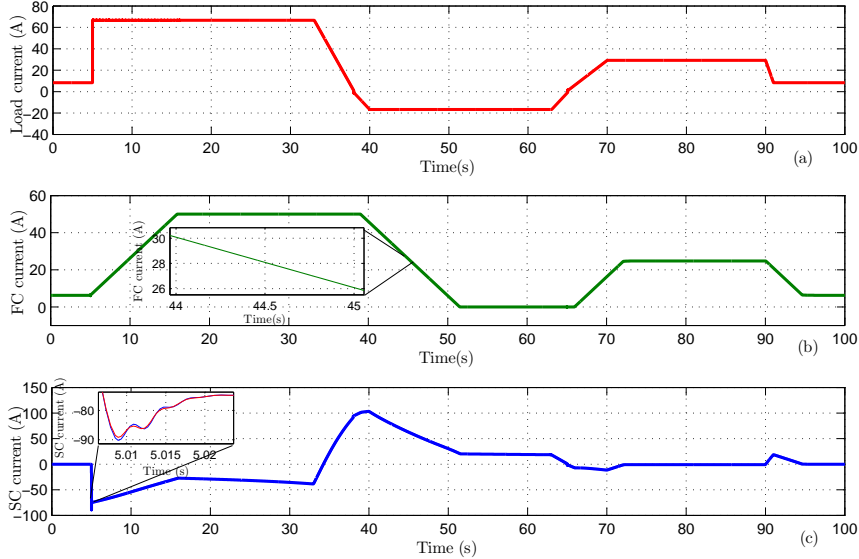


Figure 5.7: Current of the supercapacitor, load, and FC.

The current of the different devices and their references are shown in Fig. 5.7. In Fig. 5.7(a) the load current is presented, as can be seen the shape is close to its power profile, it starts at 8.33A and at time 5 it goes to 66.67A where it remains during the period (5.03, 33). At time 33, a decreasing ramp imposed during 7s, drives i_2 to -16.65A, where it stayed during the interval (40, 63). During the period (70, 90), and due to a positive ramp, the load current reaches 29.2A, yet at time 90 an other change in the reference drives it to its final value 8.3A, where it remains until the end of the simulation. As a general description of the FC current (i_3) profile, shown in Fig. 5.7(b), it can be said that is a smooth shape of the load current between the limits (0, 50)A. Although, this is a general outline is not totally accurate, a particular working condition could occur when the supercapacitor requires energy supply from the FC without any intervention of the load. As can be seen in the magnified inset, the maximum change rate of current (4A per second) limits, not only the current risings, but also the the decreasing of i_3 .

As it was said, the operation of the supercapacitor is governed by a complex control logic, therefore, i_1 (shown in Fig. 5.7(c)) has the same general shape as \dot{H}_{sc} . Given that during the interval (0, 5), C_{sc} compensates only the losses, i_1 is -0.05A, yet at time 5 it response quickly to supply the demanded energy by the

load and it reaches its lower value -90A. In the inset is shown the effect of the controller over i_1 , it can be seen that the current follows accurately its reference, in the same way as i_2 and i_3 . During the interval (5, 34.25), i_1 varies between 0 and 90A passing through a local minimum of -27.2A at 16s and finally reaching 0A at 34.25s. After 34.25s it continues increasing, and therefore charging, until time 40 where it reaches its maximum value 103.5A. Although between 51.5s and 63s i_1 remains almost stable around 20A, after time 40 i_1 decreases permanently until 70s, it crosses 0 axis at time 65 and at last reaches -11.5A. In the interval (74, 90), i_1 behaves stable around -0.7A (compensating the losses of the system). At time 90s i_1 increases until it reaches 18.8A at time 91, therefore, C_{sc} recharges in the time interval (90.03, 95.5). In the last 2 seconds of the simulation, the current i_1 takes the value -0.05A in order to compensate the losses of the system.

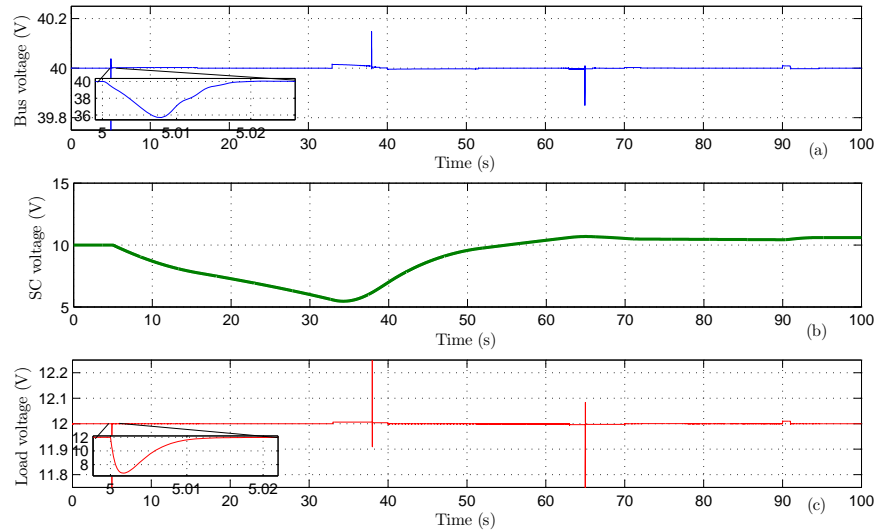


Figure 5.8: Voltage evolution of different capacitors of the system. (a) Voltage of the dc bus (v_{dc}). (b) Supercapacitor voltage (v_{sc}). (c) Load voltage (v_L).

The voltage of the C_{dc} is presented in Fig. 5.8(a), as can be seen the voltage follows closely its reference (40V) and worse displacement occurs at time 5 where the first load step is imposed. As can be seen from the magnified inset, v_{dc} reaches 36V at time 5.01 and then it starts recovering due to the controller operation. After 5.02s v_{dc} remains almost invariant around 40V, this performance might be deteriorated by considering the switching and sampling effect in the simulations. The time evolution of v_{sc} , shown in Fig. 5.8(b), is in agreement with what was

expected, since is considered as an ideal supercapacitor, the relation between H_{sc} (shown in blue in Fig. 5.6(b)) and the voltage is given by $H_{sc} = v_{sc}^2 C_{sc}/2$. The minimum value of v_{sc} (5.46V) occurs at time 34.25 and its maximum (10.68V) at time 65, is clearly that one of the control objectives is to keep the v_{sc} close to 10V. As in the case of v_{dc} , v_L (shown in Fig. 5.8(c)) follows accurately its reference, the maximum deviation (5.3V) from v_L^* take place at 5s, where the first demand step occurs. After this, only negligible oscillations, of less than 1V, can be found.

5.4 Dynamic Energy Router Application

The new approach used to solve the energy transfer problem, initially introduced in [4] and applied to power electronics technologies in [6], is based on a port representation of the system and a dynamic energy assignment on each port. The elements storage, source, and electric load, are connected to by an interconnection subsystem, in this case three dc power electronics converters with a common capacitor link.

This matrix used to assigned the references in each port, embodies a nonlinear transformation that instantaneously transfer the energy between the subsystems. The reference of flow direction and rate of change of energy between subsystems is manipulated by a single parameter, in this work a exact linerization via feedback will be applied in order to follow the energy references.

5.4.1 The Dynamic Energy Transfer Procedure

The system shown in Fig. 5.2 is given in its port representation in Fig. 5.9, it can be seen in this figure that each subsystem, Σ_1 , Σ_2 and Σ_3 correspond to the super capacitor, fuel cell and electric load, respectively.

As it is shown in Chapter 4 and in [6], is required that

$$v_1^\top(t)i_1(t) + v_3^\top(t)i_3(t) = v_2^\top(t)i_2(t), \quad (5.19)$$

where, $v_1 = v_{sc}$, $v_2 = v_{FC}$, and $v_3 = v_L$. Equation (5.19) ensures the power balance of the system. To achieve the energy exchange objective we couple the multiports by the interconnection subsystem (Σ_I), in our case the power electronics configuration shown in Fig. 5.2, which guarantee the energy exchange between the subsystems.

A general lossless interconnection, extension of the previous chapter, that ensures power balance for a 3 port system, is defined by

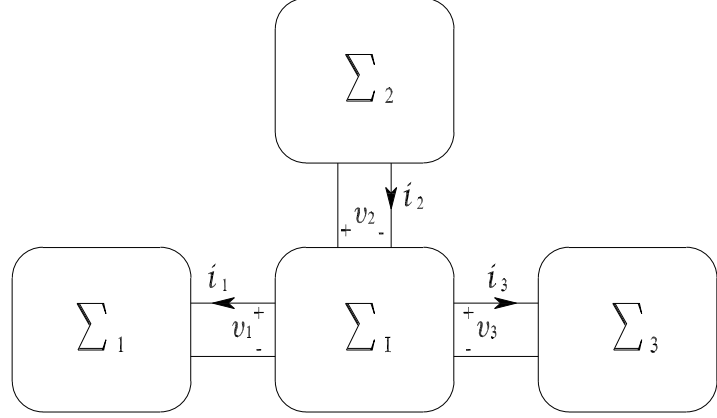


Figure 5.9: Multi-port representation of the power system.

$$\begin{bmatrix} 0 & \beta_{12}(t) & \beta_{13}(t) \\ \beta_{21}(t) & 0 & \beta_{23}(t) \\ \beta_{31}(t) & \beta_{32}(t) & 0 \end{bmatrix},$$

where $\beta_{ij}(t) \in \mathbb{R}^{m \times m}$ are chosen to ensure power-balance and satisfy equation (5.19). Therefore, the relation between the port variables is

$$\begin{bmatrix} i_1(t) \\ i_2(t) \\ i_3(t) \end{bmatrix} = \begin{bmatrix} 0 & \beta_{12}(t) & \beta_{13}(t) \\ \beta_{21}(t) & 0 & \beta_{23}(t) \\ \beta_{31}(t) & \beta_{32}(t) & 0 \end{bmatrix} \begin{bmatrix} v_{sc}(t) \\ v_{FC}(t) \\ v_L(t) \end{bmatrix}, \quad (5.20)$$

where,

$$\begin{aligned} \beta_{12}(t) &= \alpha_{12}\phi_1 v_{sc} v_{FC} v_L^2, \\ \beta_{13}(t) &= \alpha_{13}\phi_1 v_{sc} v_{FC}^2 v_L, \\ \beta_{21}(t) &= \alpha_{21}\phi_2 v_{sc} v_{FC} v_L^2, \\ \beta_{23}(t) &= \alpha_{23}\phi_2 v_{sc}^2 v_{FC} v_L, \\ \beta_{31}(t) &= \alpha_{31}\phi_3 v_{sc} v_{FC}^2 v_L, \\ \beta_{32}(t) &= \alpha_{32}\phi_3 v_{sc}^2 v_{FC} v_L. \end{aligned}$$

Multiplying both sides of equation (5.20) by $\begin{bmatrix} v_{sc}(t)^\top & v_{FC}(t)^\top & v_L(t)^\top \end{bmatrix}$ yields

$$\begin{bmatrix} v_{sc}^\top(t)i_1(t) \\ v_{FC}^\top(t)i_2(t) \\ v_L^\top(t)i_3(t) \end{bmatrix} = \begin{bmatrix} v_{sc}^\top(t)\beta_{12}(t)v_{FC}(t) + v_{sc}^\top(t)\beta_{13}(t)v_L(t) \\ v_{FC}^\top(t)\beta_{21}(t)v_{sc}(t) + v_{FC}^\top(t)\beta_{23}(t)v_L(t) \\ v_L^\top(t)\beta_{31}(t)v_{sc}(t) + v_L^\top(t)\beta_{32}(t)v_{FC}(t) \end{bmatrix}. \quad (5.21)$$

Replacing the values of $\beta_{ij}(t)$ in equation (5.21), we can rewrite it as

$$\begin{bmatrix} \dot{H}_{sc}(t) \\ \dot{H}_{FC}(t) \\ \dot{H}_L(t) \end{bmatrix} = \begin{bmatrix} (\alpha_{12}(t) + \alpha_{13}(t))\phi_1(t)v_{sc}^2(t)v_{FC}^2(t)v_L^2(t) \\ (\alpha_{21}(t) + \alpha_{23}(t))\phi_2(t)v_{sc}^2(t)v_{FC}^2(t)v_L^2(t) \\ (\alpha_{31}(t) + \alpha_{32}(t))\phi_3(t)v_{sc}^2(t)v_{FC}^2(t)v_L^2(t) \end{bmatrix}. \quad (5.22)$$

The energy transfer can be regulated by choosing appropriately the values of $\alpha_{ij}(t)$, e.g., $\alpha_{21}(t)$ will regulate the direction and rate of change between Σ_2 and Σ_1 . By suitable selection of ϕ_j it is possible to modulate the contribution of each multiport to the overall power delivered, $\phi_j : \mathbb{R}^m \rightarrow \mathbb{R}^m$ are first–third quadrant mappings. Finally the current reference of the system are given by

$$\begin{aligned} i_1^*(t) &= [\alpha_{12}(t) + \alpha_{13}(t)]\phi_1(t)v_{sc}(t)v_{FC}^2(t)v_L^2(t), \\ i_2^*(t) &= [\alpha_{21}(t) + \alpha_{23}(t)]\phi_2(t)v_{sc}^2(t)v_{FC}(t)v_L^2(t), \\ i_3^*(t) &= [\alpha_{31}(t) + \alpha_{32}(t)]\phi_3(t)v_{sc}^2(t)v_{FC}^2(t)v_L(t). \end{aligned} \quad (5.23)$$

Where, $\alpha_{31}(t) + \alpha_{32}(t) = \alpha_3(t)$ which is a time variable obtained from the load profile, given that no specific restriction is imposed over the load, neither over the supercapacitor, $\phi_1(t) = \phi_3(t) = 1$, and $\phi_2(t)$ is chosen such that a maximum magnitude (50A maximum) and maximum rate of change current (4A per second) are ensured.

5.4.2 Controller Design

In order to track the references defined in equation (5.23) a feedback linearization, considering the internal dynamics of the system, is designed and tested in simulation. The system's outputs are defined as

$$\begin{aligned} h_1(t) &= i_1(t) - \alpha_1(t)v_{sc}(t)v_{FC}^2(t)v_L^2(t), \\ h_2(t) &= i_2(t) + \alpha_2(t)\phi_2(t)v_{sc}^2(t)v_{FC}(t)v_L^2(t), \\ h_3(t) &= i_3(t) + \alpha_3(t)v_{sc}^2(t)v_{FC}^2(t)v_L(t), \end{aligned} \quad (5.24)$$

where, $\alpha_1(t) = \alpha_{12}(t) + \alpha_{13}(t)$ and $\alpha_2(t) = \alpha_{21}(t) + \alpha_{23}(t)$. Therefore, the corresponding derivatives of the outputs are

$$\begin{aligned} \dot{h}_1(t) &= \dot{i}_1(t) - \alpha_1 \dot{v}_{sc} v_{FC}^2 v_L^2 - 2\alpha_1 v_{sc} v_{FC}^2 \dot{v}_L v_L^2, \\ \dot{h}_2(t) &= \dot{i}_2(t) - 2\alpha_2 v_{sc} \dot{v}_{sc} v_{FC} v_L^2 - 2\alpha_2 v_{sc}^2 v_{FC} v_L \dot{v}_L, \\ \dot{h}_3(t) &= \dot{i}_3(t) - 2\alpha_3 v_{sc} \dot{v}_{sc} v_{FC}^2 v_L - \alpha_3 v_{sc}^2 v_{FC}^2 \dot{v}_L. \end{aligned} \quad (5.25)$$

Table 5.2: Controller parameters

Output	k_{pI}	k_{iI}
Current error \hat{h}_1	-15000	-20000
Current error \hat{h}_2	-15000	-20000
Current error \hat{h}_3	-30000	-40000
Voltage error $\hat{h}_{1v_{dc}}$	15000	20000

Replacing (5.1) in equations ((5.25), and solving for the control variables, results in

$$u_1 = \left[\frac{R_{sc}i_1 + v_{sc}}{L_{sc}} + \frac{\alpha_1 i_1 v_{FC}^2}{C_{sc}} + \frac{2\alpha_1 v_{sc} v_L^2}{C_L} \left(i_3 - \frac{v_L}{R_L} \right) + \hat{h}_1 \right] \frac{L_{sc}}{v_{dc}}, \quad (5.26)$$

$$u_2 = \left[\frac{v_{FC} - R_{FC} i_2}{L_{FC}} - \frac{2\alpha_2 i_1 v_{sc} v_{FC} v_L^2}{C_{sc}} - \frac{2\alpha_2 v_{sc}^2 v_{FC} v_L}{C_L} \left(i_3 - \frac{v_L}{R_L} \right) - \hat{h}_2 \right] \frac{L_{FC}}{v_{dc}}, \quad (5.27)$$

$$u_3 = \left[\frac{R_{LL}i_3 + v_L}{L_L} + \frac{2\alpha_3 i_1 v_{sc} v_{FC} v_L^2}{C_{sc}} + \frac{\alpha_3 v_{sc}^2 v_{FC}^2}{C_L} \left(i_3 - \frac{v_L}{R_L} \right) + \hat{h}_3 \right] \frac{L_L}{v_{dc}}. \quad (5.28)$$

Where, \hat{h}_1 , \hat{h}_2 , and \hat{h}_3 are the the outputs of the system driven to 0, due to the fact that if $h_i = 0 \Rightarrow \hat{h}_i = 0$. Moreover, by means of a proportional plus integral (PI) controller is possible to stabilize the system and track the current references given in equation (5.23). As it is shown in Section 4.5.1, an indirect method to compensate the losses of the system is by keeping the voltage (v_{dc}) constant. Therefore, and following the strategy applied in Section 5.3, the output $h_{1v_{dc}} = v_{dc} - v_{dc}^*$ is defined and, by means of C_{sc} is controlled. Thus, equation (5.26) yields

$$u_1 = \left[\frac{R_{sc}i_1 + v_{sc}}{L_{sc}} + \frac{\alpha_1 i_1 v_{FC}^2}{C_{sc}} + \frac{2\alpha_1 v_{sc} v_L^2}{C_L} \left(i_3 - \frac{v_L}{R_L} \right) + \hat{h}_1 + \hat{h}_{1v_{dc}} \right] \frac{L_{sc}}{v_{dc}}. \quad (5.29)$$

As in the previous case, the output $h_{1v_{dc}}$ is driven to 0 using a PI controller. The parameters of the PI controllers are shown in Table 5.2.

5.4.3 Simulation Results

By means of Matlab Simulink, average simulations are carried out in order to evaluate the performance of this new approach. The simulations are achieved applying the same load profile defined in Section 5.3 to the power electronics

scheme depicted in Fig. 5.2. Given that, it is assumed that the demanded power (*Load*) from port 3 is governed externally, α_3 is imposed by the external load.

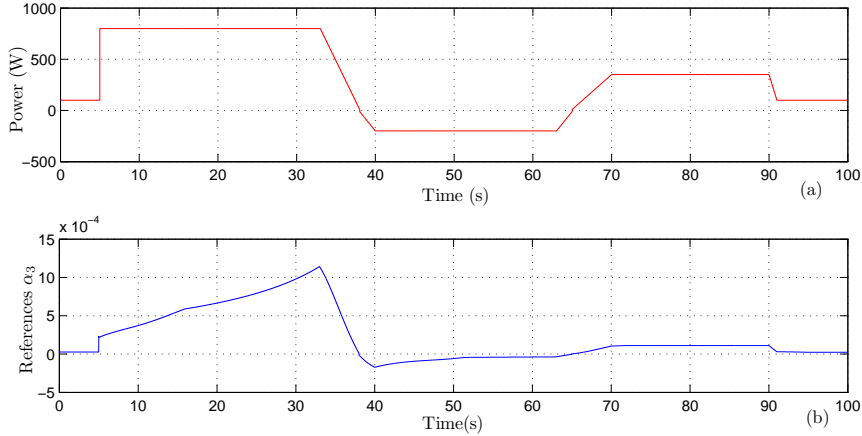


Figure 5.10: Time evolution of the load power and the corresponding reference α_3 . (a) Power profile of the load. (b) Reference α_3 that corresponds to the load power.

The power load profile, depicted in Fig. 5.10(a), has the same time evolution as the demanded power used in the previous section (see Fig. 5.6). As it is illustrated in Fig. 5.10(b), the reference α_3 required to achieve the desired power profile is shaped by the variations of the port voltages. Therefore, and unlike the results obtained Chapter 4, the shapes of the α_3 and the power load are not proportional to each other. At time 0 α_3 is 2.723×10^{-5} , it remains in this value until time 5 where it has a step change that drives it to 2.18×10^{-5} . In the interval [5, 33] α_3 increases permanently until it reaches its maximum value 1.1417×10^{-3} . α_3 decreases during the period [33, 40], it crosses 0 at 38s and it reaches its minimum value at 40s (-1.7233×10^{-4}). After time 40s α_3 starts rising with a rate shaped by the port voltages variations, it crosses 0 at time 65, at 70s it has an abrupt change of slope and continues increasing until it reaches 1.1131×10^{-4} at 90s. During the period [90, 100] α_3 decreases from 1.1131×10^{-4} to 2.4081×10^{-5} , initially it drops very fast up to 3.0723×10^{-5} , at this time (91s) a change of slope takes place and it stabilizes in its final value.

As it is shown in Fig. 5.11(a), the addition of the shapes of α_{12} and α_{13} results in the time evolution of α_1 . α_{12} (green) defines the energy exchange between ports

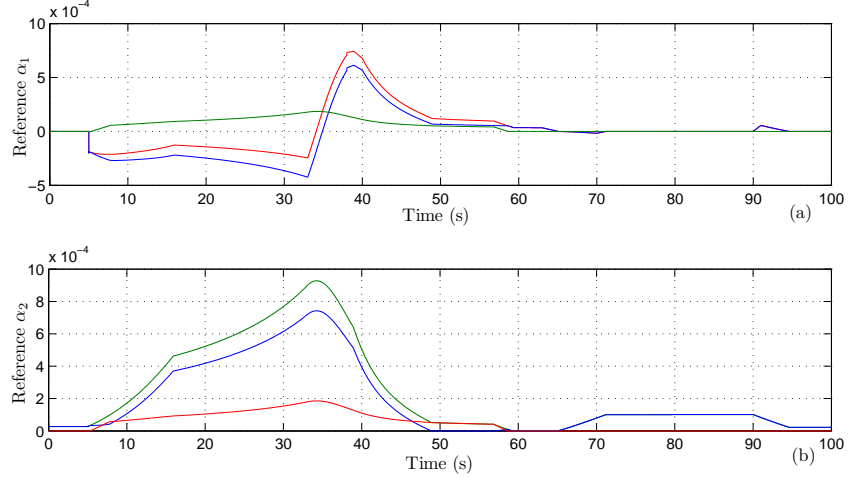


Figure 5.11: References α_1 and α_2 , and their corresponding components. (a) α_1 , α_{12} , and α_{13} in red, green, and blue, respectively. (b) α_2 , α_{21} , and α_{23} in green, red, and blue respectively.

1 and 2 (the supercapacitor and the FC), therefore, this reference comes from a recharging logic to maintain the supercapacitor in an operational voltage range. It can be seen that the energy flow demanded by port 3 is affected by the energy flow between ports 1 and 2, e.g., at time 20, the load demands energy equivalent to -2.475×10^{-4} (α_{13} in blue) yet, since there is an incoming flow of energy from the FC ($1.045 \times 10^{-4} = \alpha_{12}$) the overall energy flow is the equivalent to -1.432×10^{-4} (α_1 in red). As it was expected, the values of α_2 , α_{21} , and α_{23} are always positive, this results is achieved by the introduction of the mapping function ϕ_2 . Due to the current direction used in the simulation, the α_{12} and α_{21} are exactly the same. As in the case of port 1, the addition of α_{21} and α_{23} results in α_2 , and the addition of α_{13} and α_{23} gives α_3 .

The time evolution of the port power and energy is very close to the results obtained in section 5.3.5, by comparing figures 5.6(a) and 5.12(a) it is clear that the main difference is find in the interval (45, 60) seconds. Although, the power delivered to the load is the same, due to the criteria of references selection the energy flow inside the system follows a different pattern. At time 49, the power delivered by the FC (green) changes its tendency and remains in 152.25W until time 56.85, where it starts decreasing again until it reaches 0 at 59.35s. Due to the enforced power balance of the system, the supercapacitor power demand (blue) also remains constant (around 344W) after time 49, and decreases with the same

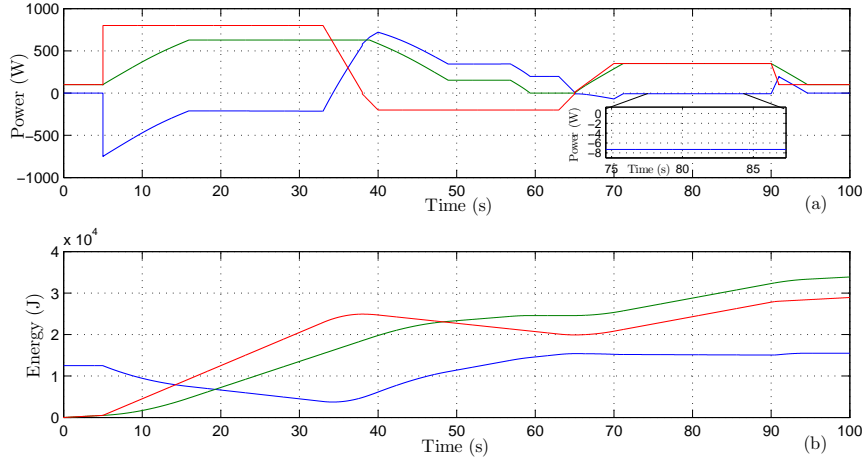


Figure 5.12: Power delivered and time evolution of the energy in the load (red), FC (green), and supercapacitor (blue). (a) Power demanded or supplied by the different components. (b) Energy flow in the connection port of the FC and load is shown in green and red, respectively. The energy stored in the supercapacitor is depicted in blue.

slope of the FC power delivered. The effect of the power delivered is no so evident in the energy flow graph (Fig. 5.12(b)), yet given that this behavior is due to the effect of α_{12} , the slope of the energy stored in the supercapacitor (blue) in the period (49, 59.35) is slightly larger than the result shown in Fig. 5.6(b). The behavior of the energy flow during the rest of the simulation time is close to the result shown in the previous section.

The shapes of the port currents of the system are also close to the results obtained in section 5.3.5. Since the track of the load power profile is one of the main objectives, the load current (shown in Fig. 5.13(a)) has the same time evolution as the result depicted in Fig. 5.7(a). The analogous effect to one occurred with the power delivered is produced over the FC current (i_2) due to the action of α_{12} . At 49s the current i_2 changes its tendency and remains constant in 10A until 56.85s where it recovers the decreasing tendency and gets to 0 at time 59.35. Due to the effect of α_{12} , as can be seen in Fig. 5.13(c) the change of reference is also reflected on the supercapacitor current (i_{sc}), which changes its slope and remains around 35A until time 56.85. In Fig. 5.13(c) is also depicted the reference of the supercapacitor current (i_{sc}^*) in order to illustrated the result of the losses compensation over the current reference, as can be seen in the magnified inset, the

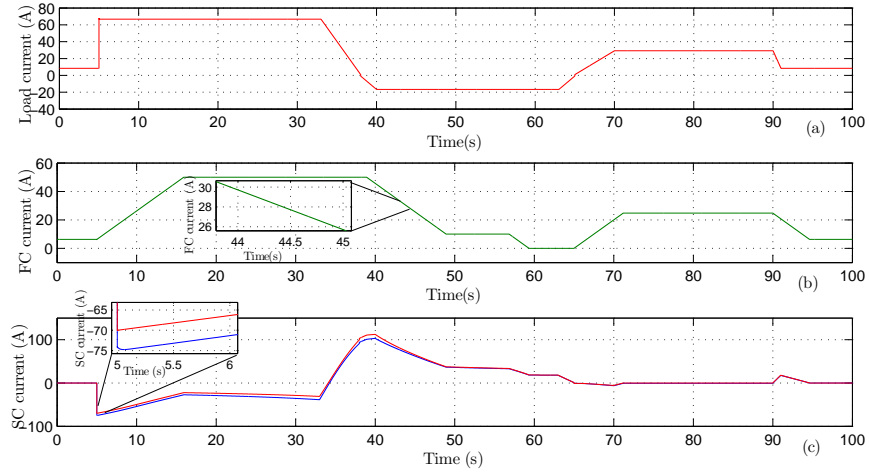


Figure 5.13: Time evolution of the current in the different ports. (a) Current of the load. (b) Current of the FC. (c) Current of the supercapacitor.

difference is around 5A and depends on the operation point. An improvement in comparison to the result of section 5.3.5 is the reduction of the peak values due to the abrupt changes of load demanded, in the previous result the current reaches -90A however the current using the DSER reaches only -75A.

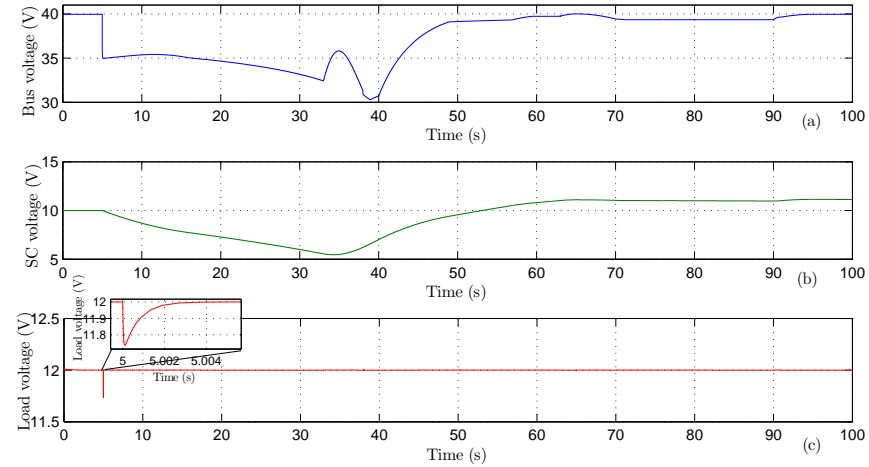


Figure 5.14: Voltage evolution of different capacitors of the system. (a) Voltage of the dc bus (v_{dc}). (b) Supercapacitor voltage (v_{sc}). (c) Load voltage (v_L).

A remarkable change in the time evolution of the bus voltage (v_{dc}) is observed,

as can be seen in Fig. 5.14(a) at time 5s the bus voltage decreases abruptly to 35V. All along the simulation v_{dc} is driven by the energy flow between the multiports, it reaches its minimum of 30.29V at 38.9s and presents a local maximum at 34.9s (35.8V). The supercapacitor voltage (Fig. 5.14(b)) behaves in the same way as in the result of the previous section, in the first part of the simulation, and due to the step change at 5s, it decreases until it reaches its minimum value 5.46V at 34.25s. After 34.25s, it recovers and reaches its initial value (10V) at 53.13s, in the last part of the simulation it presents and oscillation of 0.1V amplitude and finally it stabilize in 11.13V. As in the results shown in Fig. 5.8(c), the load voltage, depicted in Fig. 5.14(c), follows accurately its reference. Yet, unlike the previous result, a remarkable improvement regarding the spikes of the voltage is observed, it can be seen in the magnified inset, that in the worst case the voltage reaches 11.74V (at 5s).

5.5 Conclusions

An application of FC in a multi port system was developed in this chapter. In order to establish a comparison, the energy transfer was accomplished by two different approaches. In section 5.3 a linear control techniques was applied to achieved a standard energy exchange criteria and in section 5.4 the dynamic energy router (DSER), presented in a previous chapter, together with a nonlinear controller was applied to achieved the desired energy exchange. To test the performance of both approaches, average simulations are carried out using Matlab Simulink.

From the vast amount of technics available that addresses the energy exchange in a multiport system, the one propose in [51] is chosen. Given that the experimental laboratory equipment is oriented to vehicle application, is was suitable to chose a scheme that could be developed and evaluated in simulation, and later experimentally tested. To achieved the energy exchange criteria, linear controller were designed by linearizing the system around its operating point. Appropriate time scaling was used to avoid internal resonance and ensure a good performance. The overall result is that the applied technique of energy management, developed for hybrid application of FC, performed satisfactorily, the load was fed by the hybrid system, the bus voltage was controlled and it tracks its reference, and the constraints imposed over the FC were accomplished.

In a second approach of solving the energy exchange between the multiports, the DSER was adapted to the constrains and power demands of the chosen exam-

ple. A lossless interconnection matrix, that ensure the energy exchange between the ports, was defined. The objective of extend the results of the previous chapter is accomplished, i.e., the inclusion of constrains (mapping function ϕ_j) and an other port. In order to track this new references obtained from the DSER, and also considered as a result of the previous chapter, a controller based on a feedback linearization was designed. Experimentally tested in Chapter 4, the inclusion of a bus voltage controller was also applied in the control strategy. With different result as the standard approach, this new energy exchange technique performed satisfactorily, i.e., the hybrid system fed the demand of the load and the energy demanded from the FC was in agreement with its constraints (rate of change and maximum values). Although the main control objectives were accomplished, a secondary objective, which is the bus voltage control (v_{dc}), presented an oscillatory behavior. Given that an other result of the DSER approach is the reduction of the voltage spikes, it is possible that this voltage variation of the dc link turns the capacitor (C_{dc}) into the first (and fastest) energy storage device that supply energy to the load.

From this chapter it is concluded that is possible, and with an appropriate result, to apply the DSER to multiport system fed by FC stack. The flexibility of the technique make it suitable to control energy flow of complex devices as, supercapacitors or FC stacks.

Chapter 6

Conclusions and Future Work

6.1 Concluding Remarks

The study of the FC model bibliography made it possible to understand the dynamics and the variables that define the performance of the fuel cell in order to design a test bench system. The description of the FC model was given from the point of view of, FC stack model and the auxiliary components model. Since the objectives encourage it, especial attention was given to the FC stack model and to the compressor model.

One of the main objectives accomplished in the thesis is the design and setup of a fuel cell stack evaluation test bench (described in Chapter 3). Using as a starting restriction the chosen FC stack characteristics, the designing criteria and equipment technical information for the different subsystems were given (humidifiers, compressor, temperature regulation, air supply, and hydrogen supply). Although, the first objective is the evaluation of the FC, the instrumentation of the system permits to run experiments close to real applications, which is the challenging next stage of this long term project.

Due to its requirements, the signal conditioning is one of the major demanding developments. The adaptation of signals, avoiding the noise and accomplishing the power restriction, becomes a major challenge and to achieve it, custom PCB cards were designed and manufactured. From the point of view of control, standard controllers were designed to be applied in the auxiliary subsystems, i.e., bubbler temperature regulation, FC stack temperature regulation, and bubbler water refill. To ensure a safe and friendly operation, the data display, together with the digital protection system, are implemented taking advantage of the flexibilities of acquisition system and its interface software. In order to test the operation of the

integrate system and to show the potentials of the setup, final experimentation was carried out. These experimental experiences resulted in the obtention of characteristic curve of the FC, the acquisition of the internal equivalent impedance of the FC stack, and finally, the close loop operation of the FC stack.

In this thesis a device to dynamically transfer energy between electrical multiports (DSER) was presented and developed using standard switched power electronic devices. One of the central features of the DSER is the ability to control the direction and magnitude of the energy flow by changing only the parameter $\alpha(t)$, which comes directly from power port considerations. The performance of a non-dissipative dual-port DSER for a dc-to-dc application was verified by simulations and experimentally. Moreover, a dissipative dual-port DSER was also tested by the same means. Three different controllers were evaluated in order to achieve the objectives and compare performance. The overall result of the DSER is in agreement with what was expected for a non dissipative interconnection.

The linear controllers performed satisfactory around the operation point, the references were tracked accurately, the time response was in agreement with the design criteria, and the error was zero in steady state. The chosen sampling time did not impact over the system performance. With this initial test it was possible to be aware of the limitations of the power electronics electrical model and, therefore, introduce important adjustments.

Two other controllers, based on a feedback linearization (FL), were tested. A FL without considering all the dynamics of the system performed appropriately in simulation yet, due to the mismatch in the electrical model, the result of the experimentation was poor. The approximate differentiation filter (used for the FL) performed remarkably in simulation and experimentally. The FL that considers all the dynamics of the system, performed ideally in simulation, yet in experimentation the performance was slightly degraded. The dependency of the controller from the system parameters, impeded an ideal performance. Although, additional effort regarding the controller design should imply meaningful improvements.

The test over the power scheme without external energy supply yielded satisfactory results. The implemented control strategy (FL) enables the system to keep the bus voltage around its reference by altering the energy exchange. Furthermore, the energy exchange magnitude is no longer defined only by alpha. Due to this modification, the currents do not track the initial references and the bus voltage is no longer stabilized on its reference. Since the bus voltage control is a secondary objective of the control strategy, the fact that it was kept away from

its reference does not impact the main goal of the DSER.

In order to establish a comparison and evaluate the performance of the DSER in a multiports system fed by FC, test over a three port system with two different energy exchange approaches were accomplished. Firstly, linear control techniques were applied to achieve a standard energy exchange criteria, and later, the dynamic energy router (DSER), together with a nonlinear controller, were applied to achieved the desired energy exchange.

Given that the experimental laboratory equipment is oriented to vehicle application, it was suitable to chose a scheme that could be developed and evaluated in simulation, and later experimentally tested (hybridization of FC with supercapacitor). As a first approach, linear controllers were designed by linearizing the system around its operating point and appropriate time scaling was used to avoid internal resonance and ensure a good performance. The overall result is that the applied technique performed satisfactorily, the load was fed by the hybrid system, the bus voltage was controlled and it tracks its reference, and the constraints imposed over the FC were accomplished.

The second approach of solving the energy exchange between the multiports was carried out. The DSER was adapted to the constrains and power demands of the chosen example by reformulating the interconnection matrix (inclusion of β_{ij} and the mapping function ϕ_j). In order to track these new references obtained from the DSER, a controller based on a feedback linearization was designed. With different result as the standard approach, this new energy exchange technique performed satisfactorily, i.e., the hybrid system fed the demand of the load and the energy demanded from the FC was in agreement with its constraints (rate of change and maximum values). Although the main control objectives were accomplished, a secondary objective, which is the bus voltage control (v_{dc}), presented an oscillatory behavior.

6.2 Future Work

A clear opportunity of improvement exists from the point of view of the test bench instrumentation and hardware. For example, the signal conditioners of the temperature sensors can be upgraded to the ones presented in section 3.3.1 which are more accurate and reliable. Also, to have a precise control of the *RH* of the gases, new fitting devices could be installed in both input gases. Although, the actual fitting devices have heating units, which does not insure the complete absence of

condensation inside them. Since one of the objectives of the test bench, is the evaluation of new control strategies in an environment close to a real application, the integration of the system is essential to achieve this goal.

In order to run future experimentation without dealing with the transient of starting the system in a safe way, an automatized program could be developed (cool startup) and so the system can reach automatically the operation temperature and RH. The development and test of innovative control techniques that considered the nonlinearities of the system is the natural extension of the present work, respect to control theory. Also in the control field, the switch to a control strategy based on the differential pressure would approximate the system to real implementations.

One of the main features of working with an open FC stack is the possibility of isolating the stack of its auxiliary systems and looking into it with no perturbations, taking advantage of this, it is possible to research on; the state of health monitoring, FC stack models, or new operational variables. In this respect, the subject regarding the correlation of the state of health with the complex equivalent impedance is a clear next research step of the present work.

The potential applications of the DSER go beyond dc-to-dc configurations. Alternative topologies are available for handling ac-to-dc or ac-to-ac transfers. Furthermore, in this work the interconnection of voltage sources is considered, but in reality the energy in each port could be provided by current sources and a voltage-tracking system.

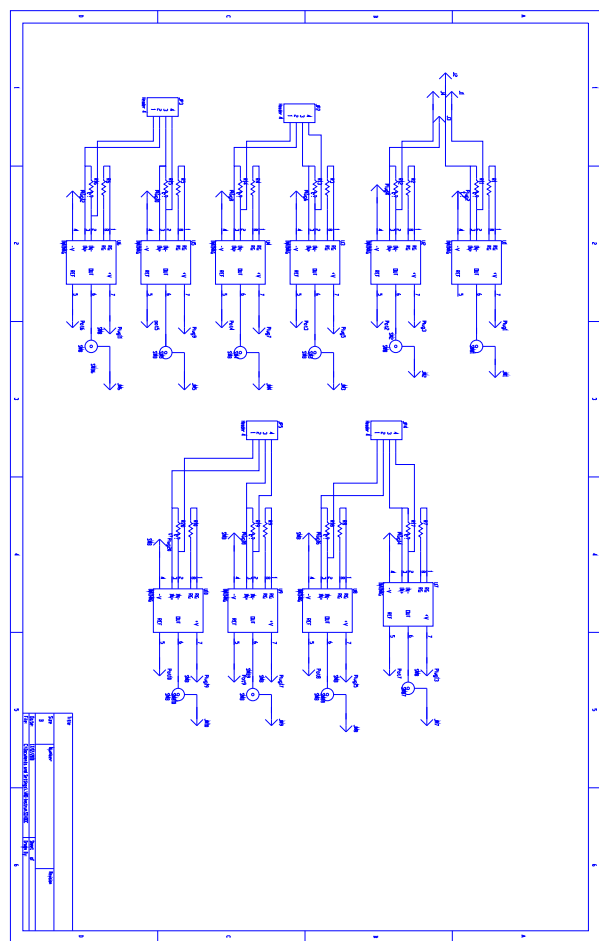
Regarding the control strategies used to implement the DSER, over a two and three port system, further efforts should be done in the improvement of the applied FL, mainly in the field of power converter modeling. The inclusion of an estimator of the dissipation resistance might be an attractive complementary tool for the FL. Also in this respect, due to its tracking features, additional tests should be done for the implementation of the approximate differentiation filter.

The dc-to-dc transfer is of special interest due to its application to interconnected systems fed by PEMFC. Experimental facilities are available [3] to test the performance of the DSER over FC fed systems, which is the next stage of this long term project.

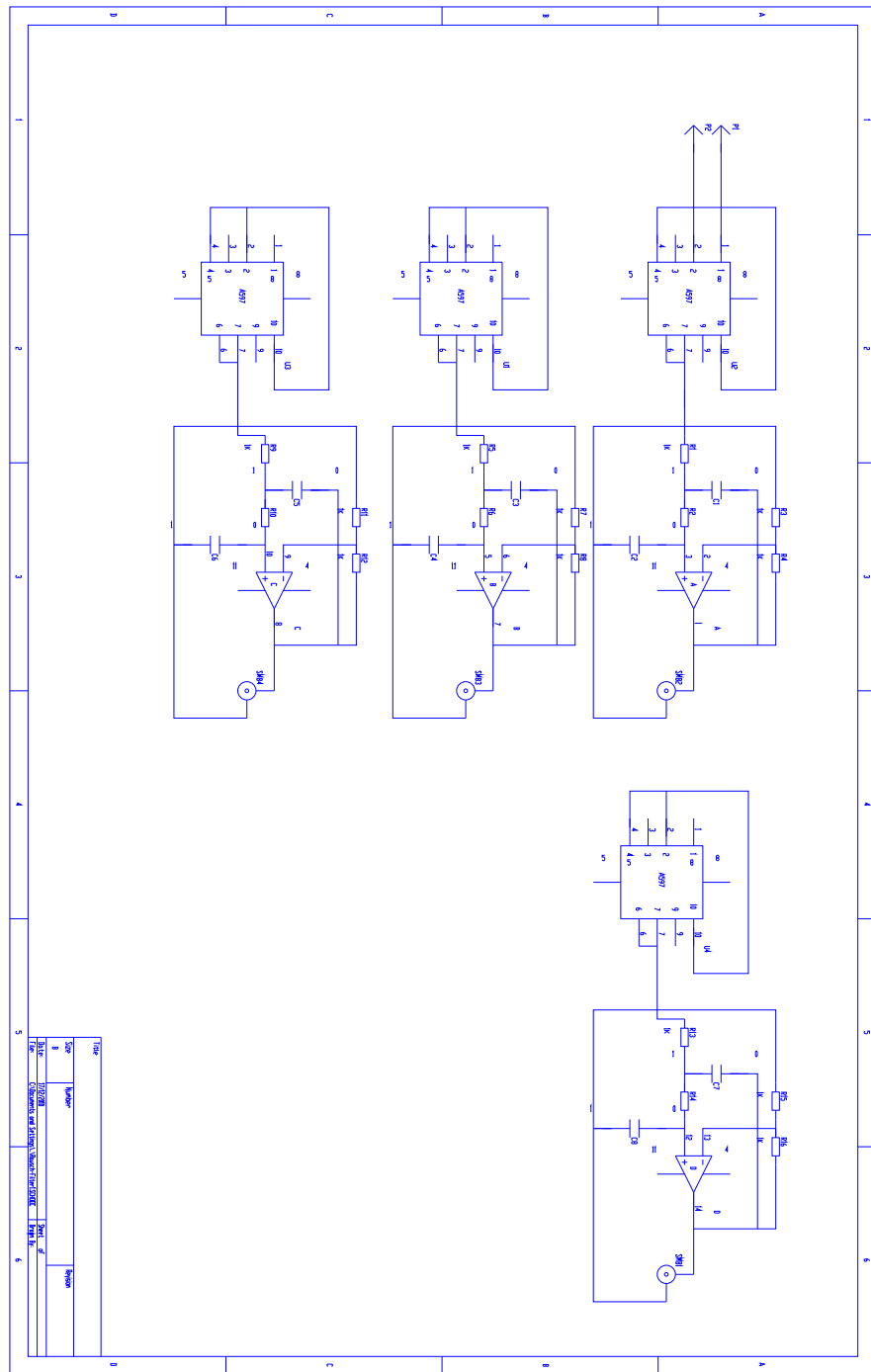
Appendix A

Appendix

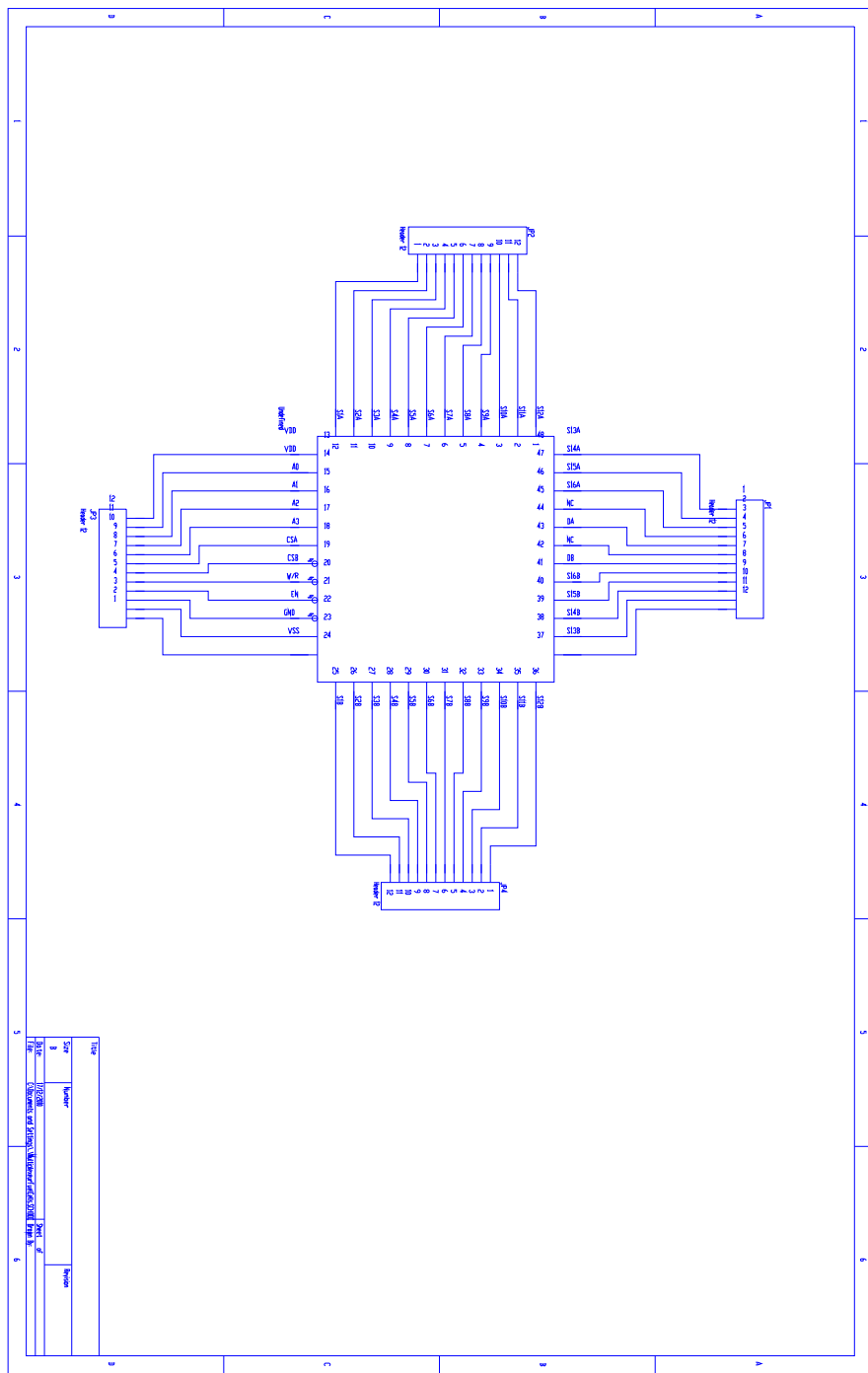
A.0.1 PCB circuit adapter, 4 – 20 mA to 0 – 10 V



A.0.2 Thermocouple signal conditioner PCB design



A.0.3 Multiplexer PCB design



Bibliography

- [1] J. T. Pukrushpan, A. G. Stefanopoulou, and H. Peng, “Control of fuel cell breathing,” *IEEE Control Systems Magazine*, vol. 24, pp. 30–46, April 2004.
- [2] J. T. Pukrushpan, H. Peng, and A. G. Stefanopoulou, “Control-oriented modeling and analysis for automotive fuel cell systems,” *Journal of Dynamic Systems, Measurement, and Control*, vol. 126, no. 1, pp. 14–25, 2004.
- [3] R. Talj, D. Hissel, R. Ortega, M. Becherif, and M. Hilairet, “Experimental validation of a pem fuel cell reduced order model and a moto-compressor higher order sliding mode control,” *IEEE Trans. Industrial Electronics*, vol. 57, no. 6, pp. 1906–1913, 2010.
- [4] V. Duindam and S. Stramigioli, “Port-based asymptotic curve tracking for mechanical systems,” *European Journal of Control*, vol. 10, no. 5, pp. 411–420, 2004.
- [5] Geplex-Consortium, *Modeling and Control of Complex Physical Systems: The Port Hamiltonian Approach*. Springer-Verlag, 2009.
- [6] A. Sánchez-Squella, R. Ortega, R. Griñó, and S. Malo, “Dynamic energy router,” *IEEE Control Systems Magazine*, vol. 30, pp. 72–80, Decembre 2010.
- [7] N. Mohan, T. M. Undeland, and W. P. Robbins, *Power Electronics, Converters, Applications and Design*. John Wiley & Sons, Inc., 1995.
- [8] R. Erickson and D. Maksimovic, *Fundamentals of Power Electronics*. Kluwer Academic Publishers, 2004.
- [9] K. Ogata, *Modern Control Engineering*. Prentice-Hall, 2003.
- [10] C.-T. Chen, *Linear System Theory and Design*. Oxford University Press, 1999.

- [11] H. K. Khalil, *Nonlinear Systems. 3rd edition.* Prentice-Hall, 2002.
- [12] R. Ortega, A. Loria, P. J. Nicklasson, and H. Sira-Ramirez, *Passivity-Based Control of Euler-Lagrange Systems.* Springer-Verlag, 1998.
- [13] A. Emadi, M. Ehsani, and J. M. Miller, *Vehicular Electric Power System.* Marcel Dekker, Inc., 2004.
- [14] M. Ehsani, Y. Gao, S. E. Gay, and A. Emadi, *Modern Electric, Hybrid Electric, and Fuel Cell Vehicles.* CRC Press., 2005.
- [15] P. Thounthong, S. Raël, H. Gualousand, D. Hissel, B. Davat, and A. Berthon, “Control strategies of embedded fuel cell–supercapacitor hybrid source,” in *Proceedings of the 2nd European Symposium on Supercapacitors & Applications (ESSCAP06)*, (Lausanne, Switzerland), pp. 1–6, November 2006.
- [16] T. Azib, O. Bethoux, G. Remy, and C. Marchand, “An innovative control strategy of a single converter for hybrid fuel cell/supercapacitor power source,” *IEEE Trans. Industrial Electronics*, vol. 57, pp. 4024–4031, December 2010.
- [17] P. Thounthong, S. Pierfederici, J. Martin, M. Hinaje, and B. Davat, “Modeling and control of fuel cell/supercapacitor hybrid source based on differential flatness control,” *IEEE Trans. Vehicular Technology*, vol. 59, pp. 2700–2710, July 2010.
- [18] F. Katiraei, R. Iravani, N. Hatziargyriou, and A. Dimeas, “Microgrids management,” *IEEE Power and Energy Magazine*, vol. 6, pp. 54–65, May/June 2008.
- [19] G. Pede, A. Iacobazzi, S. Passerini, A. Bobbio, and G. Botto, “Fc vehicle hybridisation: an affordable solution for an energy-efficient fc powered drive train,” *Journal of Power Sources*, vol. 125, no. 2, pp. 280 – 291, 2004.
- [20] J. Larminie and A. Dicks, *Fuel Cell Systems Explained.* John Wiley & Sons, Ltd., 2003.
- [21] S. Pasricha, M. Keppler, S. R. Shaw, and M. H. Nehrir, “Comparison and identification of static electrical terminal fuel cell models,” *IEEE Trans. Energy Conversion*, vol. 22, pp. 746–754, September 2007.

- [22] W. Friede, S. Raël, and B. Davat, “Mathematical model and characterization of the transient behavior of a pem fuel cell,” *IEEE Trans. Power Electronics*, vol. 19, pp. 1234–1241, September 2004.
- [23] S. Pasricha and S. R. Shaw, “A dynamic pem fuel cell model,” *IEEE Trans. Energy Conversion*, vol. 21, pp. 484–490, June 2006.
- [24] X. Kong, A. M. Khambadkone, and S. K. Thum, “A hybrid model with combined steady-state and dynamic characteristics of pemfc fuel cell stack,” in *Proceedings of 40th Industrial Application Conference (IAS 2005)*, pp. 1618–1625, October 2005.
- [25] K. Stanton and J.-S. Lai, “A thermally dependent fuel cell model for power electronics design,” in *Proceedings of 36th IEEE Power Electronics Specialists Conference (PESC 2005)*, (Recife, Brasil), pp. 1647–1651, June 2005.
- [26] K. P. Adzakpa, K. Agbossou, Y. Dubé, M. Dostie, M. Fournier, and A. Poulin, “Pem fuel cells modeling and analysis through current and voltage transient behaviors,” *IEEE Trans. Energy Conversion*, vol. 23, pp. 581–591, June 2008.
- [27] W. Turner, M. Parten, D. Vines, J. Jones, and T. Maxwell, “Modeling a pem fuel cell for use in a hybrid electric vehicle,” in *Proceedings of 49th IEEE Vehicular Technology Conference (VTC 1999)*, (Texas, USA), pp. 1385–1388, May 1999.
- [28] A. Miotti, A. D. Domenico, Y. G. Guezenne, and S. Rajagopalan, “Control-oriented model for an automotive pem fuel cell system with imbedded 1+1d membrane water transport,” in *Proceedings of 2005 IEEE Vehicle Power and Propulsion Conference (VPPC 2005)*, (Chicago, USA), pp. 611–618, September 2005.
- [29] J. Garnier, M. Pera, D. Hissel, F. Harel, D. Candusso, N. Glandut, J. Diard, A. D. Bernardinis, and J. K. G. Coquery, “Dynamic pem fuel cell modeling for automotive applications,” in *Proceedings of 58th IEEE Vehicular Technology Conference (VTC 2003)*, (Florida, USA), pp. 3284–3288, October 2003.
- [30] P. R. Pathapati, X. Xue, and J. Tang, “A new dynamic model for predicting transient phenomena in a pem fuel cell system,” *International Journal, Renewable Energy*, vol. 30, pp. 1–22, January 2005.

- [31] A. Vahidi, A. G. Stefanopoulou, and H. Peng, “Current management in a hybrid fuel cell power system: A model–predictive control approach,” *IEEE Trans. Control Systems Technology*, vol. 14, pp. 1047–1057, November 2006.
- [32] J. T. Pukrushpan, *Modeling and Control of Fuel Cell Systems and Fuel Processors*. PhD thesis, University of Michigan, 2003.
- [33] T. E. Springer, T. A. Zawodzinski, and S. Gottesfeld, “Polymer electrolyte fuel cell model,” *Journal of the Electrochemical Society*, vol. 138, no. 8, pp. 2334–2342, 1991.
- [34] C. Wang, M. H. Nehrir, and S. R. Shaw, “Dynamic models and model validation for pem fuel cells using electrical circuits,” *IEEE Trans. Energy Conversion*, vol. 20, pp. 442–451, June 2005.
- [35] M. Paul and K. Ilya, “Turbocharger modeling for automotive control applications,” in *SAE International*, (Detroit, Michigan), March 1999.
- [36] R. Talj, *Modélisation et Commandes Non Linéaires du système dair des Piles à Combustible Type PEM (Proton Exchange Membrane)*. PhD thesis, Université Paris-Sud 11, 2009.
- [37] M. Hinaje, I. Sadli, J.-P. Martin, P. Thounthong, S. Raël, and B. Davat, “Online humidification diagnosis of a pemfc using a static dc/dc converter,” *International Journal of Hydrogen Energy*, vol. 34, pp. 2718–2723, March 2009.
- [38] N. Fouquet, C. Doulet, C. Nouillant, G. Dauphin-Tanguy, and B. Ould-Bouamama, “Model based pem fuel cell state-of-health monitoring via ac impedance measurements,” *Journal of Power Sources*, vol. 159, pp. 905–913, September 2006.
- [39] H. Görgön, M. Arcak, and F. Barbir, “An algorithm for estimation of membrane water content in pem fuel cells,” *Journal of Power Sources*, vol. 157, pp. 389–394, June 2006.
- [40] M. Pérez, R. Ortega, and J. R. Espinoza, “Passivity-based pi control of switched power converters,” *IEEE Trans. Control Systems Technology*, vol. 12, no. 6, pp. 881–890, 2004.

- [41] M. Hernandez-Gomez, R. Ortega, F. Lamnabhi-Lagarrigue, and G. Escobar, “Adaptive pi stabilization of switched power converters,” *IEEE Trans. Control Systems Technology*, vol. 18, no. 3, pp. 688–698, 2010.
- [42] O. Bethoux, M. Hilairet, and T. Azib, “A new on-line state-of-health monitoring technique dedicated to pem fuel cell,” in *Proceedings of the 35rd Annual Conference of the IEEE Industrial Electronics Society (IECON09)*, (Porto, Portugal), pp. 2745 – 2750, November 2009.
- [43] S. Malo and R. Griñó, “Design and construction of an electric energy conditioning system for a pem type fuel cell,” in *Proceedings of the 33rd Annual Conference of the IEEE Industrial Electronics Society (IECON07)*, (Taipei, Taiwan), pp. 1633–1638, November 2007.
- [44] P. Thounthong, S. Raël, and B. Davat, “Utilizing fuel cell and supercapacitors for automotive hybrid electrical system,” in *Proceedings of the 20th Annual IEEE Applied Power Electronics Conference and Exposition (APEC05)*, (Austin, Texas, USA), pp. 90–96, March 2005.
- [45] W. Choi, J. W. Howze, and P. Enjeti, “Fuel-cell powered uninterruptible power supply systems: Design considerations,” *Journal of Power Sources*, vol. 157, pp. 311–317, June 2006.
- [46] M. E. Schenck, J. Lai, and K. Stanton, “Fuel cell and power conditioning system interactions,” in *Proceedings of the 20th Annual IEEE Applied Power Electronics Conference and Exposition (APEC05)*, (Austin, Texas, USA), pp. 114–120, March 2005.
- [47] G. Joós and J. Espinoza, “Three-phase series var compensation based on a voltage-controlled current source inverter with supplemental modulation index control,” *IEEE Trans. Power Electronics*, vol. 14, pp. 587–598, May 1999.
- [48] . L. Zubieta and R. Bonet, “Characterization of double-layer capacitors for power electronics applications,” *IEEE Trans. Industry Application*, vol. 36, pp. 199–205, January 2000.
- [49] M. Chami, M. Ayad, A. Djerdir, and A. Miraoui, “Control study of fuel cell and supercapacitors system using hybrid dynamic nets,” in *Proceedings of Industrial Electronics, 2008. IEEE International Symposium on (ISIE 2008)*, (Cambridge, UK), pp. 1622–1626, July 2008.

- [50] D. Casadei, G. Grandi, and C. Rossi, “A supercapacitor-based power conditioning system for a power quality improvement and uninterruptible power supply,” in *Proceedings of Industrial Electronics, 2002. IEEE International Symposium on (ISIE 2002)*, (L’Aquila, Italy), pp. 1247–1252, July 2002.
- [51] P. Thounthong, S. Raël, and B. Davat, “Control strategy of fuel cell/supercapacitors hybrid power sources for electric vehicle,” *Journal of Power Sources*, vol. 158, pp. 806–814, July 2006.
- [52] K. Jin, X. Ruan, M. Yang, and M. Xu, “Power management for hybrid fuel cell system,” in *Proceedings of 39th IEEE Power Electronics Specialists Conference (PESC08)*, (Rhodes, Greece), pp. 504–509, June 2008.
- [53] P. Thounthong, S. Raël, and B. Davat, “Control of fuel cell/supercapacitor hybrid sources for electric vehicle applications,” in *Proceedings of the 28th Electrical Engineering Conference (EECON-28)*, (Thailand), pp. 93–96, October 2005.
- [54] P. Thounthong, V. Chunkag, P. Sethakul, B. Davat, and M. Hinaje, “Comparative study of fuel-cell vehicle hybridization with battery or supercapacitor storage device,” *IEEE Trans. Vehicular Technology*, vol. 58, no. 8, pp. 3892–3904, 2009.